ABSTRACT

PROTECTION AND SENSITIZATION OF HUMAN CELLS TO PROTON RADIATION BY CERIUM OXIDE NANOPARTICLES

by Nathan B. Carlson

May 2017

Director of Dissertation: Jefferson Shinpaugh, PhD.

DEPARTMENT OF PHYSICS

In radiation therapy for the treatment of cancer, there is demand for novel approaches that will improve tumor cell killing while protecting healthy tissue. One such approach that has shown considerable promise is the application of nanoparticles as radiation sensitizers for tumor cells and as radiation protectants for healthy tissue. In this investigation, cerium oxide nanoparticles (CNPs) obtained from the University of Central Florida's NanoScience Technology Center were studied for their protective effect to charged particle radiation in non-malignant breast cells, and for their sensitizing effect in breast and prostate cancer cell lines. These experiments were conducted at East Carolina University, where human cells were grown in the cell culture facility in the Department of Biology and then irradiated with energetic protons in the Accelerator Laboratory in the Department of Physics. Prior to irradiation, the cells were treated with distinct CNP preparations ranging in concentrations from 10 nanomolar to 10 micromolar, and cell viability was assessed using multiple assays post-irradiation. Radioprotection and radiosensitization were observed for several of the CNP treatments tested. Ultimately, the goal is to find a specific nanoparticle treatment that holds the synergistic effect of enhancing the rate of killing in tumor cells while simultaneously improving the survival of normal cells.

PROTECTION AND SENSITIZATION OF HUMAN CELLS TO PROTON RADIATION BY CERIUM OXIDE NANOPARTICLES

A Dissertation

Presented To the Faculty of the Department of Physics

East Carolina University

In Partial Fulfillment of the Requirements for the Degree

Doctor of Philosophy in Biomedical Physics

by

Nathan B. Carlson

May 2017

PROTECTION AND SENSITIZATION OF HUMAN CELLS TO PROTON RADIATION BY CERIUM OXIDE NANOPARTICLES

by

Nathan B. Carlson

APPROVED BY:

DISSERTATION ADVISOR_____
Jefferson Shinpaugh, Ph.D.

COMMITTEE MEMBER_____
Michael Dingfelder, Ph.D.

COMMITTEE MEMBER_____
Ziwei Lin, Ph.D.

COMMITTEE MEMBER_____
Cindy Putnam-Evans, Ph.D.

COMMITTEE MEMBER_____
Jean-Luc Scemama, Ph.D.

CHAIR OF THE DEPARTMENT OF PHYSICS_____
Jefferson Shinpaugh, Ph.D.

DEAN OF THE GRADUATE SCHOOL_____
Paul J. Gemperline, Ph.D.

DEDICATION

This work is dedicated to my loving wife and our expected son.

ACKNOWLEDGEMENTS

I want to thank my advisor Dr. Jeff Shinpaugh for allowing me to perform research in his lab and for the giving of his time and expertise. Under his guidance I was provided with steadfast support and extensive resources, which created the perfect environment to obtain knowledge and experience as a research scientist. I thank Chris Bonnerup and the rest of the ECU Accelerator team: William, Mike, and Gene for being patient with me, answering my questions, and helping me understand how the world works inside and outside the lab. I thank Jianfen Lu for investing her time into a physicist and patiently teaching me the correct ways of cell culture. I would also like to thank my committee members: Dr. Michael Dingfelder, Dr. Ziwei Lin, Dr. Cindy Putnam-Evans, and Dr. Jean-Luc Scemama for the giving of their time and using their expertise to assist me in accomplishing this endeavor. I want to acknowledge my colleague and friend Chris Boyd, without whom this research would not be possible. There were countless hours spent in the lab trying to produce data and ongoing phone call conversations trying to understand our findings. This joint experience during our time here at ECU developed a lifelong friendship.

TABLE OF CONTENTS

LIST OF FIGURES

LIST OF ABBREVIATIONS

Chapter 1: Introduction

Ionizing radiation is a valuable resource for humanity when properly controlled and is widely used in the fields of medicine, agriculture, energy, and research. It is, however, harmful to people and certainly lethal at sufficiently high doses. It has a damaging effect on human tissue that can disrupt the normal operations and functions of cells within the body. The potential risks to our bodies have inspired research focused solely on radiation exposure from accidents like industrial incidents, acts of terrorism, and even space travel [1, 2]. Studies have shown that radiation due to medical sources alone is responsible for an almost 600% increase in exposure over the past three decades, primarily from CT scanning and nuclear medicine [3]. It is estimated that medical radiation exposure is now approximately equal to natural background radiation [3]. The biological effect of ionizing radiation on human tissue is primarily a consequence of the ionization of the atoms that make up the molecules of the tissue. An abundance of radiation exposure can produce immediate effects such as radiation sickness as well as long-term effects such as cancer [4]. Within the scope of radiation therapy, ionizing radiation can be beneficial and is used for the treatment of certain cancers. Efforts are being made that incorporate specialized additives as a way to enhance the effectiveness of this therapy [5, 6]. In other fields, where ionizing radiation is unavoidable and destructive, the main focus is to lessen its damaging effects. In the area of extended space travel, there is concern that astronauts who suffer from short-term effects due to overexposure would not have accessible or sufficient medical care. Therefore, efforts are being made to discover techniques to prevent or mitigate the damaging effects of radiation [7].

Radiation describes the emission and propagation of energy through space or a material medium [4]. As radiation traverses a material, it will encounter the orbital electrons and atomic nuclei of the atoms inside and interact via elastic collisions, inelastic collisions, or absorption events. Energy is deposited along the path that it travels in the material, known as the track [4]. The amount of deposited energy and its distribution depends on the radiation type and the probability (cross-section) of particle interactions within the material. The atoms within a material can absorb this lost energy through excitation or ionization, decreasing the intensity of the radiation as it traverses the material. This process generates secondary electrons that contain enough energy to contribute to damage within a material. These unbound electrons can now transport the energy nearby or deposit the energy far away from its original position, thus propagating the process. The dose is the amount of this energy absorbed in the material, given as energy per unit mass in Gray (Gy) [4]. There are different kinds of radiation that can deposit such energy including high-energy photons (x-rays and gamma rays), electrons, neutrons, protons, alpha particles and heavier ions. Each class of radiation has multiple processes for interacting and depositing energy in matter. Protons, neutrons, electrons, alpha particles and heavier ions are characterized as particulate radiation. Photons fall into the category of electromagnetic radiation and will primarily interact with matter by means of the photoelectric effect, the compton effect, or pair production.

1.1 Electromagnetic Radiation

In the photoelectric effect, an incident photon is completely absorbed by an atom. This causes a core electron to be ejected from the atom leaving behind a vacancy. The atom

is left in an excited state, which results in a de-excitation process that allows an outer electron to fall to the inner orbit and fill the vacancy. Characteristic X-rays and/or Auger electrons are produced as a result of this transition process. This generally occurs at energies up to 0.5 Mev [8].

With the Compton effect, an incident photon interacts with an outer shell electron. The photon strikes a loosely bound orbital electron and transfers a portion of its energy. The electron ejects, and the photon scatters. This results in a Compton electron and a lower-energy scattered photon. The Compton effect tends to dominate between 0.5 Mev and 5 Mev [8].

For pair production to occur, a high-energy incident photon with sufficient minimum energy of 1.022 MeV interacts with an atom's nucleus. As a result of this interaction the photon annihilates and an electron-positron pair is created. This specific minimum energy required of the incoming photon is representative of the total rest mass of the electron-positron pair. If there is excess energy above this requirement, it is transferred to kinetic energy that is shared by the pair. The positron will eventually interact with another electron and annihilate. This annihilation produces two 511 KeV photons traveling in opposite directions and fulfills the physical laws of conservation of momentum and energy. Pair production will start to dominate at energies above 5 MeV [8].

In all of these cases the subsequent secondary electrons and photons will continue to interact in a cascading manner, depositing their energy throughout a targeted material. Neutrons, electrons, protons, and heavy ions are considered particulate radiation, and they have distinct processes for interacting with matter.

1.2 Particulate Radiation

Since neutrons do not experience a Coulomb force, they interact with matter through direct head-on collisions. These collisions are primarily with atomic nuclei in the target material. Collisions with orbital electrons are negligible. Neutrons can interact with matter through neutron moderation (elastic collisions), neutron resonance scattering (inelastic collisions), or through nuclear reaction (an absorption process) [9]. Since they provide a neutral charge and a small cross sectional area in general (except with resonance scattering), neutrons have no definite range of penetration. The most elastic collisions with atomic nuclei will occur with those that are light in mass, such as hydrogen nuclei which is essentially a proton. Having close to the same mass, this interaction would result in a significant loss in the kinetic energy of the neutron. However, with heavier atomic nuclei, only a small fraction of the neutron's energy would be lost in a collision and thus providing the neutron with a longer range in the target medium [9, 10].

The primary interaction for incoming electrons will be with other orbital electrons. The Coulomb force dictates how electrons will interact in matter. For high electron energies (like in medical applications), elastic and nuclear interactions will occur. Rutherford scattering occurs when electrons undergo elastic interactions. Inelastic collisions, such as electron-nucleus Coulomb interactions, can result in bremsstrahlung radiation, which occurs when an electron emits a photon as it experiences a change in acceleration. This difference in the acceleration of the electron causes a change in kinetic energy and manufactures a photon with that same energy [11]. The bremsstrahlung photons may then go on to have secondary interactions in the target medium. Because this

type interaction contains equivalent masses, large losses in energy are common. Scattering angles can be sufficiently wide as well, causing the ultimate path inside the target material to become convoluted. For lower electron energies, ionizations and excitations will dominate. As the electron ionizes along the path and moves to the end of its range in the material, it will slow down and deposit more energy. This is due to the strong velocity dependence of the ionization cross section [12]. Low energy secondary electrons will eject from the ionizations along the track and higher-energy secondary electrons (so called delta rays) can eject much further from the original track [10].

Heavier charged particles behave in a similar fashion as electrons in the way that they are dictated by the Coulomb force. Nuclear elastic scattering may occur, as well as the expected ionizations and excitations. For higher energies, nuclear collisions will typically result in target fragmentation. They can undergo elastic Rutherford scattering as well as inelastic interactions resulting in bremsstrahlung radiation, however these effects are usually neglected since the scattering angles are so small. A heavier charged particle will lose energy in matter primarily through ionization and excitation of orbital electrons. This is known as collisional energy loss. Secondary electrons can result from the collisions, and these ejected delta rays can contain adequate kinetic energy to promote further ionization in the target matter. Unlike electrons and uncharged particles, heavier charged particles tend to have a straighter path in the target medium due to their heavier mass. As the heavier charged particles travel through the medium losing energy, they slow down and the energy loss spikes right before dropping off at the end of their range. This increase in energy deposition at the end of the path is called the Bragg peak [9]. The energy deposition is typically shown as a plot of stopping power vs. range in the target material, with the

Bragg peak being the region at which the rate of energy loss is a maximum. As the energy of the incoming particle increases, the Bragg peak is pushed further into the medium.

1.3 Types of Radiation Damage

When it comes to biological material and ionizing radiation, the ultimate concern is DNA damage. With direct damage, charged particles or photons alter DNA directly causing strand breaks, base damages, etc. Indirect damage occurs when molecules in the surrounding medium (water) are ionized to form free radicals, which can subsequently damage nearby DNA and cause strand breaks. The exposure of cells to radiation gives rise to these free radicals, formed from ionizing reactions, which in turn react with the DNA [13]. When it comes to damage and the repair process, a single strand break is easier for the cell to repair than a double strand break [14]. A double strand break forms when two single strand breaks occur in near vicinity to each other. This probability increases with higher linear energy transfer (LET) radiation, since there are more events per track length available. Whether direct or indirect, these kinds of damages can lead to multiple endpoints including mutations, chromosome aberrations, genomic instability, or ultimately apoptosis [15].

Radioprotectors are of growing interest as a way to mitigate damage to the cell by removing these free radicals. By providing valence electrons, radioprotectors can bind with the radicals and neutralize them. This process is essentially intercepting free radicals before they have a chance to cause indirect damage to DNA [16]. It would be exceptionally beneficial to discover an alternative that serves as both an effective radioprotector for normal tissue and an effective radiosensitizer for tumor tissue in radiation therapy. Recent

studies show that cerium oxide nanoparticles (CeO_2) are being tested as appropriate free radical scavengers and show potential for increasing cell survival [17, 18]. Although some research has been piloted using photon radiation (x-rays), the influence that cerium oxide nanoparticles have when paired with charged particle radiation remains under investigation.

1.4 Radiological Physics

One essential building block of radiation physics, and by extension dosimetry, is the measure of stopping power. Stopping power describes the average linear rate of energy loss in a medium by a charged particle [10]. It is typically represented as -dE/dx where E symbolizes energy and x signifies distance, giving units typically of MeV/cm. If the probability per unit distance of travel that an electronic collision occurs is denoted as μ and the average energy loss per collision is expressed as Q_{avg}, then the stopping power can be found as the product of these two quantities. It is calculated as

$$S(E) = -\frac{dE}{dx} = \mu Q_{avg} = \mu \int_{Q_{min}}^{Q_{max}} QW(Q)dQ \tag{1.1}$$

with μ (the attenuation coefficient) given in units of cm^{-1} and Q_{avg} measured in eV. Q_{avg} is equivalent to the integration of the single collision energy-loss spectra, where Q is the energy loss for each collision and W(Q)dQ is the probability that a given collision will result in an energy loss between the range of Q and Q+dQ.

It can be useful to divide the stopping power by the density of the target material, ρ (g/cm^3). This is known as mass stopping power and is represented as –dE/ρdx with units

typically of MeV cm^2/g, and this conveys the rate of energy loss of the charged particle per g cm^{-2} of the material penetrated. This way of expression is extremely beneficial since the mass stopping power is somewhat uniform among materials sharing similar atomic compositions [10]. The stopping power would depend on the pressure for a gas target. Using the mass stopping power instead rectifies this issue of pressure dependence since it is already taken into account by the density of the target.

Although the stopping power represents the amount of energy lost by a particle as it travels through a material, it does not necessarily equal the amount of energy absorbed by a target. This is especially true for small targets like cells. The range of the secondary electrons produced by the incident radiation has to be considered. The higher the incident radiation energy, the higher the possible maximum energy transfer will be to a secondary particle. With enough energy, delta rays can certainly escape a small volume where the initial charged particle lost its energy. Therefore the restricted stopping power is a better representation of the amount of lost energy that is actually absorbed in the target [10]. Restricted stopping power, $-(dE/dx)_{\Delta}$, is characterized as the rate of energy loss due only to the collisions in which the energy transfer does not exceed a determined threshold Δ. It is used as a way to measure the localized energy transfer along the track and excludes all secondary electrons with kinetic energies above larger than Δ. Linear energy transfer (LET) was introduced in the early 1950's and is defined as the rate of energy transferred per unit distance along the path of the charged particle with units of keV/μm [8]. LET and stopping power are two distinctive ways of characterizing similar settings. Stopping power is portrayed in terms of energy lost, while LET is explained in terms of energy transferred. Either way it is approached, both terms can be classified as restricted or unrestricted.

If two identically charged particles were to penetrate the same type material, they would not necessarily behave the same way. This stochastic nature causes statistical fluctuations in the number of collisions along a path and the amount of energy lost due to each collision. Any number of identical particles starting out under identical conditions will result in a distribution of energies as they pass a given depth and a distribution of pathlengths traversed before they stop. This phenomenon of identical initial conditions yielding unequal losses in energy is called energy straggling, and the existence of varying pathlengths is referred to as range straggling [8].

An increase in the energy of the incoming charged particle would increase its velocity and ultimately cause an increase in the range of the charged particle, so long as the ionization cross section did not increase. An increase in energy would also cause the stopping power to decrease, since the number of possible interactions decreases and it becomes less likely to slow down the particle with collisions. For the probability of interactions to increase, the energy of the charged particle must decrease, the density of the target material must increase, or the volume of the target must be made large enough to improve the chance of collisions between the charged particle and orbital electrons. On a plot of relative count rate vs. absorber thickness, the mean range can be found as the amount of absorber thickness required to obtain a relative count rate of 0.5, and an extrapolated range can be found by extending the straight portion of the curve down to the x-axis [10]. Monte Carlo simulations that are built into the Stopping and Range of Ions in Matter (SRIM) code show that the range straggling difference for 3 MeV protons in water is approximately eight percent [19].

1.5 Calculating Dose

For radiotherapy and radiobiological experiments, it is essential to measure the dose in the beam of charged particles. This is often accomplished by placing ionization chambers at different depths within the target material while exposed to the beam. The dose rate is proportional to the current of the beam. For a monoenergetic beam, a depth-dose curve shows the dose rate as having a maximum in the Bragg peak region near the end of the particle's range. The LET would also reach a maximum at that same depth in the target material. For a beam of low-energy protons (≤400 MeV), the energy lost in a target material is almost entirely due to collisions with orbital electrons. For a beam of high-energy protons, there begin to be more nuclear interactions and the depth-dose curves can become quite different from the mass stopping power curves [10].

To effectively calculate a dose rate, a uniform parallel beam comprised of monoenergetic charged particles is considered. If this beam is normally incident on a thick tissue slab, then a fluence rate $\dot{\varphi}$ can be measured in $cm^{-2}\ s^{-1}$. To calculate the dose rate at a given depth x in the slab, a thin disc-shaped volume with thickness Δx is considered along the central axis having an area A normal to the beam. Using the collisional stopping power (-dE/dx), the rate of energy deposition in the volume can then be calculated as

$$\dot{E} = \dot{\varphi} A \left(-\frac{dE}{dx}\right) \Delta x \tag{1.2}$$

where $\dot{E}$ is measured in MeV s^{-1} [10]. Now the dose rate can be understood by dividing the rate of energy deposition by the mass of the volume element (ρAΔx) to get

$$\dot{D} = \frac{\dot{\varphi} A \left(-\frac{dE}{dx}\right) \Delta x}{\rho A \Delta x} = \dot{\varphi}\left(-\frac{dE}{\rho dx}\right) \tag{1.3}$$

where ρ is the density of the tissue. The dose rate $\dot{D}$ is measured in units of MeV g^{-1} s^{-1} [10]. It can be recognized that the dose per unit fluence at any given depth is equivalent to the mass stopping power for particles at that given depth. For instance, if the mass stopping power is 5 MeV cm^2 g^{-1}, then the dose per unit fluence can be written as 5 MeV g^{-1} assuming the fluence unit is in cm^{-2}. For high-energy charged particles, this analysis becomes insufficient as the nuclear interactions become more significant and the depth-dose curves cannot be accurately calculated. At that point Monte Carlo calculations are considered that estimate the outcome of individual incident and secondary particles statistically using the cross sections of various nuclear interactions that transpire. Since the energies used in this research were low (<4 MeV), Monte Carlo simulations were not required and this analysis was adequate in determining the dose rate.

1.6 Water-Derived Radicals

Ionizing radiation can produce an abundance of secondary electrons in matter, and even more so in liquid water. This is especially relevant in understanding the biological effect to mammalian cells, which are comprised of approximately 70-85% water. These secondary electrons deposit their kinetic energy throughout the water volume [9]. In the first 10^{-15} seconds of radiation, the initial changes in water result in the creation of ionized molecules (H_2O^+), excited molecules (H_2O^*), and free electrons (e^-) in local regions around the track [10]. These three species generate changes in the water volume that produce free

radicals. There are numerous reactions and various products that arise from the radiolysis of water within a cell, as seen in the literature [20-23]. One possibility is for an ionized water molecule to react with a neighboring molecule to form a hydronium ion and a hydroxyl radical.

$$H_2O^+ + H_2O \rightarrow H_3O^+ + {}^{\bullet}OH \tag{1.4}$$

Another possibility is for an excited water molecule to give up its energy either by losing an electron (thus becoming an ion) or by molecular dissociation.

$$H_2O^* \rightarrow \begin{cases} H_2O^+ + e^- \\ H + OH \end{cases} \tag{1.5}$$

The free electrons can become thermalized by losing their energy to water molecules through vibrational and rotational excitation [10]. These thermalized electrons orient the permanent dipole moments of neighboring water molecules forming a cluster or aqueous electron.

$$e^- \rightarrow e_{aq}^- \tag{1.6}$$

Of the new reactants that were formed, ${}^{\bullet}$OH, e_{aq}^-, and H are chemically reactive. These radical species born from water with their unpaired electrons are known as free radicals and they are more than capable of causing biological damage. With cells comprised of 80% water, free radicals are known to wreak havoc to DNA in mammalian targets. This process can also include oxidation and spawn oxygen-derived radicals known as reactive oxygen species (ROS), which are highly reactive to DNA [24]. In the case of low LET

radiation (such as <2 keV/μm x-rays or gamma rays), free radicals are responsible for as much as two thirds of the DNA damage incurred [24].

1.7 DNA Damage and Repair

When it comes to radiation on biological targets, there are two pathways for damage: direct and indirect [4]. Direct damage is when the radiation itself directly interacts with the cell components. Indirect damage is when free radicals that were formed from the incident radiation interacting inside the biological material start to chemically react with the DNA. In proton radiation, for example, ions can physically break base pairs in the DNA strands by means of direct damage. That same radiation could also produce an OH radical that may attack a DNA sugar and cause a strand break through means of indirect damage. Regardless of the pathway, the damage to DNA from direct and indirect effects is the same. There can be basic damage such as base damages, single strand breaks (SSB), and double strand breaks (DSB), as well as complex damage that includes any combination of those. These damages can contribute to changes in the DNA structure by point mutations, chromosome aberrations, and crosslinks between strands. Since the double-stranded nature of DNA allows the two strands to complement each other, if one strand is broken then the opposite strand can be used as a template for repair. For this reason, most single-strand breaks can be repaired naturally. However, with double-strand breaks, repair can be far more problematic. The broken ends of DNA may be incorrectly rejoined. If these occurrences are not properly repaired, it can lead to cell damage and ultimately apoptosis (programmed cell death) or necrosis (death due to injury) [24]. In the case of high LET radiation (> 4 keV/μm protons, neutrons, and heavy ions), contributions from direct effects

become dominate, and repair could become exceedingly difficult as the probability of the complexity of damage increases [24]. Double strand breaks can arise from an individual radiation track alone or from multiple single strand breaks within close proximity, for example 6-10 base pairs [25]. Cells that survive irradiation and have sustained a double-strand break could have a segment of DNA that has been deleted. If two distinct double-strand breaks occur, there can be misrepair of the two outer ends of each break and loss of the section between the breaks. There is also the possibility of enzyme digestion of nucleotides. This process of cleaning the broken ends of one double-strand break before rejoining can leave a segment deleted [24].

Ultimately, there are four generalized outcomes for radiation damage on a cell that can occur. The cell can go undamaged from the radiation and function as usual. The cell could incur damage, but the damage is repaired properly and the transformed cell operates normally. The cell could receive some damage and the damage is misrepaired causing the cell to operate abnormally. The cell can obtain sufficient damage and die as a result. There are many different types of cells however, and they are not all as equally sensitive to radiation damage. The human body is a sophisticated interconnected system with various complex organs and certain specialized cells are associated with each organ. Cells that are not as specialized and divide rapidly tend to be more sensitive to lower doses of radiation than those that divide less rapidly and are more specialized [4].

1.8 Biological Effects

The biological effect of radiation has a great dependency on the dose received, the kind of radiation, and the observed endpoint. Sometimes the biological effect is immediate

and other times it may take years for it to become evident. Two categories are used to divide up these effects, stochastic and deterministic (or nonstochastic) [10]. A stochastic event is one that will occur in a statistical manner. There is no guarantee that a certain effect will appear, like with cancer. For instance, if a large population of people were to be exposed to radiation, it is possible that they may not all develop cancer in their lifetime. Furthermore, cancer can manifest naturally on its own without exposure, so it cannot be evident that any radiation exposure is the source an incidence of cancer. What is recognized is that the chances of cancer increase as the dose of radiation exposure increases. Additionally, there is no threshold dose under which there exists a zero probability of developing cancer. Biological effects of ionizing radiation that are stochastic include a shortened lifespan, genetic effects, and mutated offspring. On the other hand deterministic effects have a more clear and causal outcome with a dose of radiation exposure as well as a threshold dose [10]. Biological effects of ionizing radiation that are deterministic include cataracts, skin erythema, infertility, and acute radiation syndrome (ACR) [10]. If a person is exposed to a large enough short-term whole body dose of radiation, they can develop ACR. This results in the rapid depletion of radiosensitive cells in the blood and digestive tract, which can cause infection, bone marrow damage, organ and tissue damage, and even death at high enough doses.

1.9 Radioprotectors, Radiomitigators, Radiosensitizers

There are certain safety procedures that will reduce or even prevent such biological events from manifesting. These procedures include some form of shielding, increasing the distance between the source and the subject, and decreasing the time of exposure.

However, circumstances do arise in which a subject cannot implement these safety procedures. In those situations, it may be necessary to use radioprotectors to reduce or mitigate the damaging effects of ionizing radiation. The ideal radioprotector would contain certain uncompromised qualities. It would obviously have to significantly protect against radiation effects as well as provide this protective effect to the majority of internal organs. At the same time it must have an efficient time-window effect, an acceptable toxicity and stability profile, an acceptable method of administration, and be compatible with the expansive scope of other drugs available to patients and workers [2]. There are currently no radioprotectors that meet all of these requirements, but there are those that provide some protection from radiation by ways of diminishing the indirect damage [26]. A parameter used to describe the effectiveness of a radioprotector is the dose reduction factor (DRF). DRF is determined by dividing the dose of radiation in the presence of a drug at a set lethality by the dose of radiation in the absence of the drug at that same lethality. The typical lethality used is a lethal dose to 50 percent of the population after 30 days (LD 50/30) [24].

Currently, amifostine is the most well known radioprotector. It's active molecule WR-1065 provides radioprotection to cells and has been shown to prevent cell death in the presence of both direct and indirect ionizing radiation, while also mitigating genomic instability effects in the surviving cells [27, 28]. Amifostine also allows for the binding of free radicals and can induce hypoxia, which prevents reactive oxide radicals from forming, contributing to DNA protection and repair [29, 30]. Because of its success, amifostine is used in industry, medical and government applications. Astronauts have used it on missions to the moon as a safety precaution in case of a solar event. Approved by the Food

and Drug Administration as a radioprotector, it is the prevailing cytoprotective compound used today [24, 27]. However, amifostine is not the ideal radioprotector. Its side effects include severe nausea, vomiting, allergic reactions, and acute hypertension [31]. It leaves the central nervous system completely unprotected, so it is unable to provide protection to all the human organ systems [27]. It must be administered before exposure, which is not a beneficial time-window effect in the case of a nuclear incident or terrorist attack. Amifostine is valuable in specific scenarios, nevertheless it is still necessary find other possible radioprotective candidates that can more adequately fulfill the requirements of an ideal radioprotector.

Other candidates include radiomitigators, nitroxides, and bisbenzimidazol compounds. Palifermin is a considered a mitagant prototype and is delivered after exposure to radiation to target the initiated cell repair responses that include DNA repair, apoptosis activation, cell proliferation, and cell immunoinflammmatory reactions [30]. Nitroxides like tempol act as stable free radical compounds that interact with other free radicals that develop from ionizing radiation. Tempol has shown protective properties against radiation *in vitro* for mammalian cells in aerobic conditions as well as *in vivo* after whole body irradiation [32, 33]. Bisbenzimidazol compounds also show promise as radioprotectors. Hoechst 3342 was used *in vivo* and showed protection in the mouse lung model when administered half an hour before exposure. Higher concentrations of Hoechst 3342 show cytotoxicity and mutagenic effects, therefore derivatives of Hoechst are being explored that will produce less of a negative effect [34, 35].

Cytokines have shown potential as a viable natural radioprotector [36]. Herbal medicines and antioxidants have also shown promise in providing radioprotection. Naturally occurring vitamin E is a free radical scavenger that has low toxicity even at high doses and shows improvement of survival rates in mice exposed to radiation [37, 38]. Melatonin is a naturally occurring hormone produced in the pineal gland that is used as an over-the-counter (OTC) sleep aid. Some findings suggest that it is capable of scavenging free radicals [39]. Ginseng is a well-known OTC herbal medicine recognized for its benefits with diabetes, improving aging, reducing stress and fatigue, and also promoting DNA, RNA, and protein synthesis [40-42]. Ginseng extract was used with human lymphocytes exposed to radiation and showed a reduction in micronuclei, which is an indicator of cellular DNA damage [43].

Soy products are also promising in the field of natural radioprotectors. Genistein is a naturally occurring compound in soybeans that has shown benefits in cardiovascular disease, high cholesterol and osteoporosis [44]. The protective properties of genistein were shown in a study where it was intravenously injected into mice 24 hours prior to gamma radiation exposure and an increase in survival rate was observed [45]. Genistein has also shown properties of radiosensitization with regards to tumor cells, specifically human cervical cancer cells [46]. The ability of genistein to inhibit growth in different cell lines and reduce viability has an enhanced effect when combined with radiation [47]. This growth inhibition effect of genistein is seen at concentrations greater than 10 μM, while below this concentration genistein stimulates growth. An analysis of the different doses of genistein (10 nM to 100 μM) on human breast cancer carcinoma cells revealed that the lower doses

(< 10 μM) show growth promotion and growth inhibition wasn't displayed until higher doses [48].

Nanotechnology has become increasingly popular within the broad scope of biomedical research. This technology has applications in drug delivery systems, tissue engineering, luminescent biomarkers, MRI shielding, cancer therapy, as well as many others [49]. There have been developments for using nanoparticles in radiotherapy [5, 6]. Several different forms and variations of nanoparticles are being explored. Extensive research has been done using gold [50-55], silver and zinc nanoparticles [56-59], for protection from or sensitization to radiation. There are promising results that have been shown for a wide range of metal-based nanoparticles in the field of radiation therapy, including platinum, iron, and gadolinium [60-63]. The use of nanoparticles in radiotherapy is an active area of research.

1.10 Cerium Oxide Nanoparticles

Cerium oxide nanoparticles (CNPs) have been shown to provide radioprotection to normal tissue and radiosensitization to malignant cells using x-rays [17, 64-67]. They are comprised of a cerium core surrounded by an oxygen lattice. CNPs are synthesized using a micro-emulsion process consisting of surfactant sodium bis(2-ethylhexyl) sulfosuccinate (AOT), toluene, and water [18]. CNPs have gained a lot of interest due to their regenerative antioxidant properties exhibited in the reaction cycle of Ce^{3+} to Ce^{4+} to Ce^{3+}. This continuation on the surface of the CNPs offers an antioxidant with unique protection properties [65, 68]. Cerium oxide can be designed to retain a specific Ce^{3+}/ Ce^{4+} ratio. When this ratio is controlled, it can determine the CNPs distinction as an effective catalase

mimetic, superoxide dismutase (SOD) mimetic, or both, cleaving O_2 radicals and hydrogen peroxide and rendering them inactive [66, 69, 70]. Among their antioxidant behaviors, CNPs have been shown to be efficient scavengers for nitric oxide [71] and hydroxyl radicals [72]. CNPs have also shown oxidant properties under specific environmental conditions [73]. These properties increase the specialty of CNPs and the benefits of their effects on both nonmalignant and malignant cells. In cancer cells, CNPs have been shown to possess an inherent cytotoxicity and have also been shown to sensitize tumor cells to radiation-induced apoptosis while protecting the surrounding healthy tissue [17, 18, 74-76]. This inherent cytotoxicity to tumor cells is not fully understood, but it is thought to be due to the CNPs ability to provide free radicals that increase oxidative stress to the cancer cells. In addition to the cytotoxicity trait, they have been shown to limit the invasive characteristics of tumor cells. CNPs have been shown to decrease the ability of myofibroblasts to stimulate invasion by squamous tumor cells and also inhibit the ability of squamous tumor cells to invade without the presence of myofibroblasts stimulation [77, 78].

As an ideal candidate for radiation therapy, CNPs offer the synergistic feature of operating as an oxidant for cancerous cells as well as an antioxidant for normal cells. Natural antioxidants have the potential to be dangerous to cancer patients that are currently receiving treatment [79]. This provides a greater demand for an appropriate alternative. Recent studies indicate that treatment of CNPs preceding radiation therapy leads to decreased cell damage and death for normal tissue in the gastrointestinal (GI) tract, lung, head, and neck [18, 67, 74]. Also, CNPs have the ability to enhance the killing of tumor cells when they are used in low pH conditions prior to radiation therapy. Studies have shown, in pancreatic cancer cells, that CNPs have the ability to increase the level of

radiation-induced oxidative species [64]. Therefore, CNPs behave as a radiosensitizer in cancer cells by encouraging the production of reactive oxygen species (ROS) and maintaining their levels within tumor cells. This behavior combined with their inherent toxic effects make CNPs a formidable option to consider when combating tumor cell viability and growth.

CNPs have useful applications in more areas than just cancer treatment. They show promise in treating other diseases as well, specifically those characterized by ROS accumulation. Neurodegenerative diseases such as Parkinson's, Huntington's Alzheimer's, and age related macular degeneration have been connected to increased ROS levels which can prevent cellular mechanisms from combating oxidative stress [80]. A preliminary study showed that, in mouse models of hereditary retinal degeneration, CNPs scavenged ROS and reduced apoptosis in photoreceptor cells preventing retinal deterioration [81]. The regression of pre-existing pathologic retinal neovasculature has also been demonstrated using CNPs, which suggests an antiangiogenic property [80]. Increased ROS levels have been recognized as an important influence in the progression of diabetes. These levels are especially high in the liver where free radicals are removed from the bloodstream [82]. Studies have shown that, once treated with CNPs, hepatic ROS levels in diabetic rats returned to levels that were similar to non-diabetic rats while triglycerides decreased and HDL levels increased in the blood [82]. In pancreatic islet cells, CNPs have been shown to increase the viability of the pancreatic islet function thereby increasing insulin secretion and decreasing ROS levels [83]. These results help to further support CNPs as a possible treatment for diabetes.

Studies that were performed with CNPs in animal models demonstrate an apparent lack of toxicity, however research with cells *in vitro* presents conflicting evidence. This conflict is believed to arise from the undetermined cellular and environmental factors that influence their oxidant and antioxidant behavior [84]. Studies have shown that in culture CNPs are toxic to bronchial epithelial lung fibroblasts [85], yet non-toxic to mammary epithelial cells [17], pancreatic cells [64], macrophages [86], and keratinocytes [87]. In normal cells, the pH level of the cellular environment enables the CNPs to perform radical scavenging. Research on numerous human cancer cells *in vitro* show that CNPs are toxic, including alveolar epithelial cancer cells [76], squamous cell carcinoma [77], and pancreatic carcinomas [64]. They have been shown to be toxic to pancreatic tumors *in vivo* as well, shrinking the volume of a tumor by nearly 40% in one study [64]. This cytotoxicity is attributed to the CNPs ability to increase ROS levels and maintain them within the tumor cells. Even though there is conflicting evidence between the effect CNPs have *in vitro* and the toxicity results seen *in vivo*, their unique manner in the way they behave as an oxidant for tumor cells and as an antioxidant for normal cells establishes the need for further investigations of CNPs in research. Many radioprotectors are described by one antioxidant scavenger for every radical that's available to be scavenged. A single CNP, on the other hand, can scavenge multiple free radicals (or induce oxidation of multiple targets) because of its auto-regenerative capability. Also, with their regenerative antioxidant properties, CNPs would prevent the need for multiple treatments [81]. Ultimately, cerium oxide nanoparticles hold considerable potential for the possible applications within biomedical research.

1.11 Specific Aims

Within the scope of radiation therapy, there is demand for a novel approach that will improve tumor cell killing and protect normal cells while reducing negative side effects. Recently, there has been considerable attention given to nanoparticles due to their use in cancer therapy. Studies reveal that certain metal oxide nanoparticles can induce cytotoxicity in cancer cells, but not in normal cells [88]. Also, an effective radioprotector is essential for the future of space travel to protect astronauts from the tremendous amount of radiation accompanied by deep space missions [89]. Cerium oxide nanoparticles (CNPs) could be a promising candidate to meet the current needs in these fields. It is the basic goal of this investigation to study the characteristics of CNPs with charged particle radiation, in order to determine if they could act as radiosensitizers for cancer cells and/or radioprotectors to normal, non-malignant cells. The ultimate objective would be to find one of these nanoparticles that holds the synergistic effect of enhancing the rate of killing in tumor cells while simultaneously improving the surviving fraction of normal cells. One phase of this study concentrates on using CNP variations to investigate if a protective effect exists in the non-malignant 184A1 breast cell line. An additional phase of this study focuses on demonstrating that a sensitizing effect exists in the MCF7 breast tumor cell line counterpart and/or the 22RV1 prostate tumor cell line using distinctive CNP variations.

Specific Aim 1:

The first aim of this study was to determine if a specific CNP treatment can offer protection to the non-malignant 184A1 breast epithelial cell line when exposed to proton radiation. Non-malignant cells were treated with different types of varying concentrations

of CNP candidates 24 hours prior to radiation exposure to determine if a specific nanoparticle treatment could offer protective characteristics. The protection effect was assessed using MTT assay.

Specific Aim 2:

The second aim of this study was to verify that specific nanoparticle types would enhance the rate of killing in tumor cells when exposed to proton radiation. Varying types and concentrations of CNPs were administered to cells 24 hours prior to radiation exposure. Tumor cell viability was assessed initially with an MTT assay and measured using a clonogenic assay.

Chapter 2: Experimental Design and Methods

2.1 Cell Culture and Plating

Three primary cell lines were used over the course of our study. The 184A1 breast epithelial cell line (ATCC® CRL-8798™) was cultured using Mammal Epithelial Basal Medium (MEBM) complete media (minus gentamycin-amphotericin B) purchased from Lonza® and supplemented with 1 ng/ml cholera toxin and 0.005 mg/ml transferrin. This non-malignant, transformed cell line was established from the normal mammary tissue of a 21-year old female [90]. The 22Rv1 epithelial prostate carcinoma cell line (ATCC® CRL-2505™) was cultured using Roswell Park Memorial Institute (RPMI) complete media purchased from ATCC® and supplemented with a final concentration of 10% Fetal Bovine Serum (FBS). This malignant cell line was derived form a xenograft of human prostate [91]. The MCF7 epithelial breast adenocarcinoma cell line (ATCC® HTB-22™) was cultured using Eagle's Minimum Essential Medium (EMEM) complete media purchased from ATCC® and supplemented with 0.01 mg/ml human recombinant insulin and a final concentration of 10% FBS. This malignant cell line was established from the breast tissue of a 69-year old female [92].

Low passaged cells are frozen and stored in a liquid nitrogen cryogenic dewar container for future use. To thaw and continue a passage, a storage vial (containing roughly 10^5 cells) is brought to room temperature and the cells are diluted in media. The cryoprotective agent used in the freezing process is removed immediately by centrifuging

the cell suspension at approximately 125 x g for 10 min. The supernatant is discarded and the cell pellet can then be resuspended in fresh growth medium. Stock cultures are maintained in 75 cm^2 (T-75) culture flasks containing about 15 mL of media and incubated at 37°C in a 5% CO_2 environment until they reach 90% confluence. At that point, the cells are ready to use for the first step of the experiment.

On the day for the initial plating of the experiment, the media is aspirated off of our nearly confluent flask of cells. Then 10 mL of Phosphate-Buffered Saline (PBS) is added to wash the cells. After a wash, the cells are lifted via trypsinization. 1 mL of 0.25% Trypsin/EDTA (Ethylenediaminetetraacetic acid) solution (Invitrogen/Life Technologies,Inc.) is added and the cells are placed into the incubator. This helps the Trypsin work to detach the cells from the substrate. Observations of the cells indicate that they are fully trypsinized when they become rounded and detach from the flask when the flask is gently swirled. After the cells have lifted, 9 mL of complete media is added to the flask. This solution is mixed by pipetting up and down 20 times in order to break up clumps of cells and create a single cell suspension.

From the suspended cells, we take a sample 100 μL aliquot in order to perform a cell count. In an Eppendorf tube, 50 μL of the sample along with 50 μL of 0.4% Trypan Blue are mixed well, and a 10 μL aliquot of that is loaded into a hemocytometer slide. The loaded slide is placed under the microscope and the Trypan Blue-excluding cells are counted in square grid regions. An average is then calculated using the cell counts in each region. Knowing the cell count average and the volume of one of the grids, the cell concentration can be determined as follows:

avg x 2(Trypan Dilution) /Volume of grid(0.1cm x 0.1 cm x 0.01cm) = # Cells/mL

Each well that is used on the 48-well microtiter plates should have $2x10^4$ cells. Each well will also be seeded with 200 µL of suspended cells. This results in a concentration of ($2x10^4$ cells)/(0.2 mL) = $1x10^5$ cells/mL and a dilution factor equal to (counted # cells/mL)/($1x10^5$ cells/mL).

A minimum volume of (the # of wells that are receiving cells) x 200 µL is required, and the total volume of suspended cells that is prepared must be greater than the minimum volume required to allow for error when pipetting. Therefore each new suspension utilizes a total final volume that is greater than the minimum required volume. When a final amount is chosen the volume of original suspended cells to add to the new suspension can be determined,

(Total Final Volume)/(dilution factor) = (volume of suspended cells).

Then the volume of fresh media to add to the new suspension is what remains,

(Total Final Volume) – (Volume of suspended cells) = (Volume of fresh media).

These two volumes are transferred to a test tube and thoroughly mixed.

Once the appropriate cell dilution is created, the plates are seeded for the experiment. 200 µL of cell suspension is added to wells in a 48-well microtiter plate. The plates are then placed in the incubator at 37°C (5% CO_2) for 24 hours to allow the cells to adhere to the bottom of the plate. A diagram of the plating configuration is shown in Fig. 1. The reasoning for this configuration will be explained later.

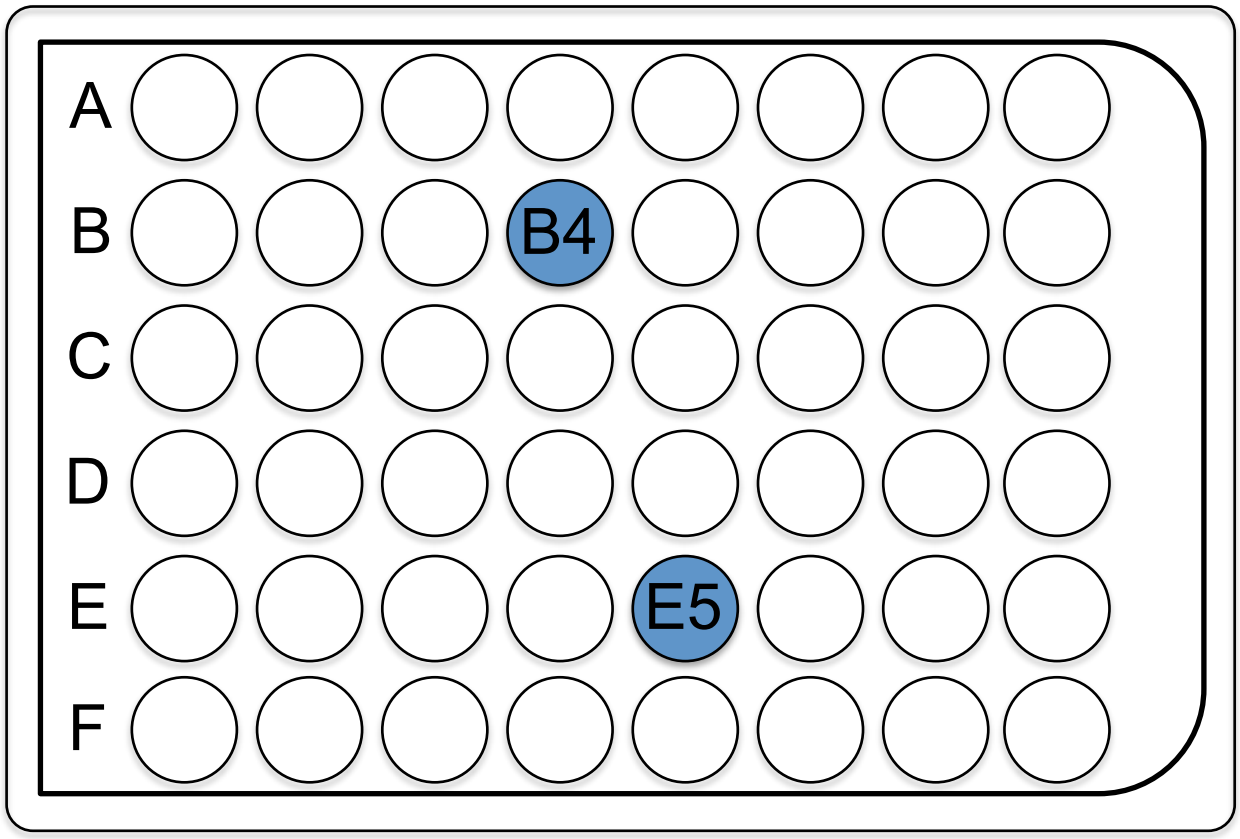

Fig. 1 Configuration for Seeding Cells in a 48 Well Plate

When plating is completed, a small split of suspended cells from the original T-75 flask is added to a new T-75 culture flask for the next experiment run. Enough fresh complete media is added to bring the total volume up to approximately 15 mL and the flask is then placed in the incubator and cells are incubated at 37°C (5% CO_2).

2.2 Adding Nanoparticles

The CNPs that were used in this study were fabricated at the University of Central Florida (UCF) NanoScience Technology Center (NSTC) and then transferred to ECU. There are several different methods of preparation that are used in order to achieve a certain effect when implemented with irradiated cells [18, 93]. These vacancy-engineered CNPs of interest are patented and therefore information about them is proprietary [94].

One method of their preparation uses a microemulsion technique that involves toluene, water, and surfactant sodium bis(2-ethylhexyl) sulfosuccinate (AOT) [18]. 2.5 mL of 0.1 M aqueous cerium nitrate solution is added to a mixture of AOT that is dissolved in 50 mL of toluene, and then stirred for 45 minutes. Using a drop method, 5 mL of 30% hydrogen peroxide is added and the subsequent reaction continues for one hour. Then the mixture is left to separate into layers, with the upper layer consisting of toluene and non-clustered ceria nanoparticles and the bottom layer containing the aqueous phase. 30% ammonia is added in order to precipitate the CNPs, and then they are washed with acetone and water to completely remove the surfactant. Then the CNPs are suspended at a 5mM concentration in deionized water.

Another method uses simple wet chemical procedures and yields CNPs with a higher surface Ce^{3+} concentration. In this preparation, cerium nitrate hexahydrate is first dissolved in deionized water. To remove undissolved impurities, the solution is then filtered using a 20 nm filter. The cerium solution is oxidized using hydrogen peroxide and then stirred overnight. Afterwards, the CNPs are dialyzed against deionized water to remove excess oxidizers and nitrate ions from the solution. A similar type preparation is

used to produce CNPs with a higher surface Ce^{4+} concentration, with the only change in methodology being ammonium hydroxide is used instead of hydrogen peroxide [65, 72].

To properly characterize the CNPs, x-ray photoelectron spectroscopy (XPS) and high-resolution transmission electron microscopy (HRTEM) were used. These CNPs have been characterized as ultrafine, being uniformly distributed, and having nanocrystallinity [17, 95]. The physiochemical properties of these CNPs reveal that they are spherical in shape, having a crystalline fluorite structure with diameters ranging from 5-18 nm and they have hydrodynamic sizes of 10-350 nm in ddH_2O (double-distilled water) depending on their morphology [84, 93]. Oxygen vacancies that are created by surface chemical reactions allow Ce^{3+} to be present in the CNP crystal lattice [96]. An XPS spectrum of the synthesized CNPs shows distinctive peaks that demonstrate the presence of the mixed valence (Ce^{3+} and Ce^{4+}) state [17].

After the plated cells have incubated overnight, the nanoparticles are added to each well at appropriate concentrations. The stock CNPs are sonicated prior to use with a Sonic Dismembrator (Fisher Scientific™ Model 50) for 2-3 minutes at 25% power. Concentrations ranging from 10 nanoMolar(nM) to 10 microMolar(μM) are required for each well receiving the nanoparticle treatment. The initial 5 miliMolar(mM) concentration of suspended nanoparticles requires that serial dilutions be performed for each nanoparticle type used.

The serial dilution process begins by labeling five tubes with the nanoparticle type followed by A, B, C, D, or E. Then 0.9 mL of media is added to each of the five tubes. 0.1 mL of the 5 mM suspended nanoparticles is added to tube A and mixed thoroughly. Then 0.1

mL of the diluted suspended nanoparticles from tube A is added to tube B. After mixing well, 0.1 mL of the diluted suspended nanoparticles from tube B is added to tube C. Once this is fully mixed, the suspension in tube C is now at a 5 μM concentration. This procedure continues for tube D and E. Once this is fully mixed, the suspension in tube E is now at a 50 nM concentration. Then 50 μL of the diluted suspended nanoparticles from each tube is added to each appropriate well of the 48-well microtiter plate. A diagram of the serial dilution process is shown in Fig. 2.

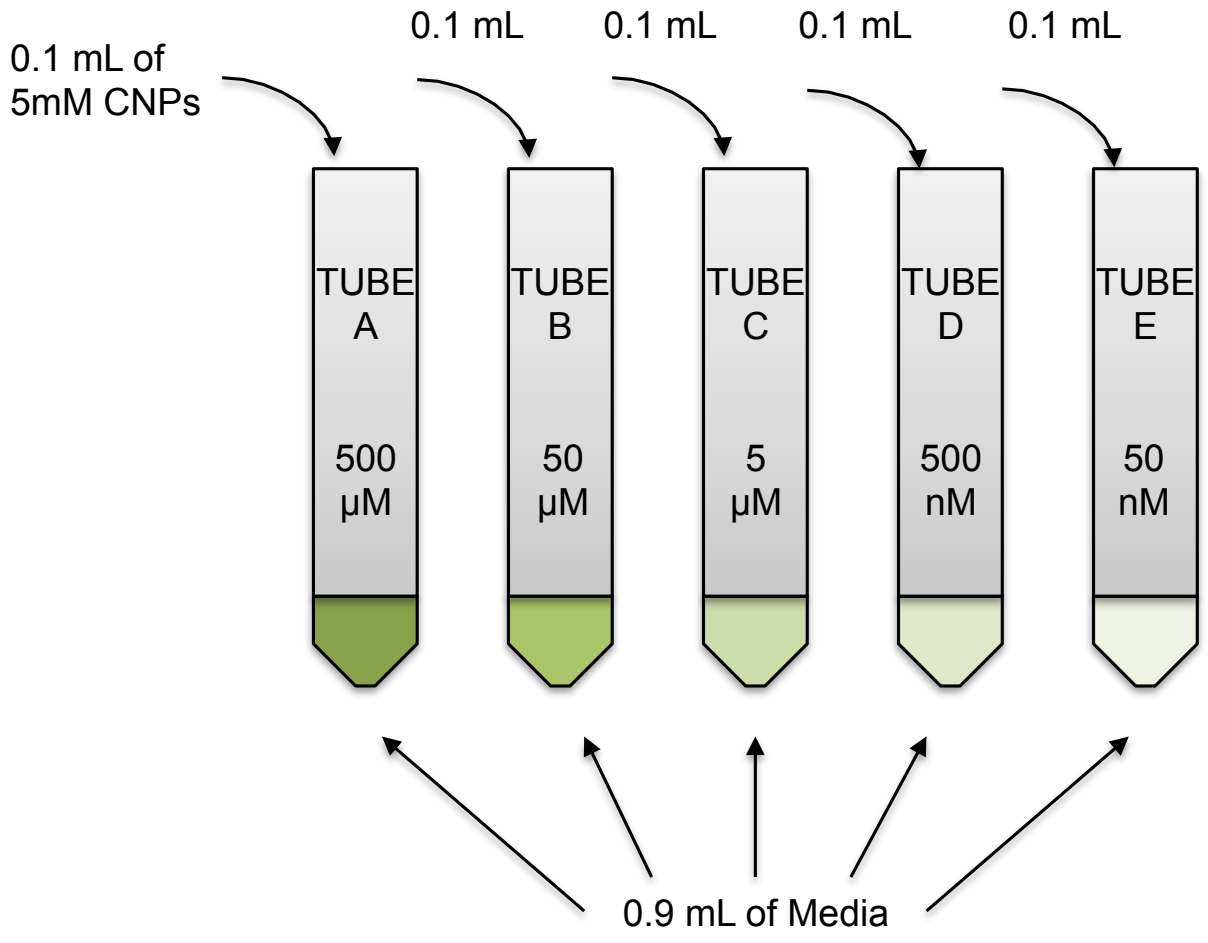

Fig. 2 Serial Dilution Process

Each well had 200 μL of media before the addition of nanoparticles from plating day. The addition of the 50 μL of diluted suspended nanoparticles results in a final volume of 250 μL and a nanoparticle dilution ratio of 1:5 from any of the prepared tubes previously described. For example, the 5 μM concentration from tube C becomes a 1 μM final concentration once added to the appropriate well. In order to ensure equal volumes in all appropriate well plates, 50 μL of complete media is added to the wells that did not receive nanoparticles. The plates are then returned to the incubator at 37°C (5% CO_2), and the cells are allowed to absorb the nanoparticle treatment for 24 hours.

2.3 Proton Irradiation

The Accelerator Laboratory at East Carolina University houses a 2 MV tandem Pelletron accelerator that is capable of producing ion beams with diverse energies and charge states for the purpose of studying atomic collisions [97]. For this study, the accelerator is operated to create a proton beam that traverses through vacuum, using steering and focusing instruments, to an exit point where the biological samples are exposed. The schematic of the accelerator system is shown below in Fig. 3.

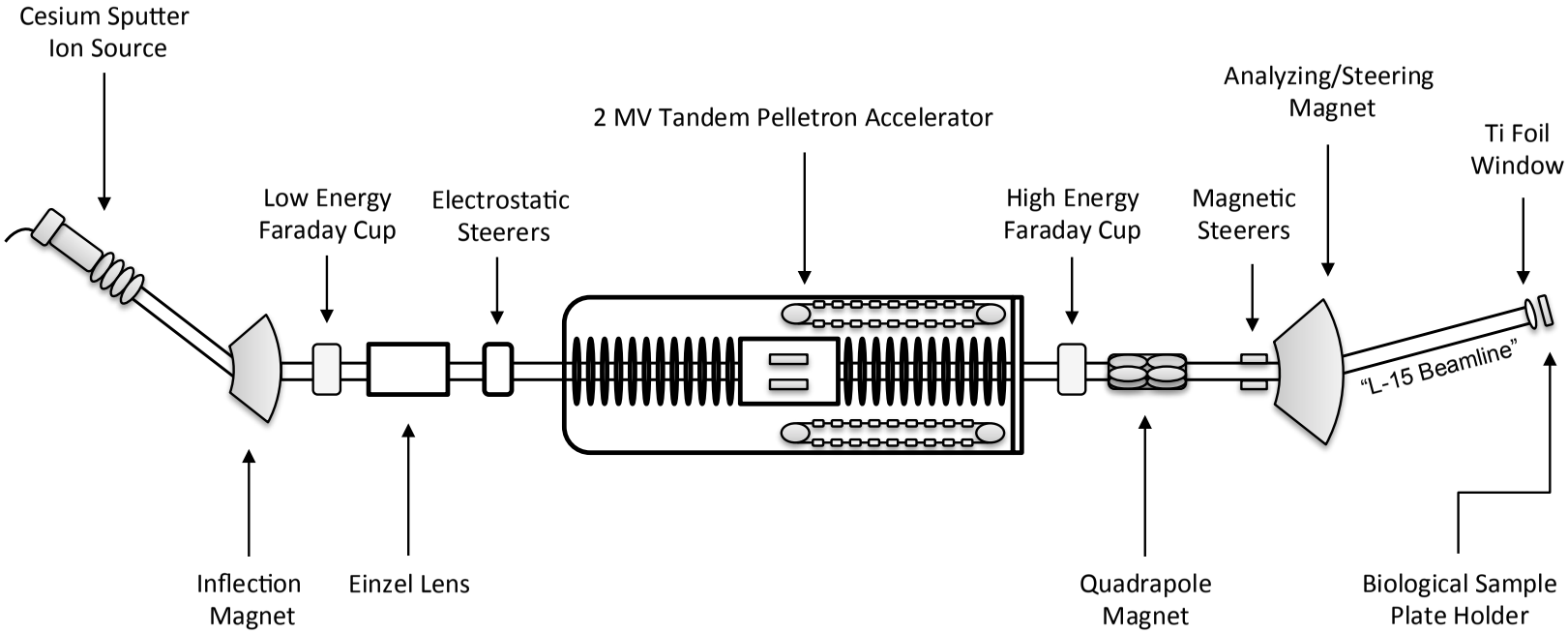

Fig. 3 ECU Particle Accelerator

This process of creating and harnessing the ion beam starts with the cesium-sputter ion source (Ionex Corporation model 860A). This source is capable of producing various atomic and molecular ions as well as negative ion beams in the microampere range [98, 99]. This particular ion sputter source and the list of potential ions available to be produced with their relative abundances have been well documented [100]. First, a cesium oven reservoir is heated in order for cesium vapors to migrate into the ion source chamber that contains a copper cathode and heated ionizer. Cesium vapors come in contact with the heated ionizer coil becoming positively ionized Cs^+. The cathode is held at a negative potential and therefore attracts the Cs^+ ions. These Cs^+ ions, due to their momentum, will sputter off atoms when they slam into the cathode material. When these atoms penetrate through the condensed cesium, an electron is captured in the process and produces negative ions, which form the initial beam. In this particular study, protons are appropriate for investigation. Therefore, H^- ions are produced using a cathode material comprised of Titanium Hydride (TiH). The cathode itself is 10 mm wide and 12.5 mm long with a cone shaped front that has a 1.6 mm well drilled 5mm into its center. This well is tightly packed with TiH powder. These ions are focused into a beam dictated by the defined potential surfaces of the cathode and ionizer potentials, while other ions (including Cs^+ ions) are scattered.

A 30 kV potential initially extracts the negative ion beam along a 1 m region and the beam is focused with an electrostatic Einzel lens. The Einzel lens can vary the surrounding electric field to focus the beam using ion optics [101]. The H^- ions are then selected based on their momentum with an inflection bipolar magnet and then focused again using another Einzel lens followed by a pair of electrostatic steerers. Then the H^- beam is injected

into the 2 MV tandem Pelletron accelerator (National Electrostatic Corporation model 6SDH-2).

Electric charge accumulates in the accelerator vessel by means of two Pelletron chains in a closed pulley system. The chains are metal pellets connected by nylon links. In this system, a negatively charged inductor pushes electrons off the pellets while they are in contact with the grounded drive pulley. They retain their charge as they exit the inductor and continue on to the high voltage terminal where the reverse process takes place. The chain passes through a suppressor to prevent arcing as the pellets deposit positive charge onto the terminal pulley [102]. This is an enclosed system operating inside a pressurized tank that contains up to 550 kPa of SF_6 insulating gas to prevent discharge.

As the ion beam enters the accelerator, the H^- ions are attracted to the positive high voltage terminal. In the center of the vessel, nitrogen gas (N_2) is present that strips off electrons from the H^- ions making them positively charged H^+ ions (protons). Then the positive ions are accelerated again as they are repelled towards the ground potential, completing the tandem process of acceleration. Using this technique, the accelerator at ECU can generate singly charged ions up to 4 MeV. The National Electrostatic Corporation (NEC) details the design and operation of these type accelerators [103].

As H^+ ions exit the accelerator, the beam is focused with a pair of quadrupole magnets. An analyzing magnet selects the beam of the appropriate mass to charge ratio and steers it down the left 15° beamline to the biological samples. A diagram of the 15° beamline is shown in Fig. 4.

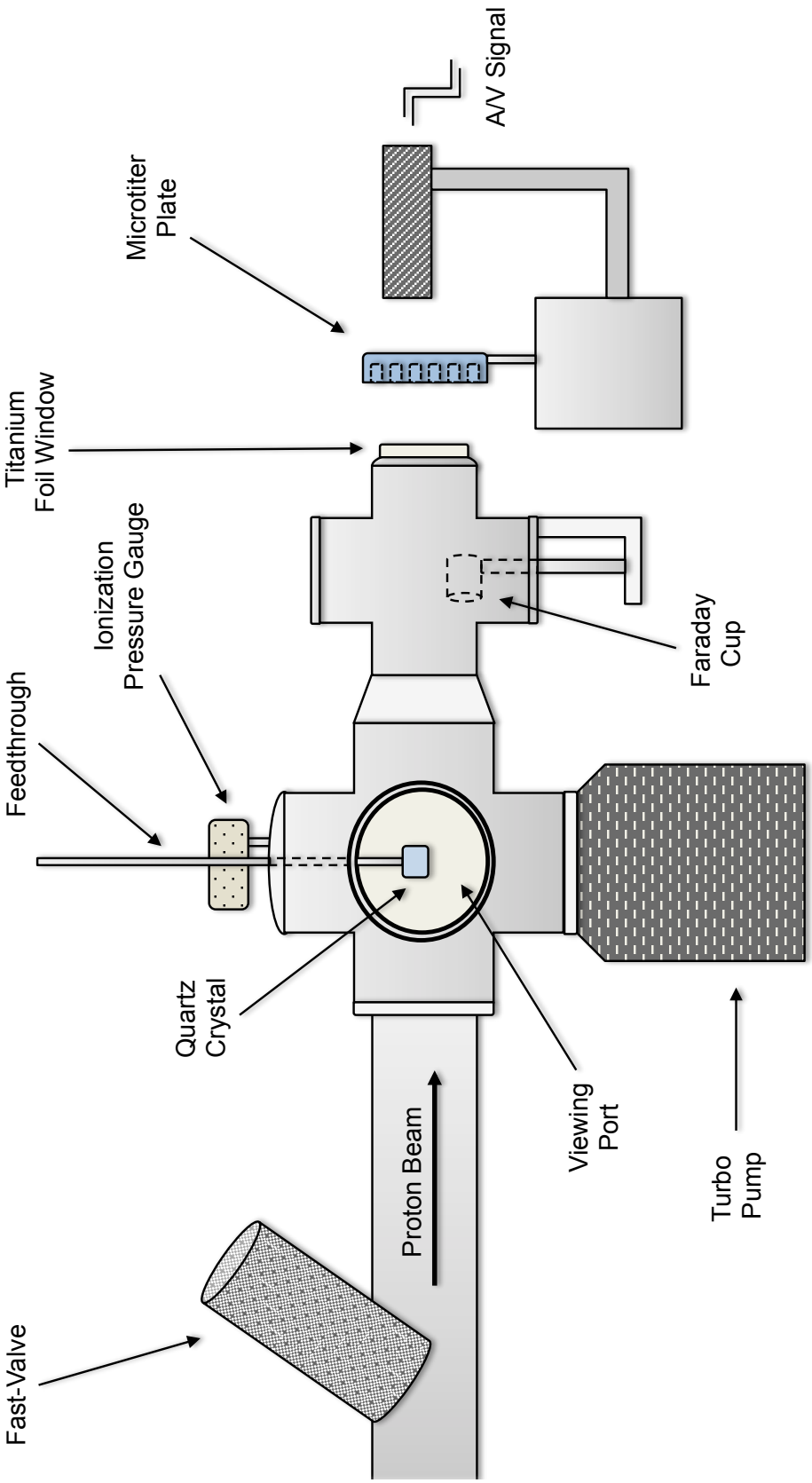

Fig. 4 Side View of the Left 15° Beamline

The pressure in the experimental beamline is maintained around the 10^{-7} torr range with a turbomolecular pump and an ionization pressure gauge is used to measure and monitor the vacuum pressure. Inside the ion gauge, a heated filament releases electrons that are attracted to a positively charge grid. The electrons can collide with gas molecules on their way to the grid creating gas ions. These gas ions are collected with a negatively charged wire and the resulting current can be measured to determine the vacuum pressure. A fast-shut valve is mounted upstream in the beamline so that if there were a sudden loss of pressure it would trigger to preserve the vacuum further up the line. Down the beamline, a feedthrough block is positioned with a quartz crystal attached that will fluoresce when exposed to the beam. The beam spot can be seen through the viewing window on the side of the beamline. The beam current can then be measured with a Faraday cup that is mounted on the beamline right before the beam exits through a 12.5 μm titanium foil vacuum window into open air. The titanium foil is epoxied to a brass beamline blank with a 1.4 cm aperture drilled in the center. This window is appropriately small as to limit the amount of energy loss of the ion beam due to nuclei interactions in the foil. As the beam exists the foil, it propagates through open air before reaching a monolayer of cells in the center of a well on a 48 well microtiter plate. A picture of the end of the L15 beamline is shown in Fig. 5.

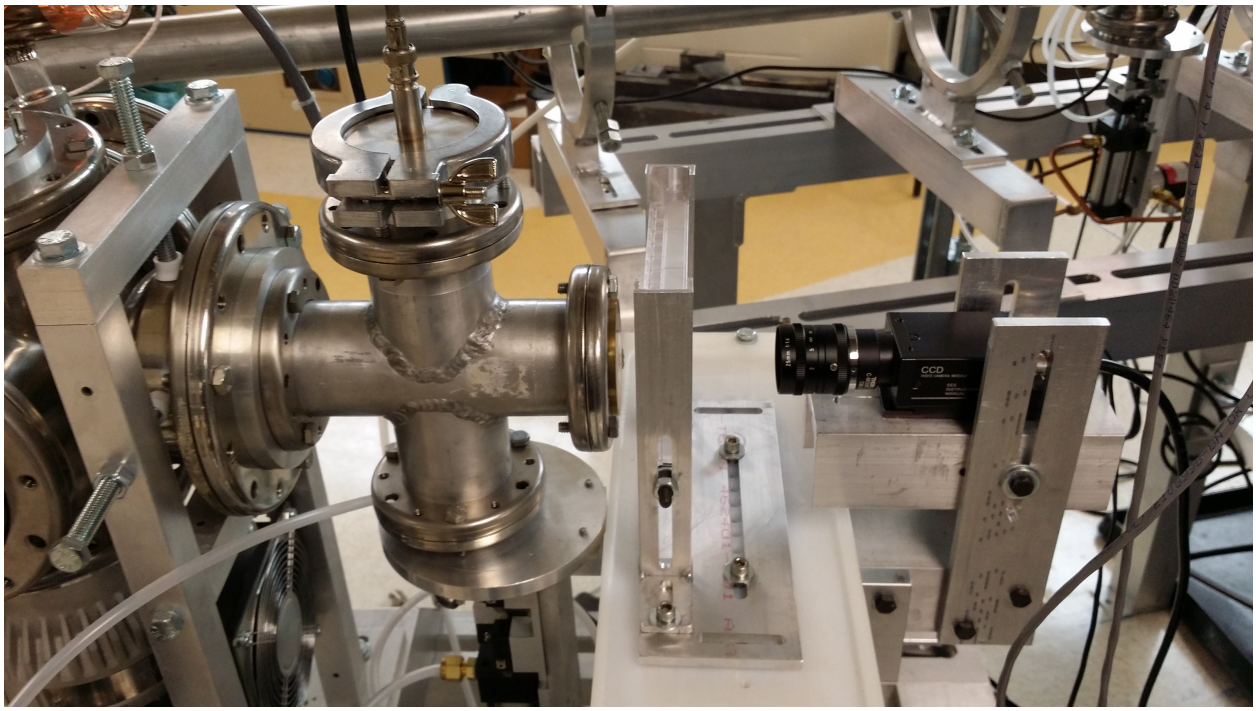

Fig. 5 A picture of the target that is held at the end of the L15 beamline. A vacuum window is attached to the end of the four-way cross. The beam exits the window and strikes the biological sample in the 48-well plate.

To ensure the uniformity of the beam, the beam intensity profile is imaged using a cerium-doped yttrium aluminum garnet (YAG) crystal. This crystal scintillates when exposed to charged particles. It is specifically placed at the location where the cells are irradiated and is fixed in a 48-well microtiter plate sample to simulate a monolayer of cells at the bottom of one of the wells. A diagram is shown in Fig. 6 of the exact location of the YAG crystal in the E5 well of the sample plate.

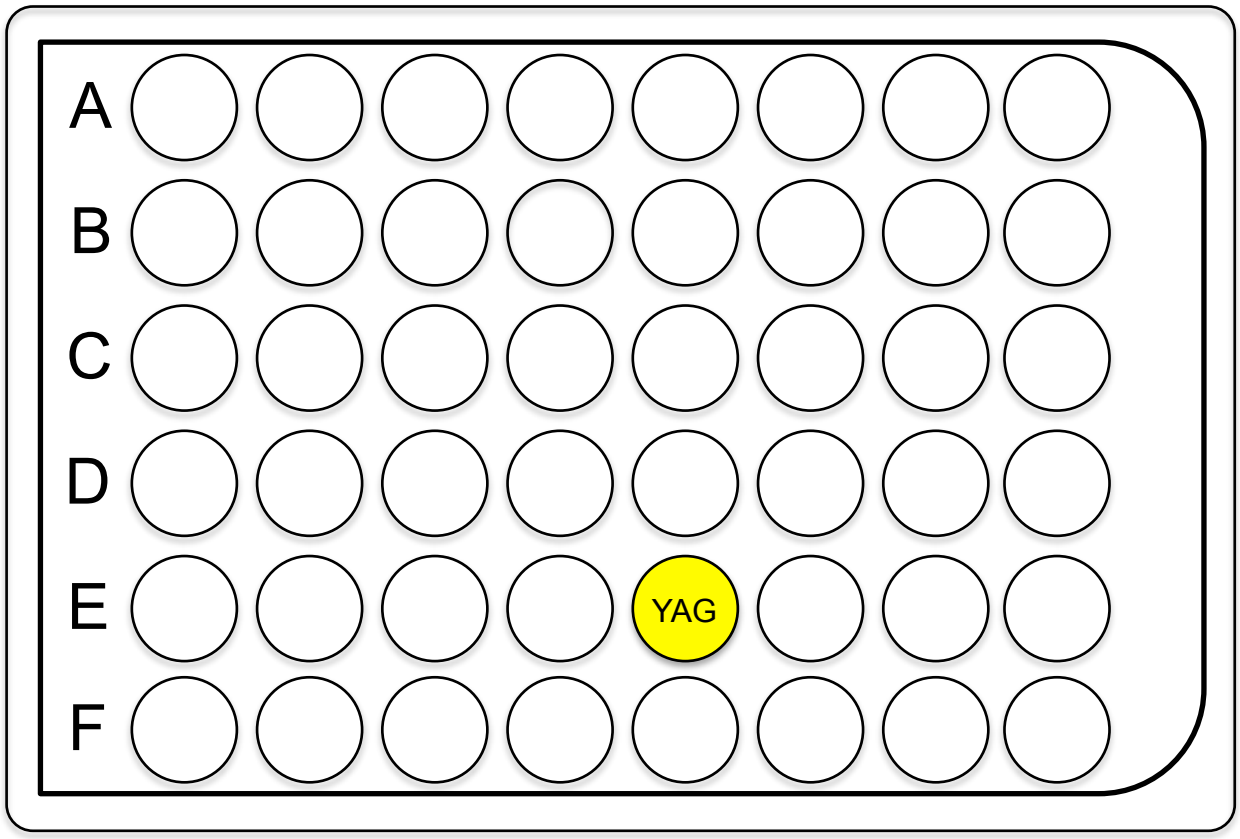

Fig. 6 A depiction of the positioning of the YAG scintillation crystal in the E5 well of a sample plate.

In this arrangement, a 180 degree rotation of the plate allows the B4 well to be in line with the beam. This current setup allows for two irradiated wells per plate. A camera was mounted directly behind the plate holder and focused on the well containing the YAG crystal. This camera allows an image to be captured using XCAP® for Windows. The image can then characterized using ImageJ, a public domain Java based script program developed at the National Institute of Health [104]. ImageJ is used to process and display the image as a 3D representation that shows deviances in the scintillation of the crystal, which indicates variations in the beam flux. The beam intensity profile can then be adjusted with the

quadrupole magnets and electrostatic steerers to obtain the desired uniformity. A visual of the scintillation and capturing process is shown in Fig. 7. A sample representation of the beam intensity profile adjusted for uniformity is shown in Fig. 8.

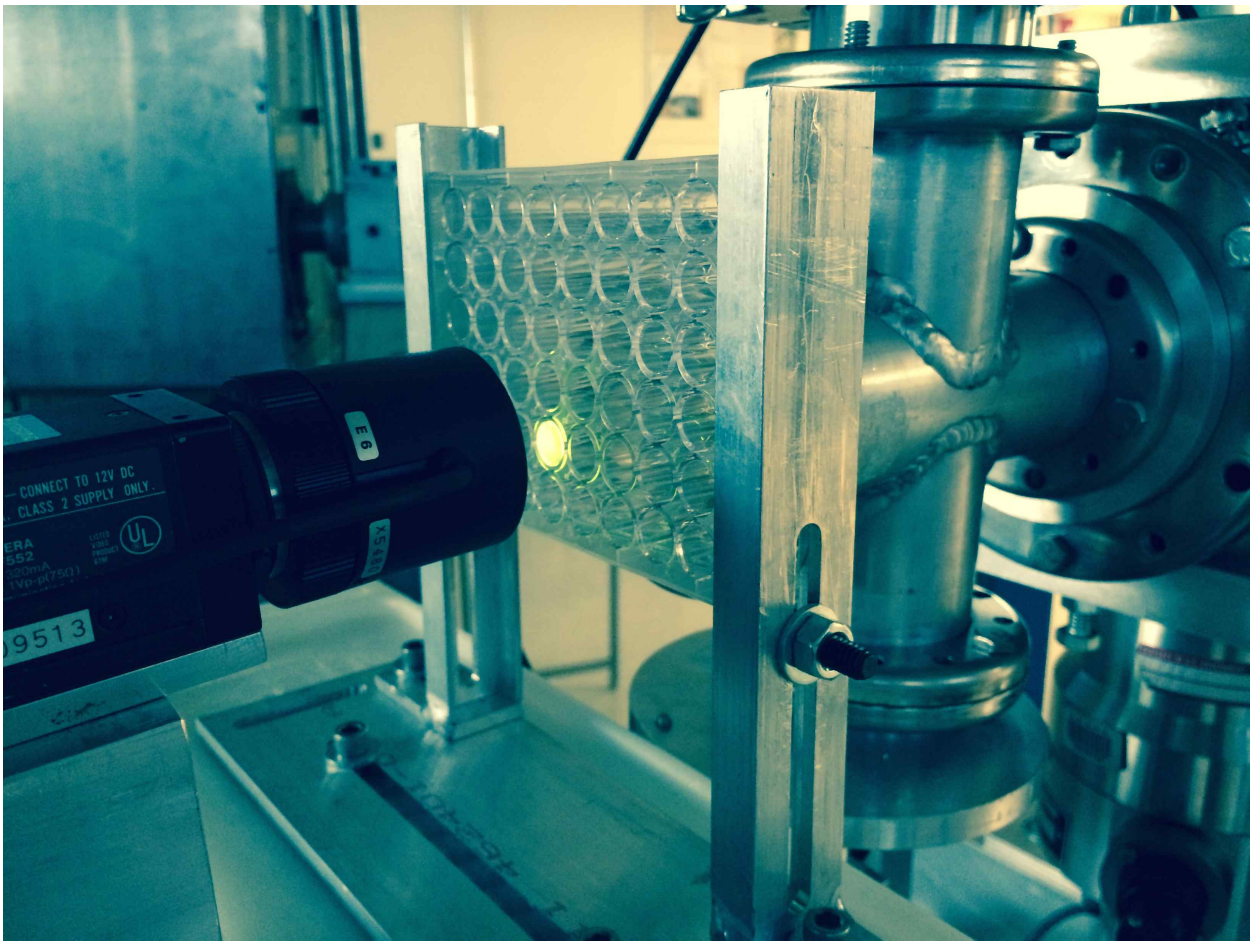

Fig. 7 A visual of the scintillation and image capturing process that occurs in order to characterize the beam intensity profile.

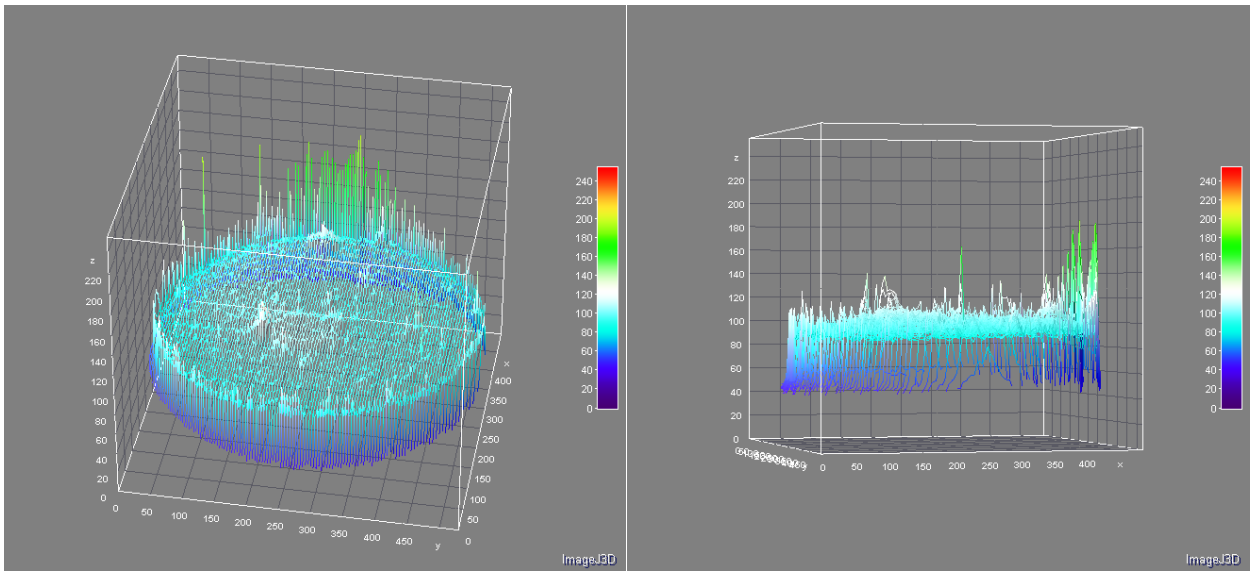

Fig. 8 An example of the intensity profile from the cerium-doped YAG scintillation crystal bombarded with protons adjusted for uniformity. This image was taken with a camera at the end of the beamline and then processed using ImageJ software.

While adjusting the beam uniformity, it is also necessary to verify a steady beam current in time in order to avoid a surge that would cause a spike in the dose received by our samples. This usually requires waiting long periods of time in between each tuning of a parameter for the beam to stabilize.

With the beam uniformity in place, the dose can be calculated using equation 1.3. The dosimetry is determined using the measured beam current of the faraday cup, the beam profile, and the calculated energy deposition using the stopping powers predicted by Stopping and Range of Ions in Matter (SRIM) code [19]. The SRIM code gives the stopping power and range of ion into matter at energies up to 2 GeV/amu through means of a quantum mechanical treatment of ion-atom collisions and uses statistical algorithms that average the results from calculated ion collisions to use throughout the intervening gaps

[19]. The SRIM program uses this treatment for various types of material.

To define the dose received by the cells, the LET of the beam must first be calculated to determine the energy lost to each material traversed by the beam. The stopping power and density are used to establish the LET of the first material as follows.

$$LET = \left(-\frac{dE}{\rho dx}\right) * \rho \tag{2.1}$$

Then the material's thickness is used to determine the energy loss of the beam as it exits the medium.

$$E_{loss} = LET * \Delta x \tag{2.2}$$

Now the remaining energy of the beam can be calculated and used as the starting value for the next LET calculation.

$$E_{remaining} = E_0 - E_{loss} \tag{2.3}$$

This process continues for each subsequent material that the beam encounters along its path. The beam initially crosses the 12.5 μm titanium foil window before traveling 3.1 cm of air into a single layer of identical epithelial cells with a presumed thickness of 5 μm that is consistent with comparable studies [105, 106]. This generalization is necessary in determining a relative dose to the cells, however in reality the cells vary in shape and size but this variance is not critical and the estimation is sufficient for dose calculations. A schematic of the spacing at the end of the beamline is shown in Fig. 9.

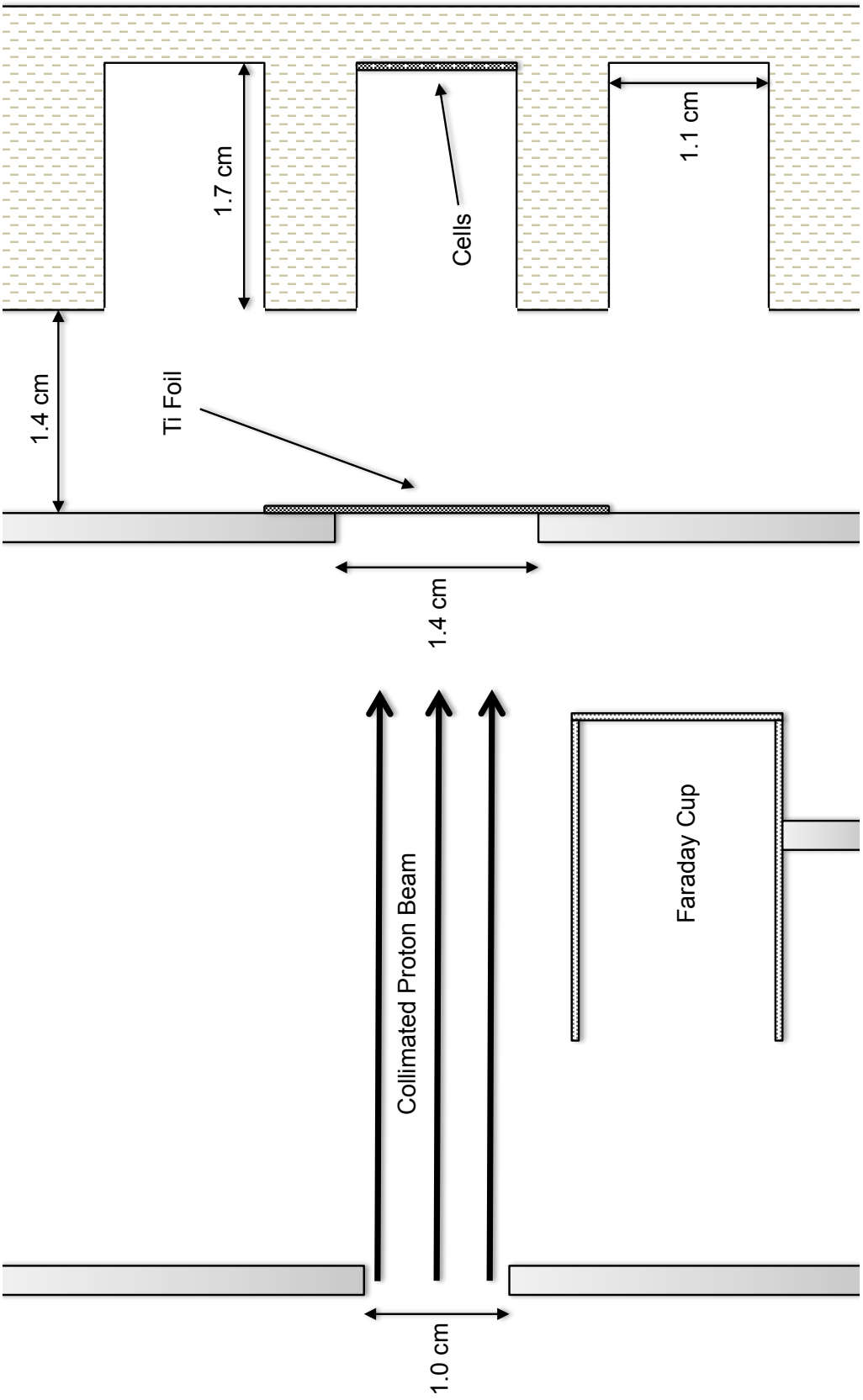

Fig. 9 A representation of the layout and exact measurements at the end of the L15 beamline.

For the 3 MeV protons that were used in this study, the energy loss in the foil was determined to be 13%. The energy loss of the beam to the air was determined to be 19%. This resulted in an incident energy on the cells that was approximately 1 MeV less than the initial beam energy in the beamline prior to exiting vacuum.

The dose rate was determined at the midpoint of the cell using the mass stopping power (dE/ρdx) and the fluence rate ($\dot{\varphi}$) from the measured current in the faraday cup.

$$\dot{D} = \dot{\varphi}\left(\frac{dE}{\rho dx}\right) * 1.6\times10^{-7} \tag{2.4}$$

Since the mass stopping power is measured in MeV cm^2/mg and the fluence rate has units of cm^{-2} sec^{-1}, a conversion factor of 1.6×10^{-7} is needed to convert MeV/mg to the standard unit of dose Gy (J/kg) and produce a dose rate that is measured in Gy/sec. Analyzing the dose rate at the midpoint of the cell is consistent with previous studies [106-108].

This dose rate is used to calculate the correct beam exposure time needed for the cells to receive a prescribed dose of radiation. The samples can then be exposed using the Farady cup as an open/close shutter valve, controlling the amount of time it stays open with a computer-operated precision timer.

Once the proton beam has been stabilized on target, every setting has been optimized to create uniformity, and the dose is calculated, then the cells are ready to be irradiated. First the cells are washed with media, being certain not to cross contaminate between the wells. Then the cells in their well plates are transported to the accelerator lab. Even the non-irradiated plates are transported along with the rest of the other plates to the

accelerator lab to ensure that all groups are treated equally.

The appropriate plates are irradiated with an external proton beam that is extracted at the exit point through the titanium foil window. The plates are randomized and exposed as quickly as possible to minimize the time that the cells sit without media. During this process, the beam current is monitored for stability. If there is even a slight fluctuation, the dose time is recalculated to guarantee that all of our samples receive the same relative dose. Once the irradiation is completed, the cells are immediately transported back to the cell culture lab. Each well is brought back up to a volume of 200 μL with fresh complete media. The plates are then returned to the incubator and cells are allowed to incubate at 37°C (5% CO_2) and recover for 24 hours. It is at this point in the experiment that samples are handled according to which assay is to be performed.

2.4 MTT Assay

The Microculture Tetrazolium Technique(MTT) assay was used to assess cell viability after exposure to radiation. For 184A1 cells, the MTT assay was performed 24 hours after irradiation. For the 22Rv1 and MCF7 cells, the MTT assay was performed 72 hours after irradiation. It is a colorimetric assay that measures cell viability by the reduction of tetrazolium salts. For this study we used Thiazolyl Blue Tetrazolium Bromide MTT (3-(4,5-Dimethyl-2-thiazolyl)-2,5-diphenyl-2H-tetrazolium bromide) purchased from Sigma-Aldrich®. The cells that are metabolically active will reduce the MTT using dehydrogenase enzymes yielding intracellular purple formazan. The amount of purple formazan produced can be quantified using spectrophotometry. The ending result from

this assay describes metabolic activity and also lack of activity due to events such as apoptosis, necrosis, cell arrestment, etc.

The assay is performed as follows. 44.5 µL of 5 mg/ml MTT reagent (dissolved in PBS) is added to every well in the experiment (including two background control wells on each plate). Then the cells are allowed to incubate at 37°C (5% CO_2) for about 3 hours. After this incubation time, the media is removed carefully from each well as to not disturb the purple crystal precipitate at the bottom. Then 400 µL of 100% 2-propanol is added to every well to resuspend the purple crystals. The contents of each well are mixed until the crystals are completely dissolved. Once these suspensions are complete, they are measured for their absorbance in a Tecan plate reader (Infinite 200PRO). The absorbance is measured at a wavelength of 570 nm using the Magellan™ software program and the values are exported to an Excel spreadsheet.

The percent of the primary control was calculated for each experimental group. First the average absorbance values for the background wells were subtracted from the all other values. Then the average values for each experimental group were calculated and divided by the primary control group average. This normalizes the primary control group to 100% and represents the other experimental groups as a percent of that primary control. The standard error that was calculated for each group is represented as the standard deviation divided by the square root of the sample size. For the normalization, these errors were added in quadrature. A typical layout for this type assay included 6-8 samples per experimental treatment.

2.5 Clonogenic Assay

The clonogenic (or colony) assay was used to assess cell proliferation in tumorous populations after radiation exposure. To perform the colony assay, a small amount of a sample population in the well of a 48-well plate is seeded into the well of a 6-well plate. In order to do this properly, a serial dilution must be performed. Since the cells at the beginning of the experiment were initially plated with an approximate density of $2x10^4$ cells/well, and since Rv1 cells (for example) have a theoretical doubling time of around 40 hours [109], then after accounting for the initial lag phase of plating, at least one population doubling has completed since the initial plating. This results in an estimated $4x10^4$ cells being present in the wells of the control plates. Using this estimated density, a serial dilution is performed to reduce the number of cells per well to an order of magnitude closer to the targeted final seeding density of 200 cells per well. To avoid confusion, the wells that were originally plated with cells and media are referred to as the "sample wells" and the wells in the serial dilution are referred to as wells A and B, respectively. The final seeding is prepared in 6-well plates.

For each well on every plate that has cells and media, two other empty wells are chosen on the same plate to use for a serial dilution (referenced hereafter as wells A and B, respectively). The media from the sample well is transferred to well A in the series. Then 100 µL of 0.25% Trypsin (w/ EDTA) is added to each sample well. The plates are allowed to incubate for about five minutes or until cells in each sample well become rounded and detach when the plate is lightly shaken. Then 700 µL of fresh complete media is added to each sample well and the contents of each well are mixed up and down 20 times with the

pipette to break up cell clusters. The cells are then suspended in the media. The contents of each sample well are then transferred to its associated well A. This results in well A having a total volume of 1 mL (200 µL of original media, 100 µL of Trypsin, and 700 µL of fresh media). The contents of well A are mixed up and down 20 times with the pipette.

After the contents are mixed, 100 µL of suspended cells is taken from well A and deposited to each corresponding well B in triplicate. Also 900 µL of fresh complete media is added to well B and mixed up and down 20 times with the pipette, bringing the total volume up to 1 mL. At this point, in each well B, the number of cells has been reduced to approximately 4000 cells. Then we take 50 µL of suspended cells from each well B to separate wells on 6-well plates and label the new plates accordingly. This process results in a targeted final seeding density of 200 cells per well. Roughly 2 mL of fresh complete media is then added to each well on the new 6-well plates for the colonies to grow. All of the 6-well plates are then placed in the incubator and the cells are allowed to incubate at 37°C (5% CO_2) for at least 10 days, or until the wells develop scorable colonies. A diagram of the serial dilution process within the 48 well plates is shown in Fig. 10.

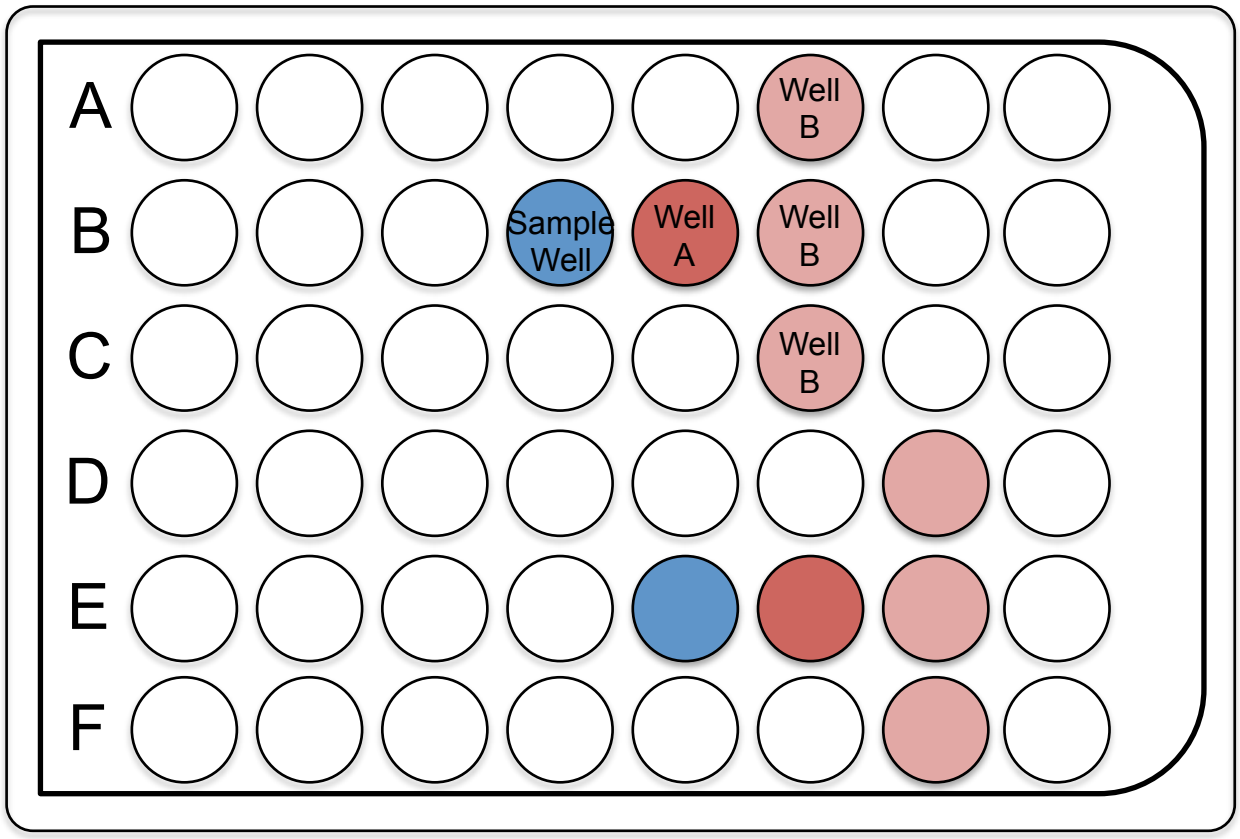

Fig. 10 The explicit configuration selected for lifting and diluting the irradiated cell population within a 48-well plate. The serial dilution process is performed in triplicate for each sample well.

Colonies are considered scorable when they are comprised of at least 50 cells, which indicates that the originally plated cell has undergone at least six cycles of division. 22RV1 cells, for example, have a theoretical doubling time of around 40 hours [109], thus requiring approximately ten days, without accounting for the lag time after plating. The best time to proceed with counting colonies can be determined by monitoring the cells in the non-irradiated control wells.

Once the colonies look ready for counting, the media from all the wells is aspirated. Then 1 mL of 10% NBF (Neutral Buffered Formalin) is added to each well in order to fix the

colonies. The colonies are allowed to sit in the formalin for approximately 30 minutes. Afterwards the colonies are stained with 1 mL of 0.01% (w/v) crystal violet and allowed to sit for approximately 60 minutes. Then the excess is aspirated, and all the wells are allowed to dry out completely. Once the plates are dry every well is individually imaged and each image file is named appropriately to indicate the group that the imaged well belonged to. Finally, the scorable cell colonies are counted and recorded.

The percent survival of the primary control was calculated for each experimental group. First the plating efficiency was calculated to determine what percentage of cells that were seeded would grow into colonies due to the plating process alone. This is coming from the primary control group, without any experimental treatment, that just goes through the process of the assay, e.g. lifting, diluting, replating. The plating efficiency is calculated as (the # of colonies counted)/(the # of cells seeded). Once an average plating efficiency is determined, the percent survival in an experimental group is calculated as follows, (average # of colonies counted)/(# of cells seeded x average plating efficiency). The standard error that was calculated for each group is represented as the standard deviation divided by the square root of the sample size. For the normalization, these errors were added in quadrature. A typical layout for this type assay produced 12 samples per experimental treatment.

The complete experimental setup is rather lengthy. If there are no hindrances, then a single data set can occupy from one week (MTT assay) up to three weeks (colony assay). A generalized overview for the entire experimental design is shown in Fig. 11.

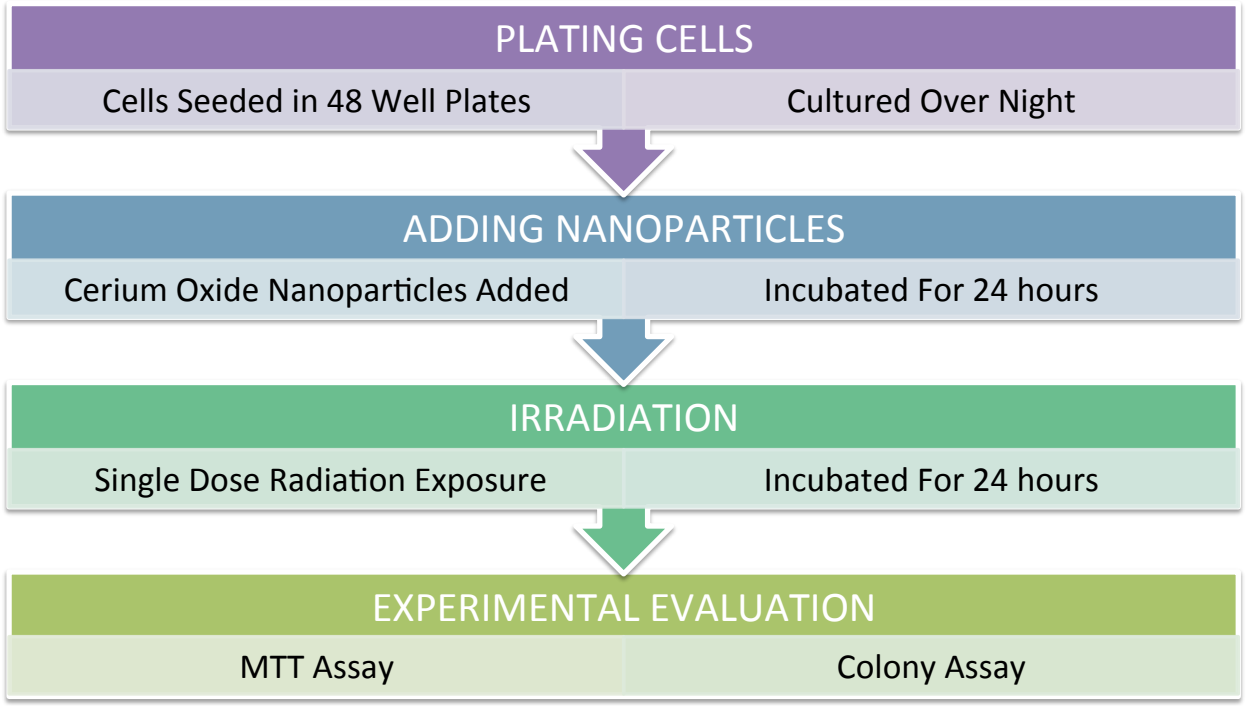

Fig. 11 A diagram of the main steps involved in the experimental design. This protocol typically takes 1-3 weeks to produce a single dataset.

2.6 Estimation of Nanoparticle Uptake

Gold type nanoparticles (GNPs) were brought into this study as a hopeful benchmark for sensitization. GNPs have been shown to sensitize tumorous cells due in part to their secondary electron emission properties [50-55]. 1.9 nm GNPs ordered from AuroVist™ Nanoprobes were used to investigate this effect, however the initial experiments performed with the MTT assay quickly failed. The resulting absorbance values were skewed due to the presence of the GNPs and their inherent metallic properties. There was motivation to create an assay as a way to determine how much of gold-type nanoparticles were contributing to the absorbance values themselves. If an absorbance value can be determined that is due solely from the presence of the GNPs inside the cells, then this can

be subtracted from the original readings to get more accurate absorbance values. This would ultimately have the potential to indicate the amount of nanoparticles taken up by the cells.

The experimental design is shown in Figure 12. The alphanumerical labeling on the 48-well microtiter plate was used to correspond to different treatments. It was decided that each column on the plate (A through F) would contain all experimental groups needed for one sample, this way the plate could produce 8 columns of samples for a desired nanoparticle type or concentration. Row A contained media only, while row B contained media plus nanoparticles. Row C contained media and cells. Rows D and E were treated the same initially, both containing media, cells, and nanoparticles. Row F was intentionally left empty in the beginning. Since irradiation was not required to do this study, it became a fairly simple process occurring over the course of 3 days.

On the first day of this experiment, cells are plated using the same protocols as before. Rows A and B receive 200 µL of media only, while rows C, D, and E are seeded with 200 µL of suspended cells. The plates are then placed in the incubator at 37°C (5% CO_2) for 24 hours, giving the cells plenty of time to adhere. On the second day, nanoparticles are added in desired concentrations. Rows B, D, and E receive 50 µL of suspended nanoparticles. Rows A and C are given 50 µL of media in order to ensure that all the wells have an equal volume of 250 µL. The plates are then placed in the incubator at 37°C (5% CO_2) for 24 hours, allowing plenty of time for the uptake of nanoparticles to take place. On the third day, the media from row E is transferred to row F, which was strategically left empty for this very step. Then an equal volume of fresh media (250 µL) is added back to

row E. At this point the plates are ready to be scanned. The plates are scanned in the Tecan plate reader, absorbance is measured at a wavelength of 570 nm, and the values are exported to an Excel spreadsheet.

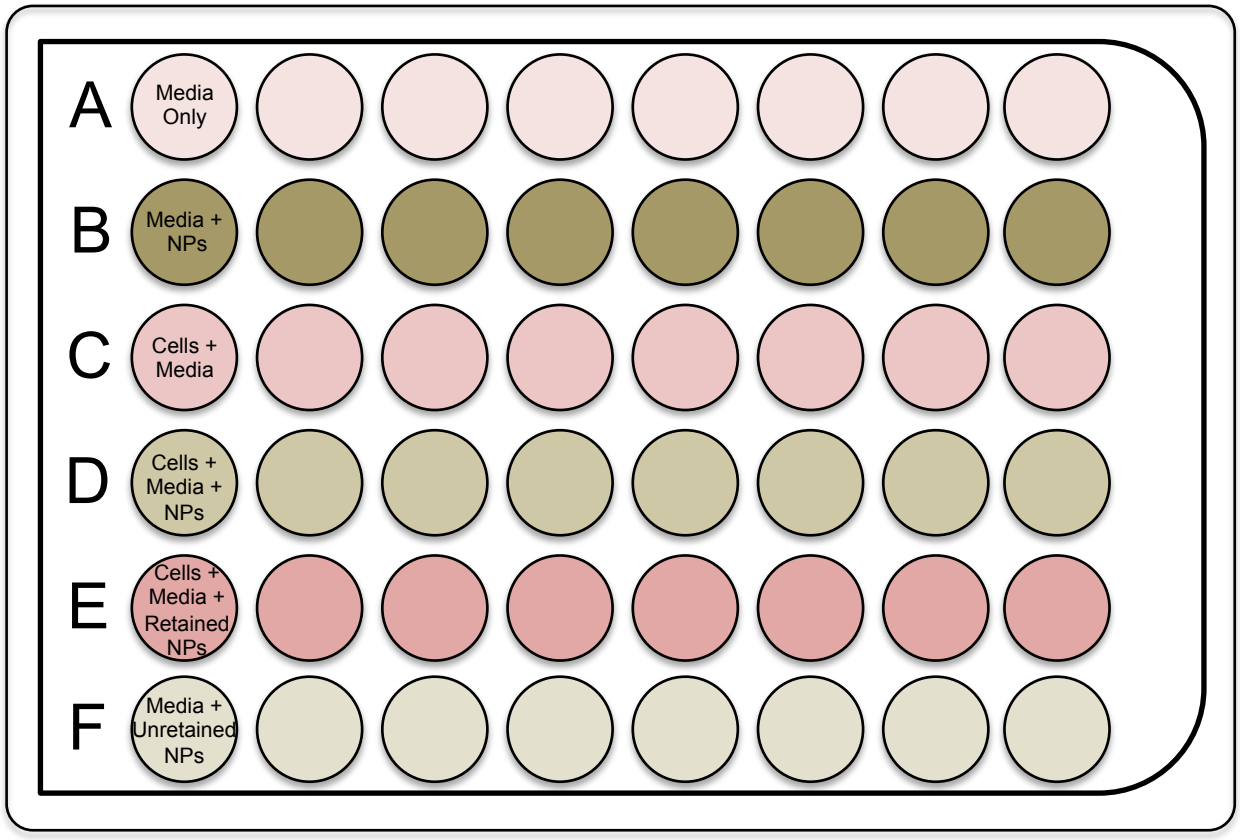

Fig. 12 Experimental setup for the Absorption assay.

This setup would determine any absorbance that comes from the nanoparticles, or media and cells, or any combination thereof that contributes to the normal MTT assay values. The nanoparticles that were taken up by the cells were defined as retained. Unretained nanoparticles were defined as ones that were not taken up by the cells and left in the media. The absorbance of the full concentration of nanoparticles was calculated as

row B (media and nanoparticles) – row A (media only). The absorbance due to the retained nanoparticles was calculated as row B (media and nanoparticles) – row F (media and unretained nanoparticles). The absorbance from the unretained nanoparticles was calculated as row F (media and unretained nanoparticles) - row A (media only).

Manipulation with the remaining rows yielded several values of absorbance for other combinations, some of which were negligible. Ratios of retained nanoparticles to total nanoparticles were calculated. Averaging these ratios allowed for an estimation of the percentage of nanoparticles taken up for a given concentration. The standard error that was calculated for each group is represented as the standard deviation divided by the square root of the sample size. These errors were added in quadrature. A typical layout for this type assay included 8 samples per nanoparticle concentration.

Chapter 3: Experimental Results

3.1 Survival Curve Results

Before treatment with nanoparticles began, cell survival curves were first determined. These curves provided the targeted LD50 value of proton irradiation used in experiments with the corresponding cell line. Data was plotted on a semi-logarithmic plot and fitted using the linear-quadratic model. This model is the accepted standard for plotting survival rates in radiobiology [106-108, 110, 111]. The survival fraction is calculated as,

$$S = e^{-(\alpha D + \beta D^2)} \tag{3.1}$$

where S represents the fraction of cells surviving, D represents the dose measured in Gy while α and β are constants. For low LET radiation, these type curves generally have two distinguishable segments, an initial linear portion that transitions into a subsequent quadratic portion producing a shoulder region that connects the two. For higher LET radiation such as proton radiation, the linear portion dominates and a straight fit is observed. Therefore, the survival curves performed in this study were properly straight since the quadratic portion of the fit was negligible in most cases. Previous research with protons of comparable LET show this similar straight fit characteristic using hamster cells [106]. Figure 13 shows the 184A1 breast epithelial cell survival curve produced using the MTT assay. Based on this curve, the LD50 was found to be 3.3 Gy. Figures 14 and 15 show the 22RV1 prostate carcinoma cell survival curves produced using the MTT and clonogenic assays respectively. The MTT curve predicts the LD50 value to be around 55 cGy, while the

colony curve estimates it to be about 75 cGy. The decision was made to expose this cell line at level higher than the LD50 mark so that any drop in survival due to sensitization from an experimental treatment would be most pronounced in a graphical representation. It was decided that 40 cGy would be adequate for exposure. Figures 16 and 17 show the MCF7 breast carcinoma cell survival curves produced using the MTT and clonogenic assays respectively. The MTT curve estimates the LD50 value to be 35 cGy and the colony curve shows a value closer to 55 cGy. Since these cells were so sensitive, a decision was made to expose them at a level slightly higher than the LD50 mark in order to increase the signal in our assays. It was decided that 30 cGy would be sufficient. Although these survival curves are not excessively compelling, they are sufficient in providing an estimated starting dose for the purposes of this study.

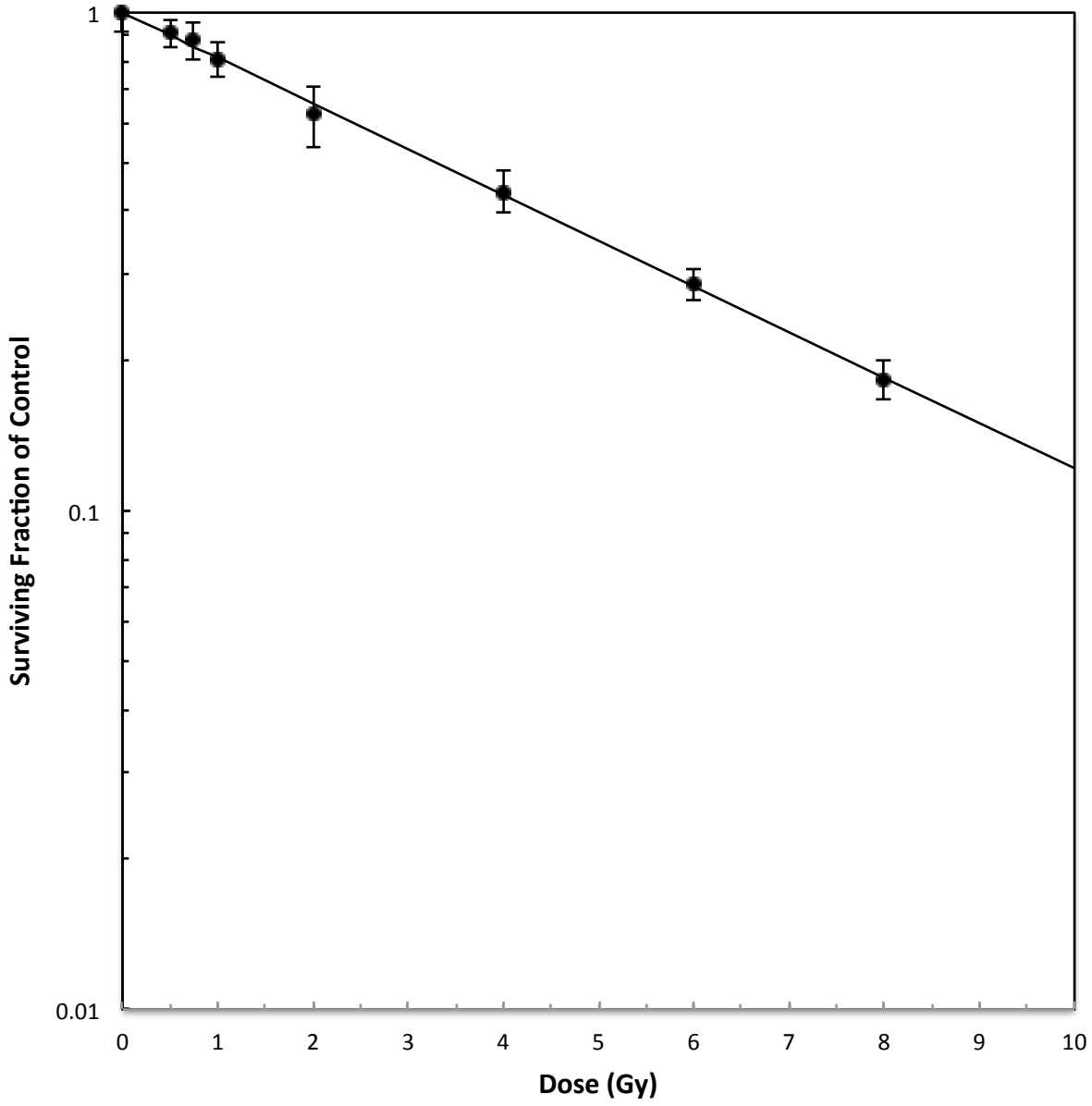

Fig. 13 Survival curve of the 184A1 breast epithelial cell line exposed to 2 MeV incident protons. This data was collected using the MTT assay and was plotted on a semi-log plot using the linear-quadratic model (mean ± standard error).

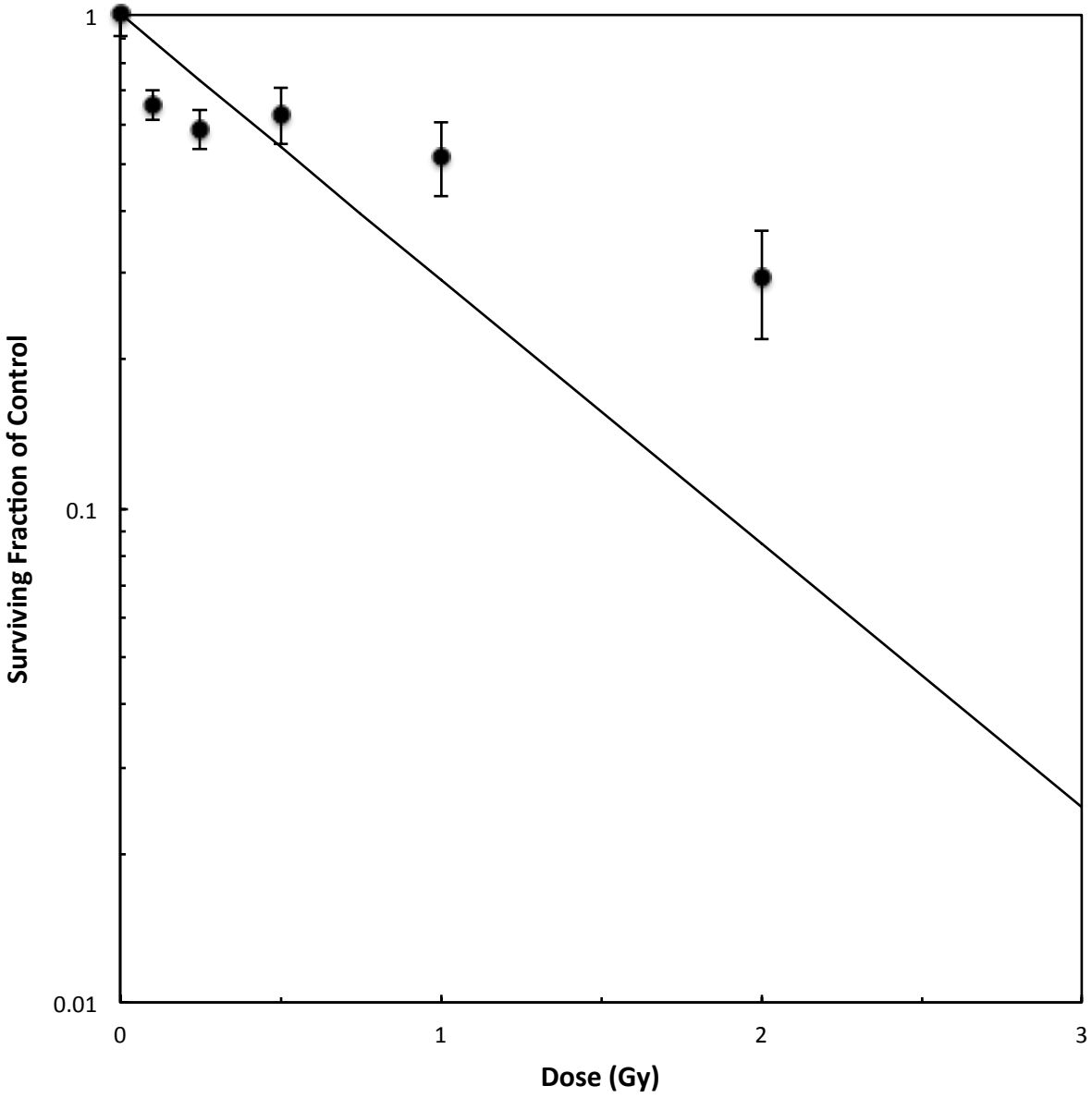

Fig. 14 Survival curve of the 22RV1 prostate carcinoma cell line exposed to 2 MeV incident protons. This data was collected using the MTT assay and was plotted on a semi-log plot using the linear-quadratic model (mean ± standard error).

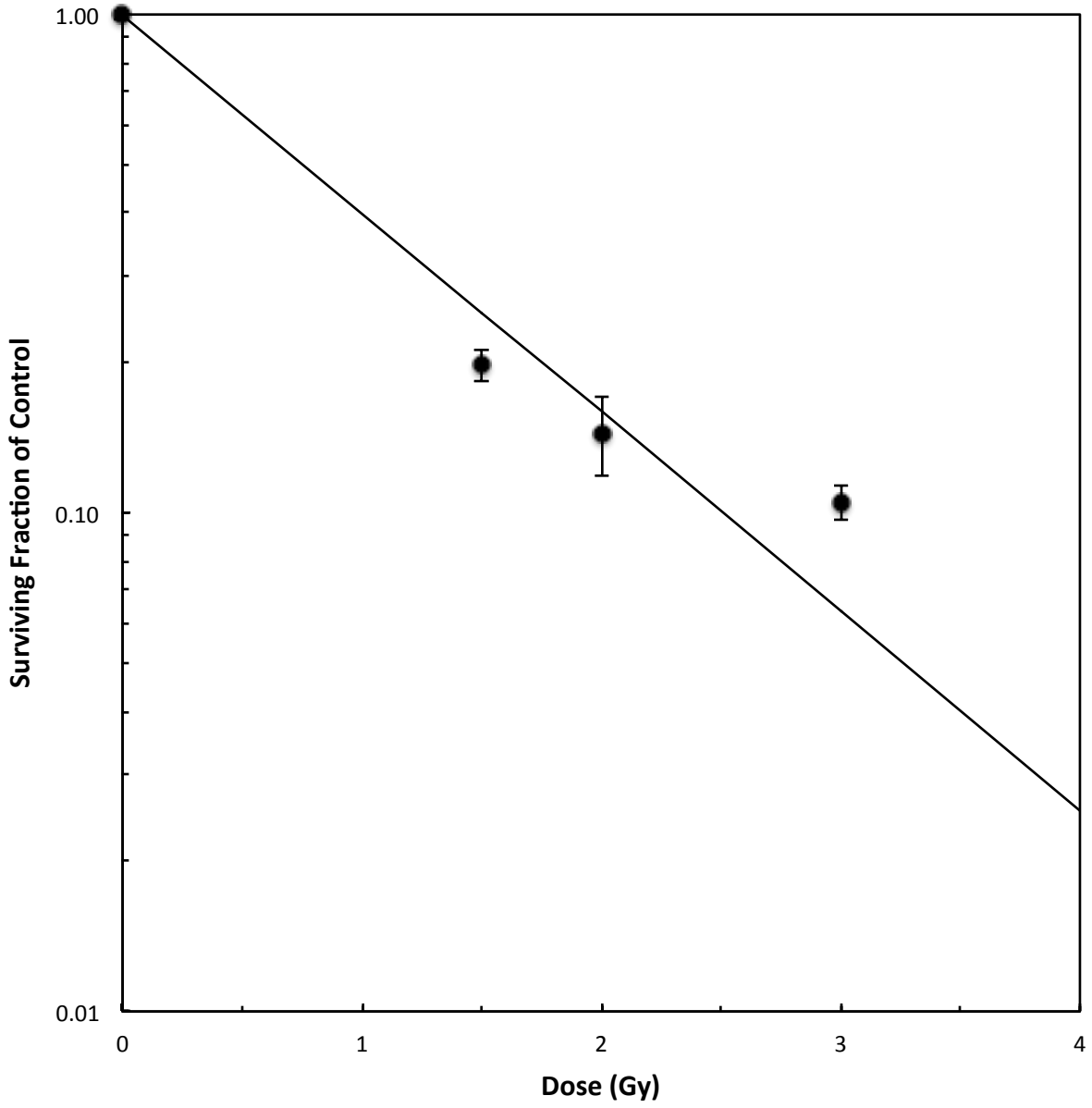

Fig. 15 Survival curve of the 22RV1 prostate carcinoma cell line exposed to 2 MeV incident protons. This data was collected using the clonogenic assay and was plotted on a semi-log plot using the linear-quadratic model (mean ± standard error).

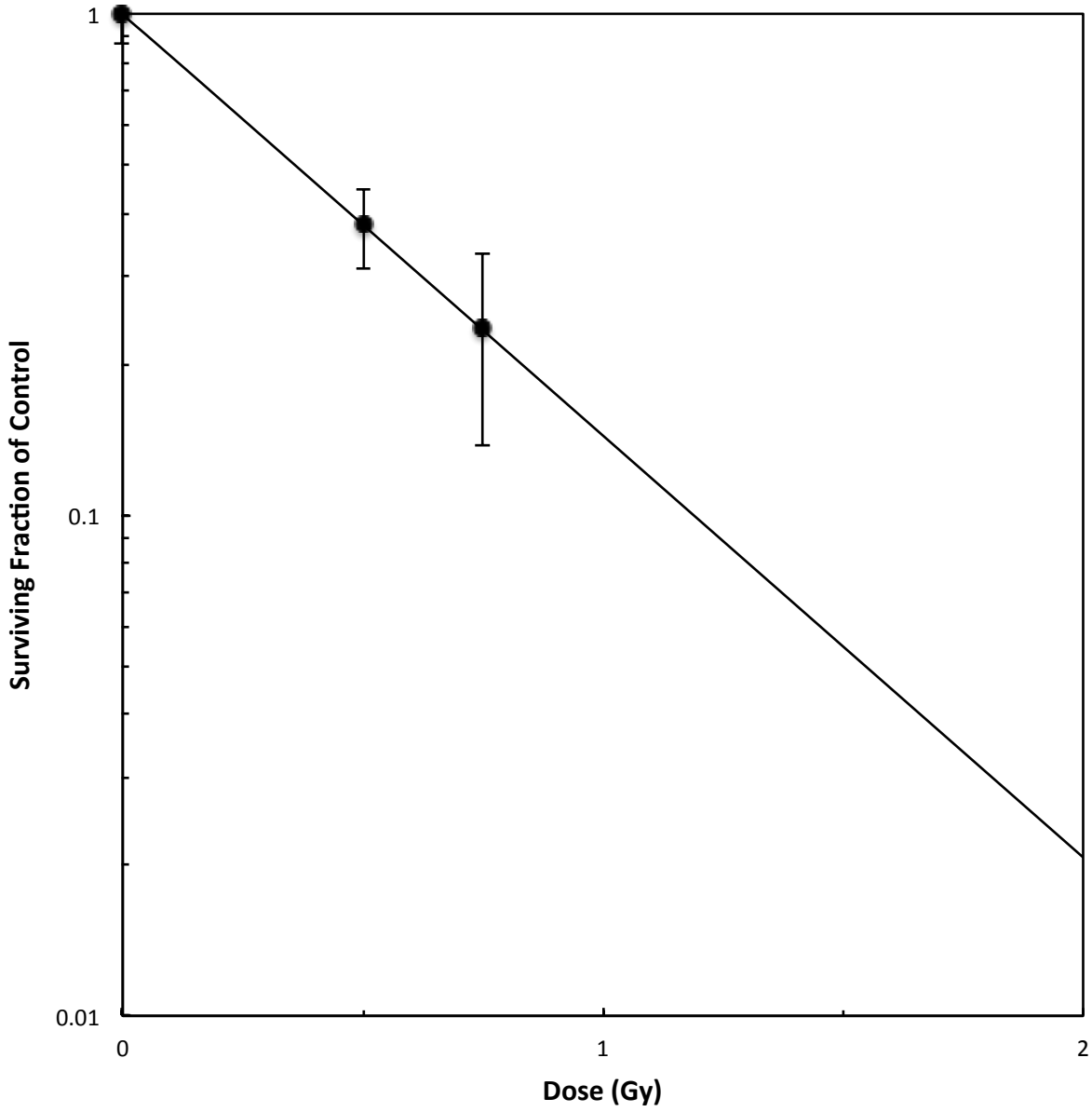

Fig. 16 Survival curve of the MCF7 breast carcinoma cell line exposed to 2 MeV incident protons. This data was collected using the MTT assay and was plotted on a semi-log plot using the linear-quadratic model (mean ± standard error).

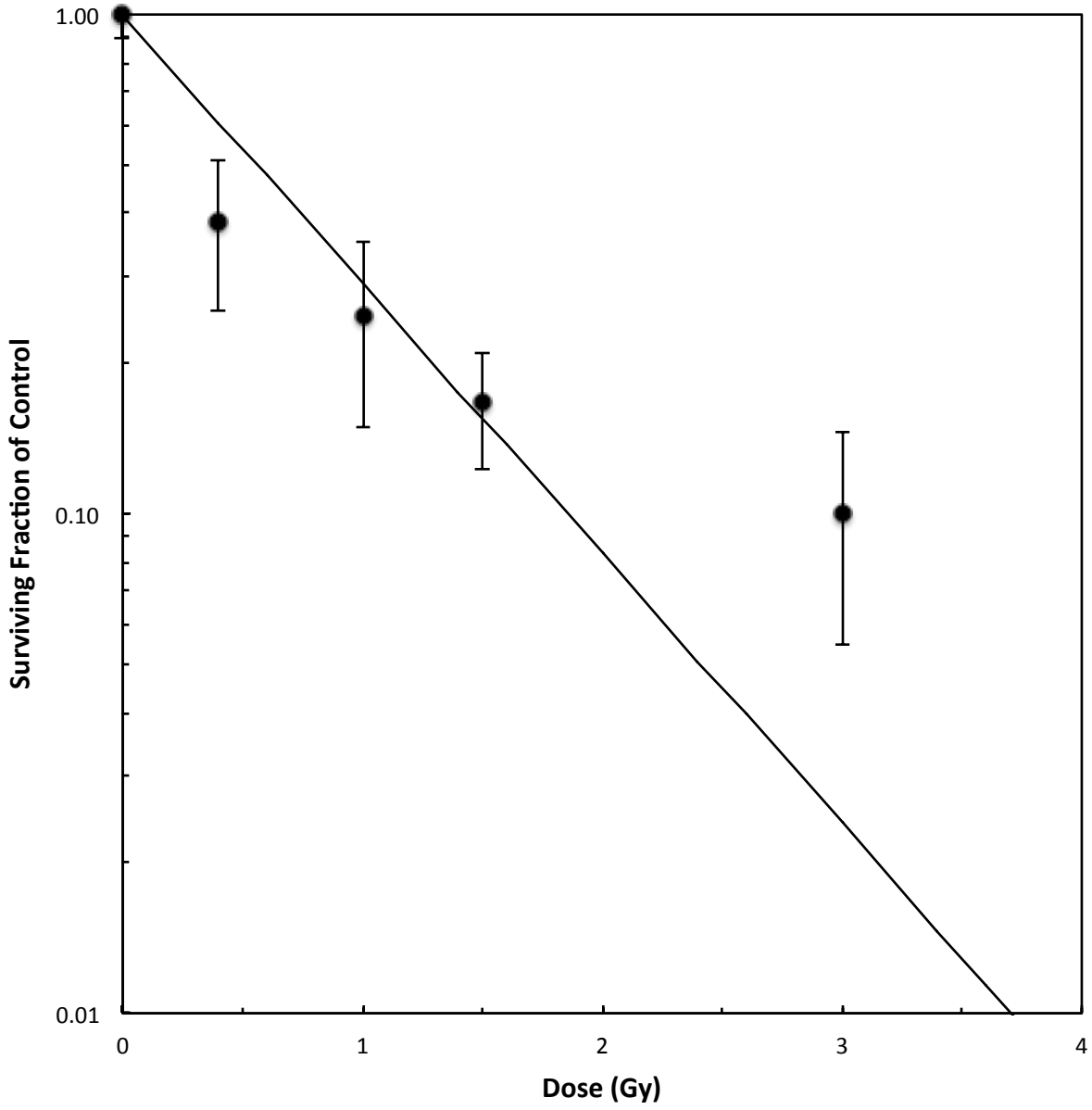

Fig. 17 Survival curve of the MCF7 breast carcinoma cell line exposed to 2 MeV incident protons. This data was collected using the clonogenic assay and was plotted on a semi-log plot using the linear-quadratic model (mean ± standard error).

3.2 CNP Results

Various types of CNPs were used throughout the course of this study. Some of them were investigated in a parallel study[112] and other parameters of CNP treatment were focused on in previous studies[113]. Two of the CNP types will be discussed in detail below. They are designated according to the label on their respective vials received from UCF. Every CNP type and concentration that was examined had a corresponding non-irradiated control that was used to observe chemical toxicity. A non-irradiated primary control as well as an irradiated control with no additives was included in each experiment to determine the radiation damage to untreated cells. These untreated controls are typically labeled as having "0 M" concentration of nanoparticles or as simply "No NP". Each set of data was analyzed two different ways for comparison. The first analysis compares all experimental groups as a surviving percent of the primary non-irradiated control. The data are shown this way to document potential toxic effects (chemical toxicity) of the nanoparticles. In the second analysis, the data points for each irradiated group are divided by their respective non-irradiated control to provide insight into any physical (radio-protective or enhancing) effects of the nanoparticles. Correct interpretation of any radio-effect of the nanoparticles requires subtraction of their inherent chemical effects.

184A1 Results

Fig. 18 shows the effects of CNP type NH4 screened in various concentrations against the 184A1 breast epithelial cell line. The MTT assay was employed to survey the different concentrations in order to expose any trends. The non-irradiated controls show evident signs of chemically toxic effects increasing with the NH4 concentration, and the

irradiated groups show some apparent sensitization effects at the higher concentrations. The toxicity is statistically significant even at the low concentration of 10 nm, and becomes highly significant at and above the 100 nm concentration. The net effect of the nanoparticles yielded a significant 26% drop and a highly significant 36% drop in the 100 nM and 1 μM groups respectively as compared to the irradiated 0 M group. Comparison of each irradiated sample with its non-irradiated control indicates that NH4 produces a slight physical protection with a 6% increase at the 10 nM concentration in spite of toxicity when compared to the untreated control group and increasing physical sensitization at the 100nM concentration with an 11% drop and the 1 μM concentration with a 26% drop. Only the 1 μM concentration is statistically significant.

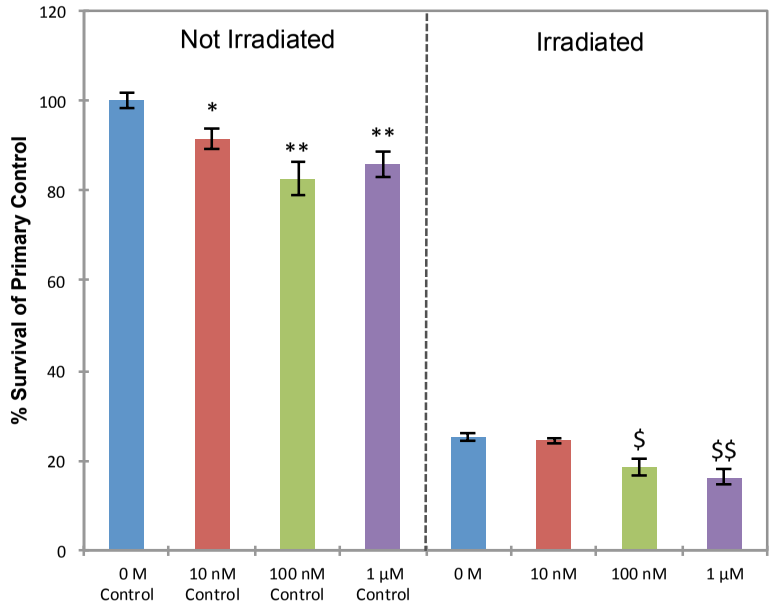

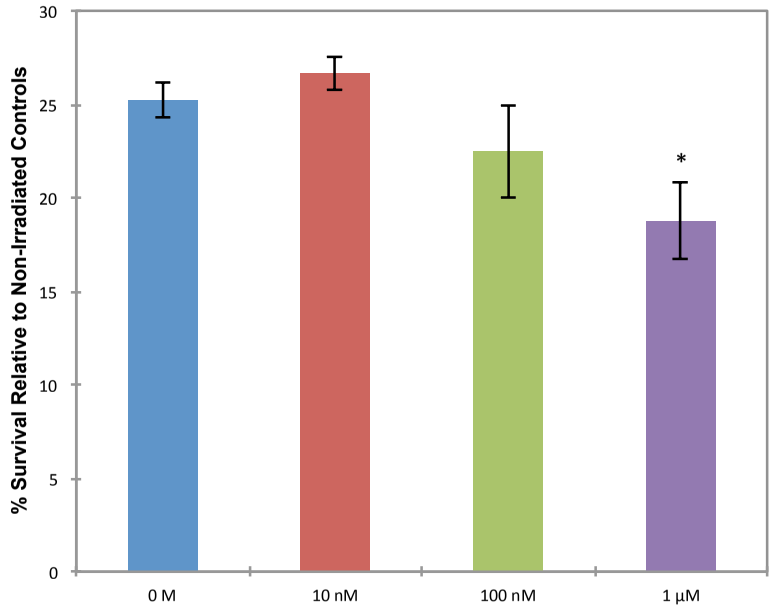

Toxicity	tstat	P-value	% Diff From Control
0 M Control			
10 nM Control	-3.058404	0.028153	-8.493413
100 nM Control	-4.335490	0.007461	-17.513102
1 µM Control	-4.307286	0.007662	-14.133171

Radio Effect	tstat	P-value	% Diff From Control
0 M			
10 nM	1.136275	0.307351	5.706871
100 nM	-1.028820	0.411716	-10.783012
1 µM	-2.888288	0.034255	-25.567840

Fig. 18 A survey of concentrations with NH4-type nanoparticles in 184A1 breast epithelial cells using the MTT assay. Cells were exposed to a 3.3 Gy equivalent single dose of proton radiation. Data are expressed as percentages of the primary control first to show chemical toxicity, and then irradiated groups are expressed as percentages of their corresponding non-irradiated controls to provide insight into any physical effects (mean ± standard error). Experimental groups are compared to untreated controls and statistical significance is determined by Student's t-test (*P<0.05, **P<0.01). The net effect yielded a significant 26% drop (labeled with $) and a highly significant 36% drop (labeled with $$) in the 100 nM and 1 µM groups respectively as compared to the irradiated 0 M group (P-values = 0.0259 and 0.0053).

Fig. 19 displays the CNP type NC investigated with various concentrations against the 184A1 breast epithelial cell line using the MTT assay. The NC-type nanoparticle shows no signs of chemical toxicity among the non-irradiated controls and possibly slight growth promotion at the highest concentration. The irradiated groups reveal a significant net effect is present at the 10 μM concentration producing a 32% overall increase for this cell line. Comparison of each irradiated sample with its non-irradiated control indicates that physical protection from the radiation is evident at the 10 μM concentration with an 18% increase when compared to the untreated control group, however this increase is not statistically significant. It appears that at high concentrations of NC the chemical effects start to interfere with any protective properties.

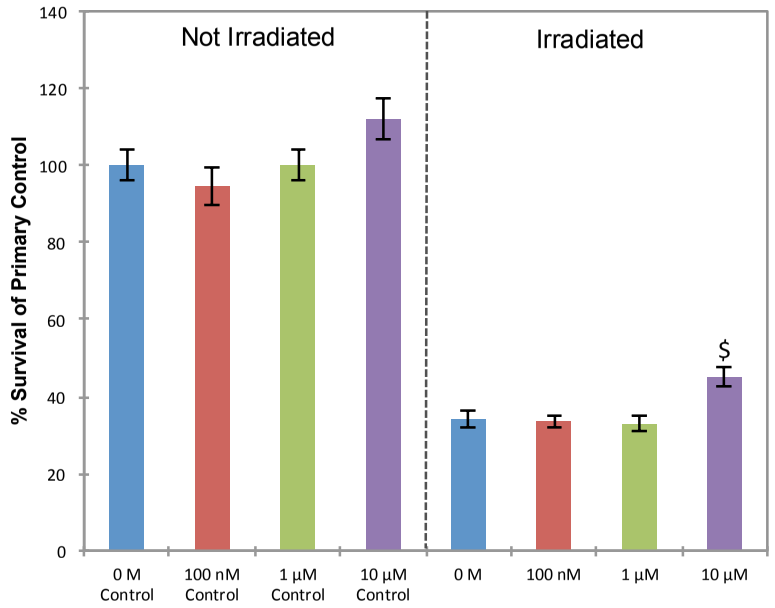

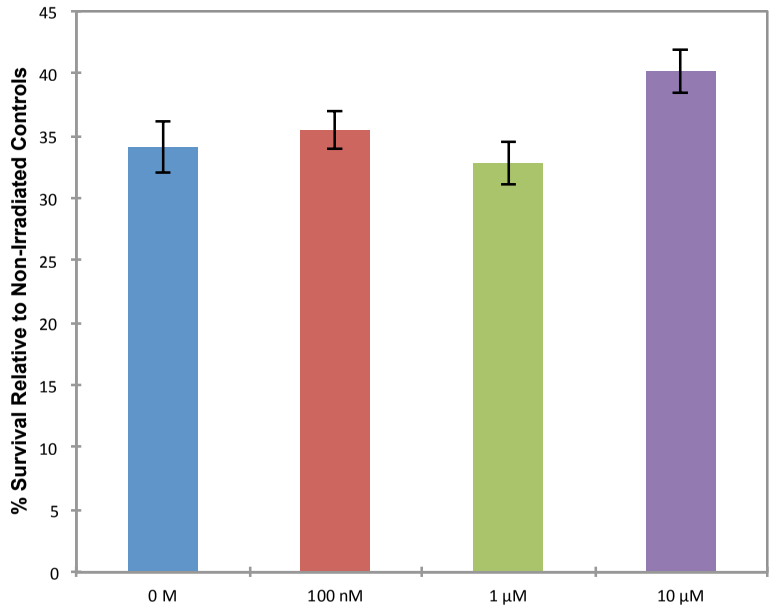

Toxicity	tstat	P-value	% Diff From Control
0 M Control			
100 nM Control	-0.825402	0.446722	-5.279905
1 µM Control	0.023832	0.981908	0.139865
10 µM Control	1.784394	0.134432	11.998671

Radio Effect	tstat	P-value	% Diff From Control
0 M			
100 nM	0.535201	0.615448	3.993584
1 µM	-0.459937	0.664869	-3.639136
10 µM	2.263069	0.073070	17.955662

Fig. 19 A survey of concentrations with NC-type nanoparticles in 184A1 breast epithelial cells using the MTT assay. Cells were exposed to a 3.3 Gy equivalent single dose of proton radiation. Data are expressed as percentages of the primary control first to show chemical toxicity, and then irradiated groups are expressed as percentages of their corresponding non-irradiated controls to provide insight into any physical effects (mean ± standard error). Experimental groups are compared to untreated controls and statistical significance is determined by Student's t-test (*P<0.05, **P<0.01). The net effect at the 10 µM level (labeled with $) had a statistically significant 32% increase as compared to the irradiated 0 M group (P-value = 0.0175).

An experiment was performed in which the nanoparticles were added after irradiation in order to see if the CNPs exhibited any radiomitigating properties as well. In this experiment, 184 breast epithelial cells were exposed to a 3.3 Gy equivalent single dose of proton radiation, NC and NH4 were added post-irradiation in 10 μM concentrations, and the result was evaluated with the MTT assay shown in Fig. 20. The results show no significant chemical effect for NC but highly significant toxicity for NH4 in the non-irradiated controls and the irradiated groups reveal no discerning effects. However, comparison of each irradiated sample with its non-irradiated control indicates that NH4 produced a higher percent of survival in spite of its own toxicity, yielding a statistically significance increase of 25% as compared to the untreated control group. NC had a slight increase, but ultimately yielded no significant effect.

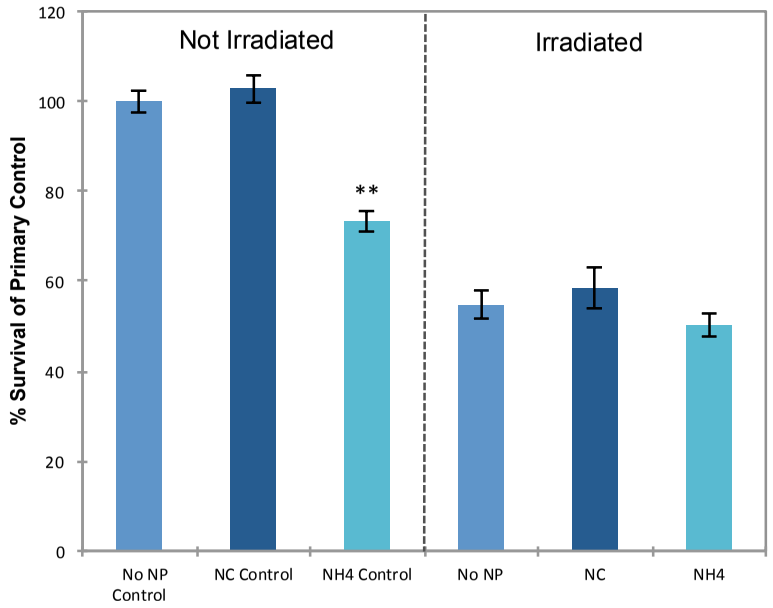

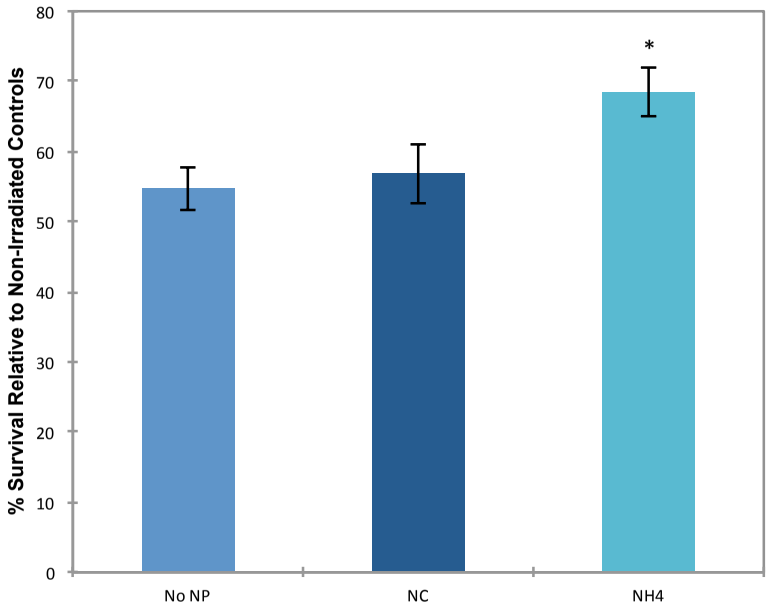

Toxicity	tstat	P-value	% Diff From Control
No NP Control			
NC Control	0.705790	0.503124	2.839992
NH4 Control	-7.861662	0.000102	-26.762300

Radio Effect	tstat	P-value	% Diff From Control
No NP			
NC	0.408671	0.694994	3.930529
NH4	2.993240	0.020134	25.184726

Fig. 20 A post-irradiation study in which 184A1 breast epithelial cells were exposed to a 3.3 Gy equivalent single dose of proton radiation and then NC-type and NH4-type nanoparticles were added to the cells in 10 μM concentrations. These results were collected using the MTT assay. Data are expressed as percentages of the primary control first to show chemical toxicity, and then irradiated groups are expressed as percentages of their corresponding non-irradiated controls to provide insight into any physical effects (mean ± standard error). Experimental groups are compared to untreated controls and statistical significance is determined by Student's t-test (*P<0.05, **P<0.01).

22RV1 Results

The results for a preliminary study performed with the 22RV1 prostate carcinoma cell line are shown in Fig. 21. In this experiment, cells were treated with NC and NH4 nanoparticles at 1 μM concentrations, exposed to a 1 Gy equivalent single dose of proton radiation, and evaluated using the MTT assay. The non-irradiated controls show no significant chemical effects, while the irradiated groups appear to be showing some sensitization properties. Although comparison of each irradiated sample with its non-irradiated control indicates that both NC and NH4 treated cells show slight physical sensitization to the radiation with a 35% and 23% decrease respectively when compared to the untreated control group, it is not enough to be statistically significant.

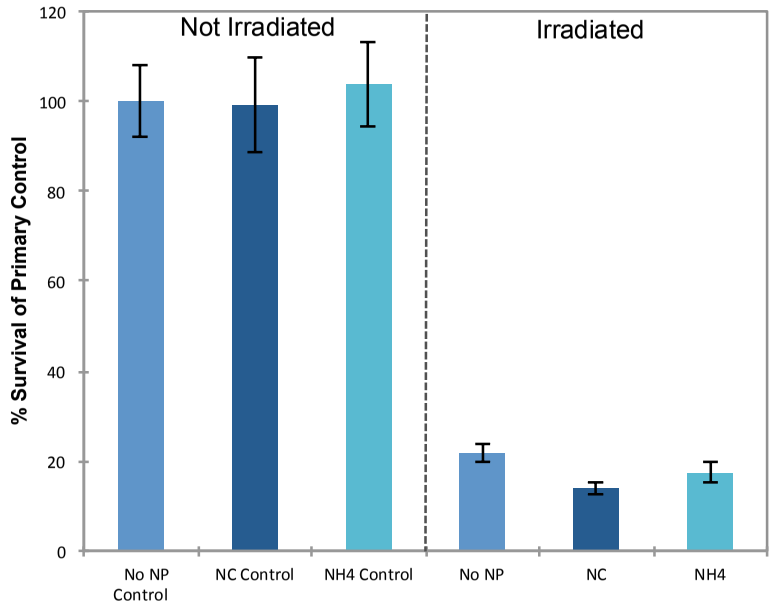

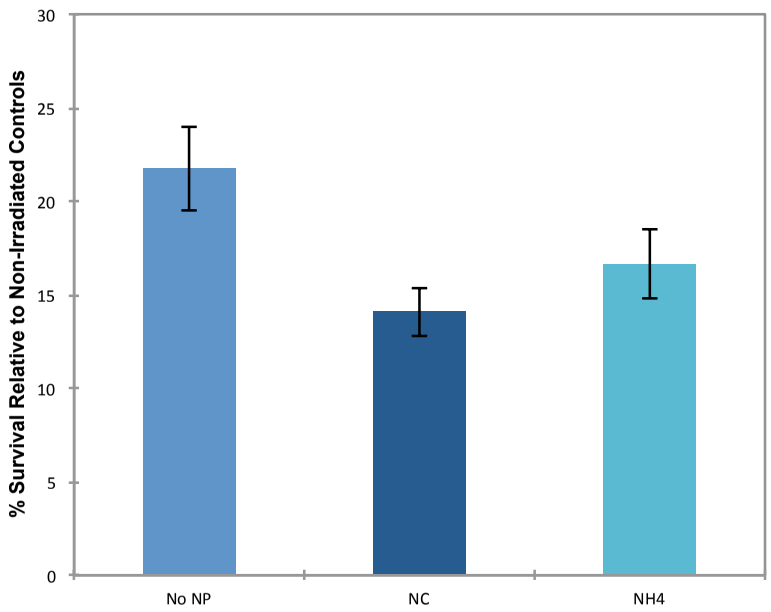

Toxicity	tstat	P-value	% Diff From Control
No NP Control			
NC Control	-0.060269	0.957422	-0.799802
NH4 Control	0.309493	0.786215	3.825858

Radio Effect	tstat	P-value	% Diff From Control
No NP			
NC	-2.939996	0.060510	-35.187797
NH4	-1.753808	0.177741	-23.487093

Fig. 21 A Preliminary study of NC-type and NH4-type nanoparticles in 22RV1 prostate carcinoma cells. Cells were treated nanoparticles at a 1 μM concentration, exposed to 1 Gy equivalent single dose of proton radiation, and the results were determined with MTT assay. Data are expressed as percentages of the primary control first to show chemical toxicity, and then irradiated groups are expressed as percentages of their corresponding non-irradiated controls to provide insight into any physical effects (mean ± standard error). Experimental groups are compared to untreated controls and statistical significance is determined by Student's t-test (*P<0.05, **P<0.01).

Fig. 22 shows the effects of the CNP type NH4 screened in various concentrations with the 22RV1 prostate carcinoma cell line. Effects were evaluated using the MTT assay in order to expose any trends. The non-irradiated controls show obvious chemical toxicity that increases with increasing NH4 concentration. For the irradiated groups, every concentration appears to be showing some degree of sensitizing properties. At the 1 μM level, the net effect produced a highly statistically significant decrease of 39% as compared to the irradiated control group. Upon closer inspection however, comparison of each irradiated sample with its non-irradiated control demonstrates that because of the high chemical toxicity, only the 10 nM concentration presents a physically sensitizing effect to the radiation with a slight 15% decrease as compared to the untreated control group, however it is not enough to be significant. In fact, the higher concentrations present some physical protection from the radiation in spite of their chemical toxicity, the greatest being the 10 μM group with a highly significant 75% increase when compared to the untreated control group. It is believed that in this cell line NH4 provides a chemically toxic effect that is somewhat linear and a small non-linear physical sensitization effect. As the concentrations increase, this small sensitizing effect is outweighed by the toxicity and gives way to more protective properties.

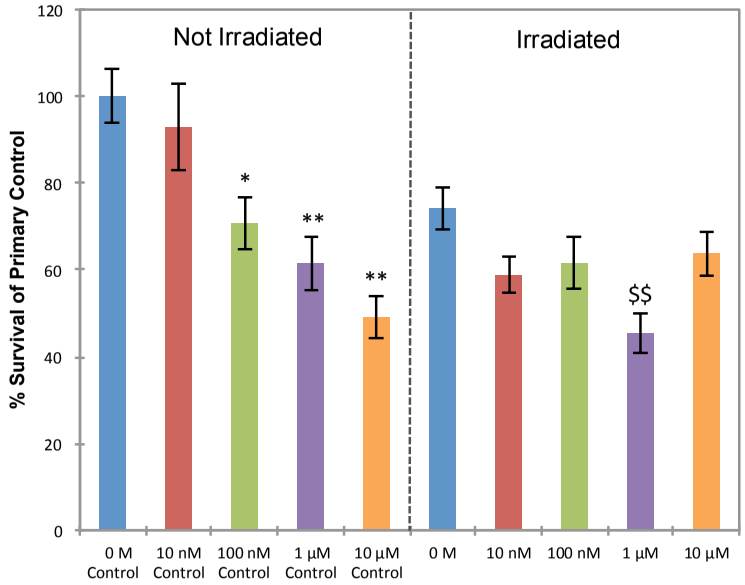

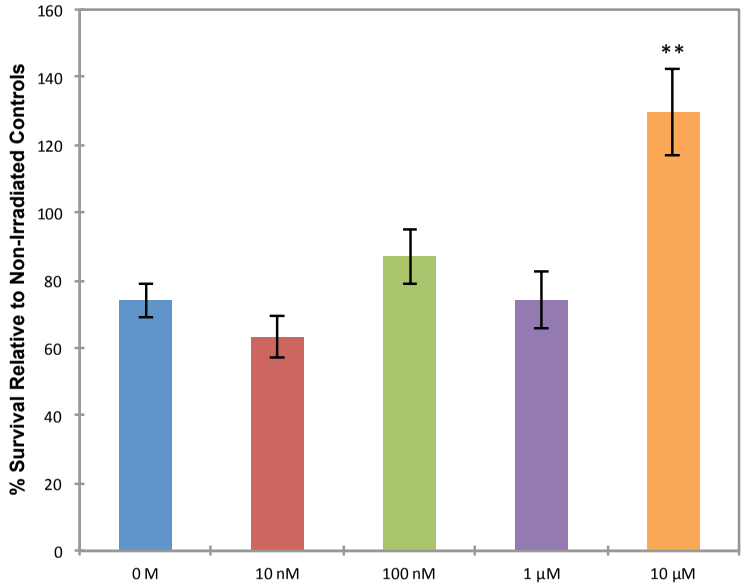

Toxicity	tstat	P-value	% Diff From Control
0 M Control			
10 nM Control	-0.596913	0.576565	-7.054163
100 nM Control	-3.443706	0.018362	-29.298723
1 µM Control	-4.479922	0.006519	-38.582072
10 µM Control	-6.411452	0.001369	-50.857379

Radio Effect	tstat	P-value	% Diff From Control
0 M			
10 nM	-1.377738	0.226755	-14.632465
100 nM	1.336697	0.238916	17.464191
1 µM	-0.004610	0.996500	-0.060637
10 µM	4.056998	0.009758	75.085291

Fig. 22 A survey of concentrations with NH4-type nanoparticles in 22RV1 prostate carcinoma cells using the MTT assay. Cells were exposed to a 40 cGy equivalent single dose of proton radiation. Data are expressed as percentages of the primary control first to show chemical toxicity, and then irradiated groups are expressed as percentages of their corresponding non-irradiated controls to provide insight into any physical effects (mean ± standard error). Experimental groups are compared to untreated controls and statistical significance is determined by Student's t-test (*P<0.05, **P<0.01). The net effect at the 1 µM level (labeled with $$) had a highly statistically significant 39% decrease as compared to the irradiated 0 M group (P-value = 0.0085).

Fig. 23 displays the results for the CNP type NC investigated with various concentrations against the 22RV1 prostate carcinoma cell line using the MTT assay. The NC-type nanoparticle shows obvious toxicity in the non-irradiated controls, increasing with concentration, while the irradiated groups exhibit some apparent protective properties. The toxicity is statistically significant at the 100 nM and 10 μM concentrations. Comparison of each irradiated sample with its non-irradiated control shows no physical sensitization whatsoever for NC, but rather physical protection from the radiation that increases with concentration yielding a 52%, 80%, and 108% increase for the 100 nM, 1 μM, and 10 μM concentrations respectively as compared to the untreated control group. Only the 100 nM and 1 μM concentrations are statistically significant however. It is believed that in this cell line NC provides a protective effect with increasing concentration, while at the same time presents a chemically toxic effect, and as the concentration increases, the toxic effects start to overwhelm the protective properties.

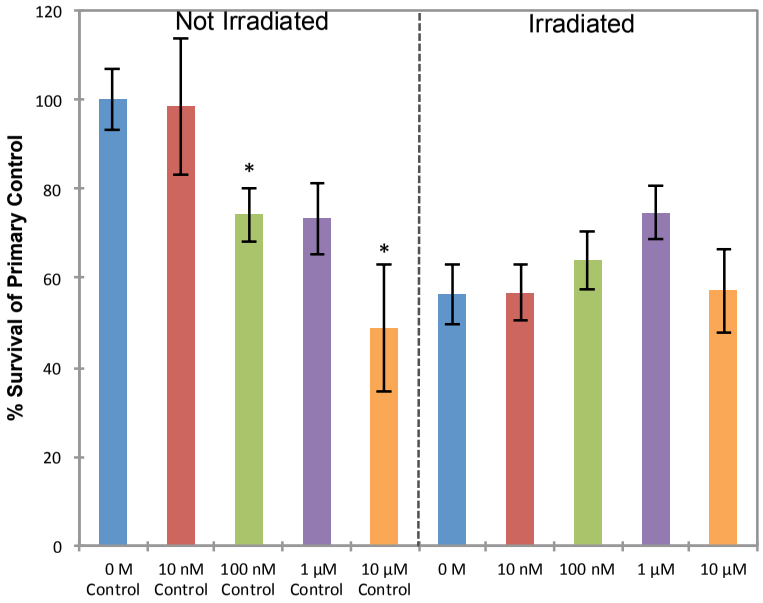

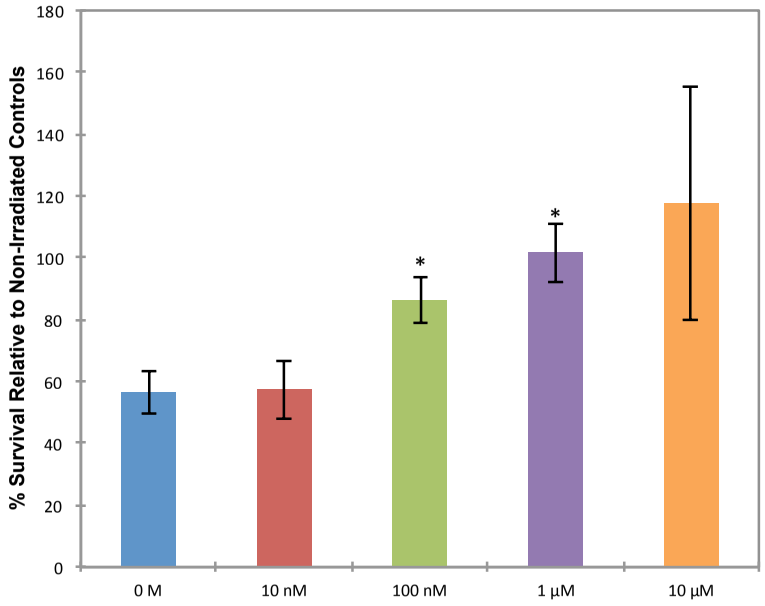

Toxicity	tstat	P-value	% Diff From Control
0 M Control			
10 nM Control	-0.086910	0.934116	-1.463622
100 nM Control	-2.794731	0.038231	-25.780396
1 µM Control	-2.509815	0.053840	-26.654925
10 µM Control	-3.250982	0.022671	-51.299648

Radio Effect	tstat	P-value	% Diff From Control
0 M			
10 nM	0.089928	0.931835	1.846209
100 nM	3.003865	0.029966	52.765809
1 µM	3.895183	0.011465	80.427763
10 µM	1.601526	0.170160	108.545374

Fig. 23 A survey of concentrations with NC-type nanoparticles in 22RV1 prostate carcinoma cells using the MTT assay. Cells were exposed to a 40 cGy equivalent single dose of proton radiation. Data are expressed as percentages of the primary control first to show chemical toxicity, and then irradiated groups are expressed as percentages of their corresponding non-irradiated controls to provide insight into any physical effects (mean ± standard error). Experimental groups are compared to untreated controls and statistical significance is determined by Student's t-test (*P<0.05, **P<0.01).

Fig. 24 displays the data for NC at the 1 μM concentration and NH4 at the 10 nM concentration in the 22RV1 prostate carcinoma cell line evaluated with the clonogenic assay. The results show no significant chemical effects in the non-irradiated controls after two weeks of growth with both nanoparticle types, and no evidence of sensitization or protection in the irradiated groups either. Based on the clonogenic assay, there was no visible effect with these type nanoparticles and their chosen concentrations in the 22RV1 cell line, which conflicts with the results collected from the MTT assay.

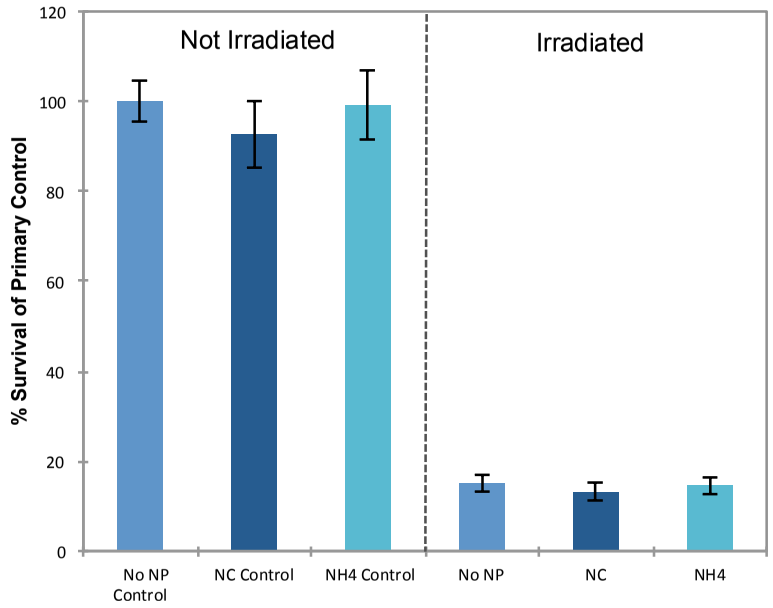

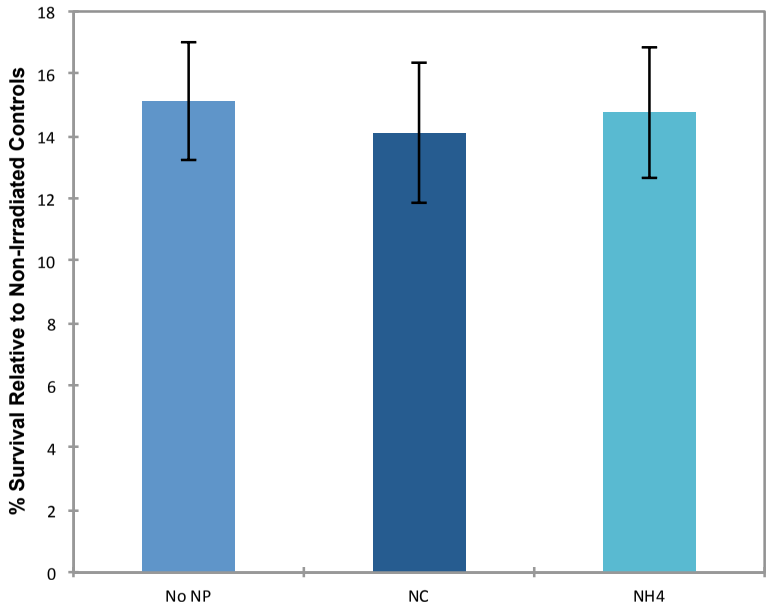

Toxicity	tstat	P-value	% Diff From Control
No NP Control			
NC Control	-0.814764	0.432494	-7.244094
NH4 Control	-0.085056	0.933745	-0.787402

Radio Effect	tstat	P-value	% Diff From Control
No NP			
NC	-0.350606	0.732506	-6.789403
NH4	-0.125707	0.902232	-2.356151

Fig. 24 1 µM of NC-type nanoparticles and 10 nM of NH4-type nanoparticles evaluated in 22RV1 prostate carcinoma cells using the clonogenic assay. Cells were exposed to a 40 cGy equivalent single dose of proton radiation. Data are expressed as percentages of the primary control first to show chemical toxicity, and then irradiated groups are expressed as percentages of their corresponding non-irradiated controls to provide insight into any physical effects (mean ± standard error). Experimental groups are compared to untreated controls and statistical significance is determined by Student's t-test (*P<0.05, **P<0.01).

MCF7 Results

Fig. 25 shows the CNP type NH4 screened in various concentrations with the MCF7 breast carcinoma cell line. The MTT assay was used to survey the different concentrations in order to expose any trends. The non-irradiated controls show clear chemical toxicity that increases quite linearly with increasing NH4 concentration. The toxicity becomes highly significant at and above the 1 μM concentration. For the irradiated groups, a net effect at the 10 μM level produced a statistically significant decrease of 42% as compared to the irradiated 0 M group. Comparison of each irradiated sample with its non-irradiated control indicates some physical sensitization to the radiation at the 100 nM and 10 μM concentrations. These concentrations show an 18% and 19% drop respectively when compared to the untreated control group, however this drop is not statistically significant.

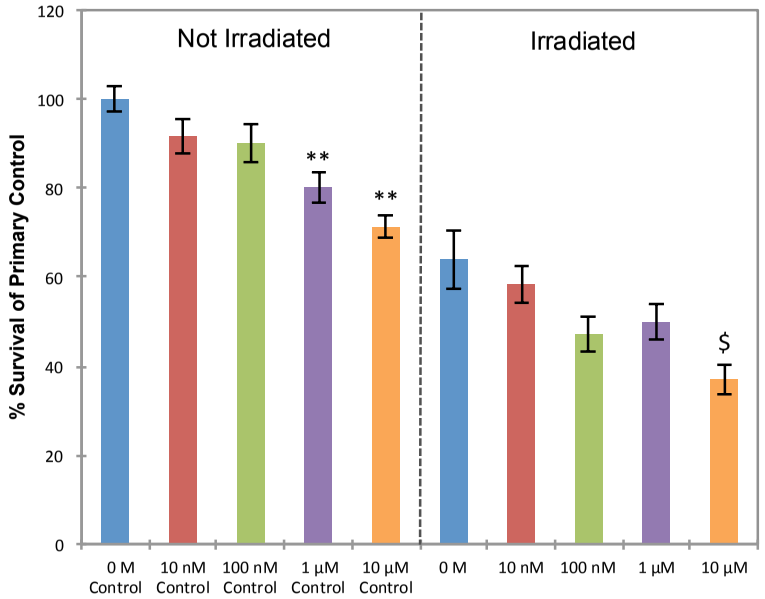

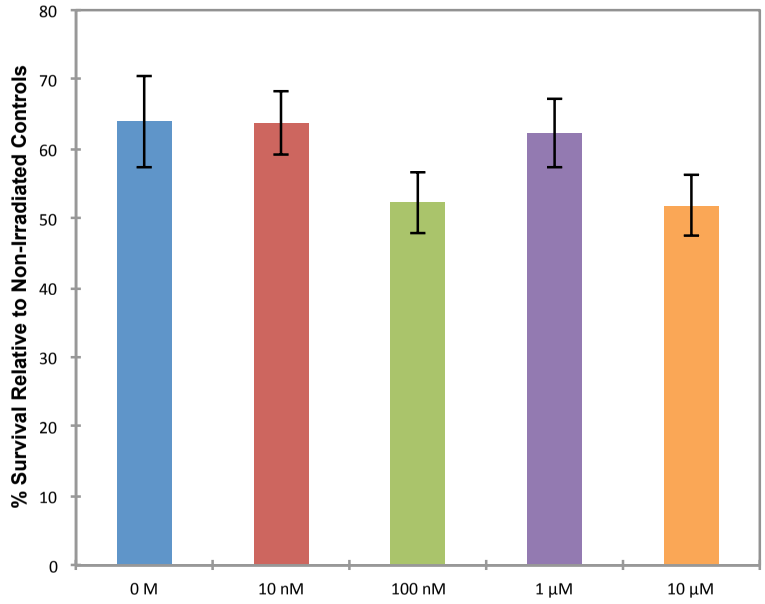

Toxicity	tstat	P-value	% Diff From Control
0 M Control			
10 nM Control	-1.705780	0.148764	-8.323946
100 nM Control	-1.862415	0.121593	-9.920188
1 µM Control	-4.383965	0.007128	-19.941040
10 µM Control	-7.561250	0.000642	-28.753925

Radio Effect	tstat	P-value	% Diff From Control
0 M			
10 nM	-0.031691	0.975945	-0.399771
100 nM	-1.460285	0.204041	-18.262476
1 µM	-0.201459	0.848279	-2.632069
10 µM	-1.528702	0.186882	-19.000422

Fig. 25 A concentration survey of NH4-type nanoparticles in MCF7 breast carcinoma cells using the MTT assay. Cells were exposed to a 30 cGy equivalent single dose of proton radiation. Data are expressed as percentages of the primary control first to show chemical toxicity, and then irradiated groups are expressed as percentages of their corresponding non-irradiated controls to provide insight into any physical effects (mean ± standard error). Experimental groups are compared to untreated controls and statistical significance is determined by Student's t-test (*P<0.05, **P<0.01). The net effect at the 10 µM level (labeled with $) had a statistically significant 42% decrease as compared to the irradiated 0 M group (P-value = 0.0146).

Fig. 26 displays the CNP type NC investigated with various concentrations with the MCF7 breast carcinoma cell line using the MTT assay. The NC-type nanoparticles show clear toxicity in the non-irradiated controls that appears to increase quite linearly with concentration. The toxicity is significant even at the low concentration of 10 nM and it becomes highly significant at and above the 100 nM concentration. For the irradiated groups, the net effect produced a highly significant 38% drop, a significant 25% drop, and a highly significant 31% drop in the 100 nM, 1 μM, and 10 μM groups respectively as compared to the irradiated 0 M group. Comparison of each irradiated sample with its non-irradiated control implies there is significant physical sensitization to the radiation at the 100 nM concentration yielding a 27% decrease as compared to the untreated group. The higher concentrations show an upward trend in spite of their increasing toxicity, which suggests a protective attribute may be present at those concentrations as well.

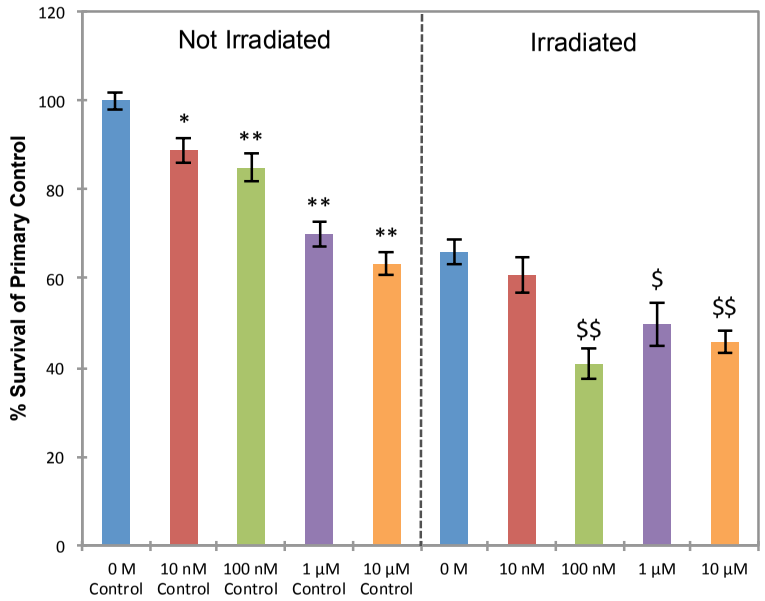

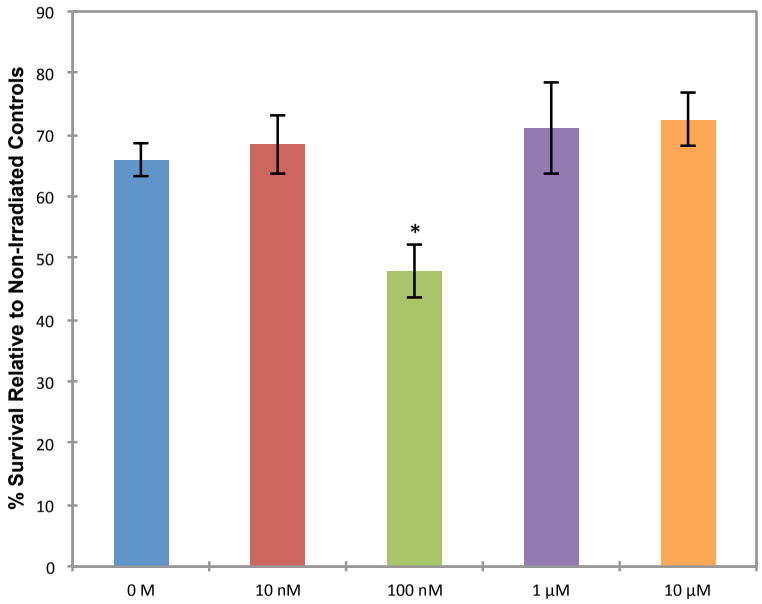

Toxicity	tstat	P-value	% Diff From Control
0 M Control			
10 nM Control	-3.174233	0.024697	-11.146364
100 nM Control	-4.058390	0.009745	-15.133181
1 µM Control	-8.586194	0.000353	-29.990900
10 µM Control	-11.609901	0.000083	-36.779065

Radio Effect	tstat	P-value	% Diff From Control
0 M			
10 nM	0.448175	0.672780	3.756937
100 nM	-3.507016	0.017155	-27.270198
1 µM	0.645968	0.546773	7.754761
10 µM	1.248841	0.267006	9.834562

Fig. 26 A survey of concentrations with NC-type nanoparticles in MCF7 breast carcinoma cells using the MTT assay. Cells were exposed to a 30 cGy equivalent single dose of proton radiation. Data are expressed as percentages of the primary control first to show chemical toxicity, and then irradiated groups are expressed as percentages of their corresponding non-irradiated controls to provide insight into any physical effects (mean ± standard error). Experimental groups are compared to untreated controls and statistical significance is determined by Student's t-test (*P<0.05, **P<0.01). The net effect produced a highly significant 38% drop ($$), a significant 25% drop ($), and a highly significant 31% drop ($$) in the 100 nM, 1 µM, and 10 µM groups respectively as compared to the irradiated 0 M group (P-values = 0.0025, 0.0364, 0.0030).

Fig. 27 shows both NC and NH4 at the 100 nM concentration in the MCF7 breast carcinoma cell line using the clonogenic assay. After two weeks of growth, the results show the expected chemical toxicity in the non-irradiated NC group and an unexpected chemical growth promotion effect in the non-irradiated NH4 group, while both irradiated groups appear to show some overall sensitization. The net effect for the NC group had a 23% decrease and the net effect for the NH4 group had a 42% decrease as compared to the irradiated No NP group. Upon closer inspection, comparison of each irradiated sample with its non-irradiated control shows that once the chemical effects are factored out, only NH4 had a physically sensitizing effect to the radiation, resulting in a highly significant drop of 54% as compared to the untreated group.

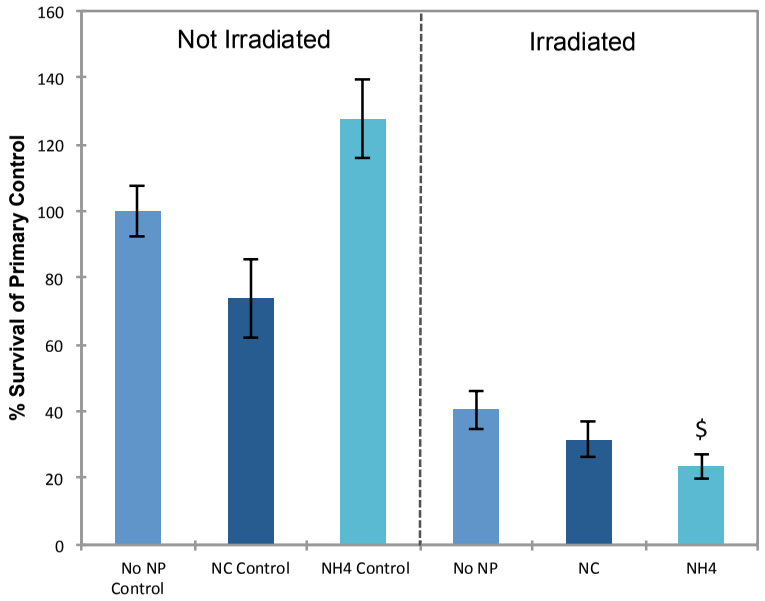

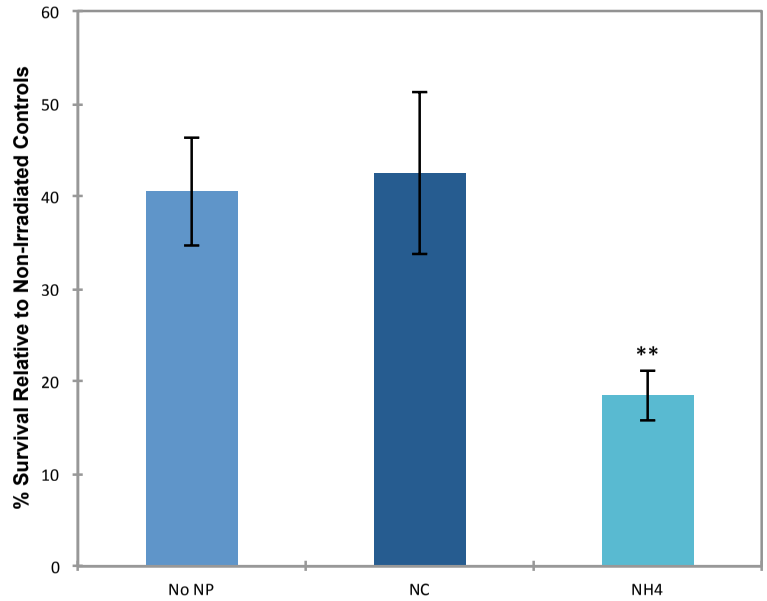

Toxicity	tstat	P-value	% Diff From Control
No NP Control			
NC Control	-1.873506	0.087793	-26.143791
NH4 Control	1.959624	0.075863	27.450980

Radio Effect	tstat	P-value	% Diff From Control
No NP			
NC	0.185844	0.855950	4.824436
NH4	-3.418127	0.005742	-54.441687

Fig. 27 NC-type and NH4-type nanoparticles in MCF7 breast carcinoma cells at 100 nM concentrations. Cells were exposed to a 30 cGy equivalent single dose of proton radiation and results were determined using the clonogenic assay. Data are expressed as percentages of the primary control first to show chemical toxicity, and then irradiated groups are expressed as percentages of their corresponding non-irradiated controls to provide insight into any physical effects (mean ± standard error). Experimental groups are compared to untreated controls and statistical significance is determined by Student's t-test (*P<0.05, **P<0.01). The net effect for the NH4 group (labeled with $) had a statistically significant 42% decrease as compared to the irradiated No NP group (P-value = 0.0318).

3.3 Gold Nanoparticle Uptake Results

The results from an assay designed to look at uptake of nanoparticles, and outlined in the methods section above, are shown in Figure 28 below. CNPs do not have any measurable absorbance in the visible region, so gold nanoparticles, which absorb at 570 nm, were used as a proxy to give a rough estimate of particle uptake. GNPs of various concentrations were used with the 22RV1 prostate carcinoma cell line and evaluated for their uptake into the cells. The values displayed in Figure 28 below represent a ratio of the retained nanoparticles within the cell to the total nanoparticles that were added to the culture media as a way to demonstrate how much of the GNPs are taken up by the cells. For the 100 nM, 1 μM, and 10 μM concentrations, 34%, 52%, and 82% of the GNPs initially added were found to be retained in the cells respectively. Using a projected fit, the 10 nM concentration was extrapolated to be around 8%. Making the broad assumption that the rates of uptake between the two different types of particles are roughly the same, this simple assay may provide information on the uptake of the CNPs.

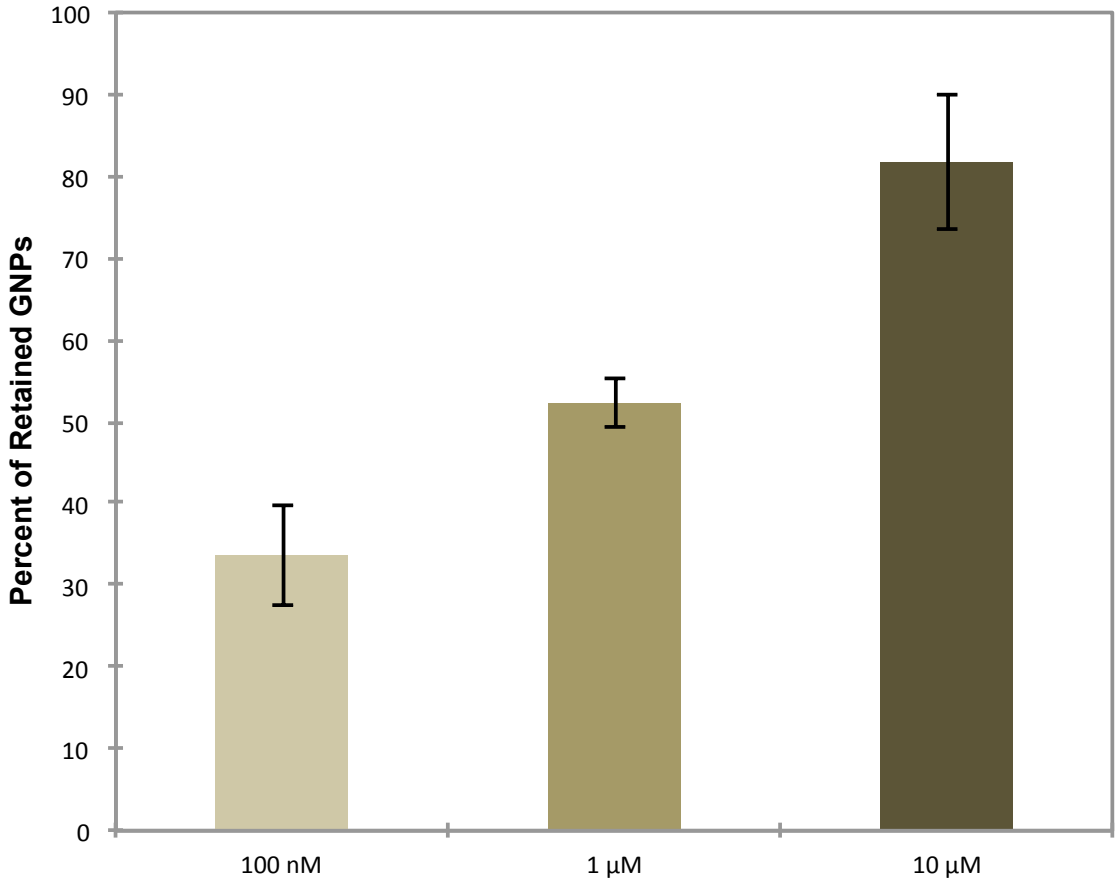

Fig. 28 Gold nanoparticles (GNPs) added to the 22RV1 prostate carcinoma cell line are assessed for their retention in the cells using an absorption assay. Data are expressed as percentages of the initial nanoparticle treatment added to cells (mean ± standard error).

Using the calculated absorbance value for the retained GNPs found in the absorption assay, a previous data set was corrected by subtracting this from the original values to obtain a more accurate representation of metabolically-determined cell viability. In this experiment, GNPs were added to the 184A1 breast epithelial cell line in 10 μM concentrations and then the cells were exposed to a 2 Gy equivalent single dose of proton radiation and assessed using the MTT assay. The results are shown in Figure 29 below. The results present a chemical growth promotion effect in the non-irradiated gold (Au) control with no apparent effect in the irradiated group. However, this growth promotion effect is not statistically significant. Comparison of each irradiated sample with its non-irradiated control indicates that there was enough physical sensitization to the radiation in spite of the growth promotion to yield an apparent 29% decrease when compared with the untreated control group; however, this decrease was not statistically significant.

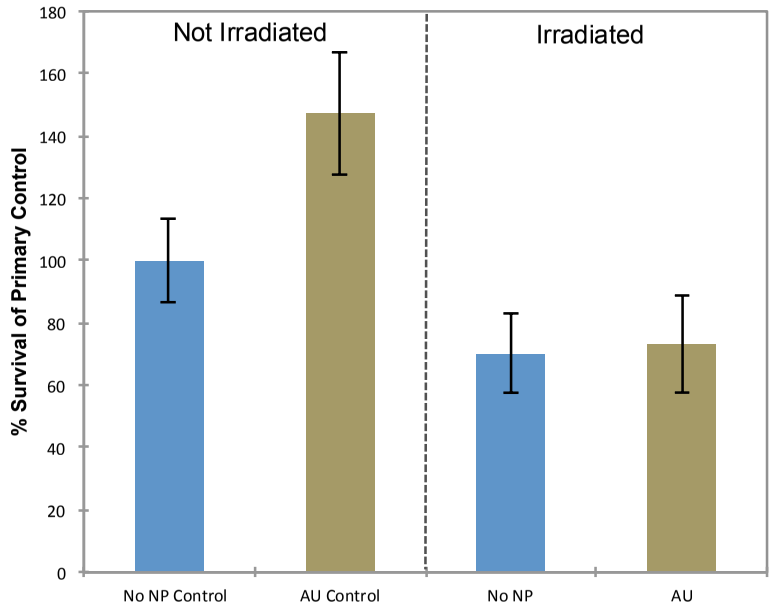

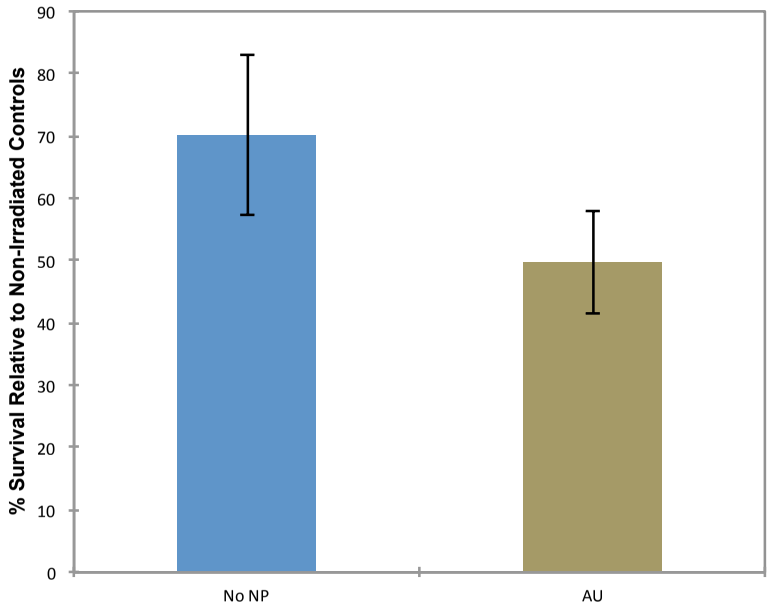

Toxicity	tstat	P-value	% Diff From Control
No NP Control			
AU Control	1.988649	0.185057	47.347881

Radio Effect	tstat	P-value	% Diff From Control
No NP			
AU	-1.342347	0.272026	-29.154520

Fig. 29 GNPs were added to 184A1 breast epithelial cells in 10 μM concentrations. Cells were exposed to 2 Gy equivalent single dose of proton radiation and assessed using the MTT assay. Data are expressed as percentages of the primary control first to show chemical toxicity, and then irradiated groups are expressed as percentages of their corresponding non-irradiated controls to provide insight into any physical effects (mean ± standard error). Experimental groups are compared to untreated controls and statistical significance is determined by Student's t-test (*P<0.05, **P<0.01).

Figure 30 shows GNPs investigated in various concentrations with the MCF7 breast carcinoma cell line and the 22RV1 prostate carcinoma cell line. The MCF7 cells and the 22RV1 cells were exposed to 25 cGy and 30 cGy equivalent single dose of proton radiation respectively and evaluated using the clonogenic assay. There is clear evidence of severe chemical toxicity in the non-irradiated controls after 2 weeks of growth and no clear effect in the surviving irradiated groups. The toxicity in all of the non-irradiated treated controls for both cell lines is highly statistically significant. With so much chemical toxicity in these cell lines, the data is undoubtedly skewed making it difficult to determine anything meaningful with regards to any protective or sensitive effects.

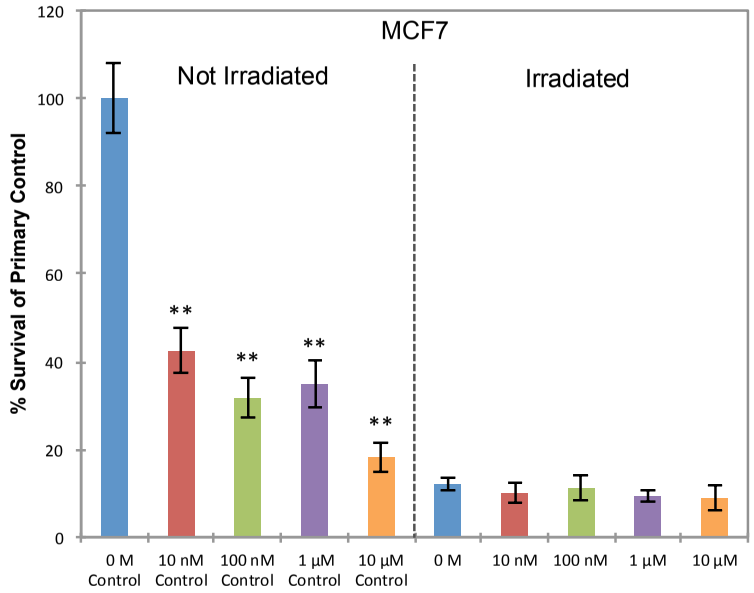

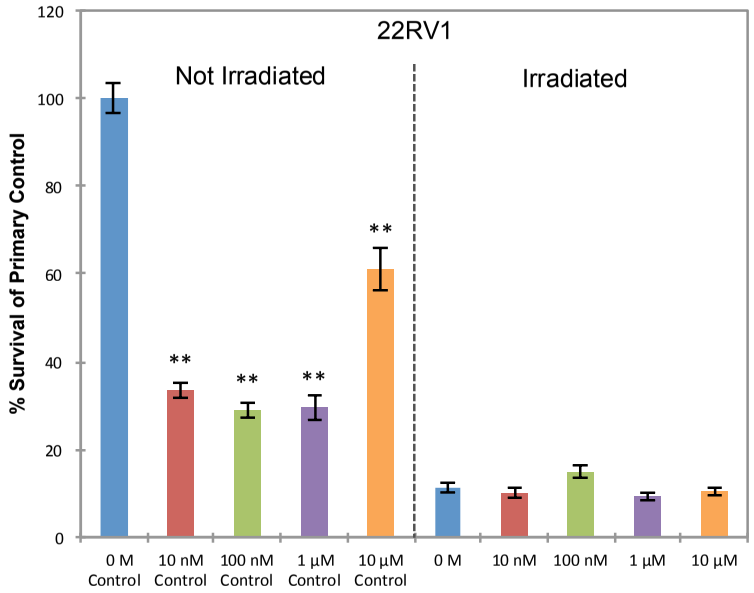

Toxicity	tstat	P-value	% Diff From Control
0 M Control			
10 nM Control	-6.016241	0.000087	-57.651246
100 nM Control	-7.423003	0.000013	-68.327402
1 µM Control	-6.738295	0.000032	-65.124555
10 µM Control	-9.383360	0.000001	-81.850534

Toxicity	tstat	P-value	% Diff From Control
0 M Control			
10 nM Control	-17.051996	0.000000	-66.522865
100 nM Control	-18.232662	0.000000	-71.009491
1 µM Control	-15.581992	0.000000	-70.405522
10 µM Control	-6.636327	0.000037	-38.999137

Fig. 30 A survey of concentrations with GNPs in MCF7 breast carcinoma and 22RV1 prostate carcinoma cells. Cells were exposed to a 25 cGy (MCF7) or a 30 cGy (22RV1) equivalent single dose of proton radiation and assessed with a clonogenic assay. Data are expressed as percentages of the primary control (mean ± standard error). Experimental groups are compared to untreated controls and statistical significance is determined by Student's t-test (*P<0.05, **P<0.01).

Chapter 4: Discussion

The aims of this research were 1) to determine if CNP treatment would offer a protective effect to non-malignant cells and 2) to demonstrate that CNPs would enhance the rate of killing in tumor cells as well when exposed to particle radiation. The effects of CNPs on cells exposed to x-rays has been investigated in some detail [17, 64-67], but similar research using proton irradiation has not been carried out to any extent.

4.1 Cell Survival Data

Initially, cell survival curves were measured to find an estimated dose of administration that was close to the true LD50 level. A table summarizing these LD50 values and the chosen dose values is shown in Figure 31 below.

Cell Survival Curves	184A1	22RV1	MCF7
MTT LD50 Values	3.3 Gy	55 cGy	35 cGy
Colony LD50 Values	~	75 cGy	55 cGy
Chosen Dose Values	3.3 Gy	40 cGy	30 cGy

Fig. 31 A table summary of the predicted LD50 values from the cell survival curves with the chosen dose values.

This was performed somewhat successfully in all three cell lines because the cell killing did in fact increase with increasing dose and could be plotted using the linear-quadratic model. However, the MTT assay only indicates metabolic activity, so there is the possibility that it can misrepresent the genuine cell survivability. Cell survival is truly

indicated by cell proliferation. There could be metabolically active cells being picked up by the MTT assay that would have little to no proliferation. Plating variability is a concern as well. The number of cells that were plated can be determined and controlled to be consistent among wells, but true cell proliferation is a stochastic process and is responsible for a large portion of the error in these experiments. Also, the cell populations in this study were asynchronous. Cells in this population that were in the part of the cell cycle preparing for mitosis or undergoing mitosis were particularly vulnerable to damage. Research has shown that these mitotic cells are more radiosensitive than the non-mitotic cells [114]. This can result in two distinct populations, which could yield a survival curve that initially drops at lower doses due to the killing of the more radiosensitive population and then gradually falls at the higher doses due to the remaining radioresistant population [115]. Although the linear-quadratic model is well used in the field of radiobiology, it does not incorporate DNA repair and the transformation of cells due to radiation exposure. The transformation process could include mutated cells that are permitted to grow beyond the set restrictions of the remaining population, allowing them to find new forms of survival. Contemporary models include these factors using a combination of linear, quadratic, and higher order terms and could provide a superior fit for high LET radiation [116, 117].

4.2 CNP Data

Various types and concentrations of CNPs were then tested for their protective and sensitizing properties in all three cell lines with some success. The experimental results from that testing are summarized below in Figure 32.

Chemical Effects	184A1	22RV1	MCF7
MTT Assay (NH4)	Toxicity **	Toxicity **	Toxicity **
MTT Assay (NC)	None	Toxicity **	Toxicity **
Colony Assay (NH4)	~	None	None
Colony Assay (NC)	~	None	None

Net Effects	184A1	22RV1	MCF7
MTT Assay (NH4)	Decrease (36%) **	Decrease (39%) **	Decrease (42%) *
MTT Assay (NC)	Increase (32%) *	None	Decrease (38%) **
Colony Assay (NH4)	~	None	Decrease (42%) *
Colony Assay (NC)	~	None	None

Physical Effects	184A1	22RV1	MCF7
MTT Assay (NH4)	Sensitization *	None	None
MTT Assay (NC)	None	Protection *	Sensitization *
Colony Assay (NH4)	~	None	Sensitization **
Colony Assay (NC)	~	None	None

Fig. 32 A table summary of the experimental results showing only significant effects. (*=Significant, **=Highly Significant)

Both NC and NH4 CNPs were examined in the 184A1 breast epithelial cell line to determine if any protective effects would emerge. MTT results indicate the best candidate for radioprotection to be NC at the 10 μM concentration, which yielded a net effect increase of 32% compared to the untreated group. Another MTT experiment in which nanoparticles were added post-irradiation indicates that NH4 was the superior radiomitigator, with a 25% increase compared to the untreated group in the secondary interpretive step. The radioprotective characteristics of CNPs stem from their ability to act as free radical

scavengers with indirect damage caused by the radiolysis process. This was shown with previous research using the high indirect damage produced by x-rays to produce high cell survival rates [17]. By contrast, with charged particle radiation there is more direct DNA damage sustained and less indirect damage to the DNA from free radicals. This may explain why the CNPs were not as effective in the cells against proton radiation as they were with x-ray exposure.

For the 22RV1 prostate carcinoma cell line, the preliminary MTT study using CNPs at a concentration of 1 μM showed some promise of sensitization for both CNPs. However, further experiments revealed NH4 to be the best candidate with a net effect drop of 39% at the 1 μM level when compared to the untreated group. Also, it is worth mentioning that the lowest concentration of NH4 indicated slight physical sensitization when the data were analyzed to compare each irradiated sample with its corresponding non-irradiated control (15%, not statistically significant) and showed no significant chemical effects in the non-irradiated control. On the other hand, the results from the colony assay demonstrated that there were no significant effects for either CNP in the long term.

In the MCF7 breast carcinoma cell line counterpart, both NC and NH4 showed promising physical sensitization using the MTT assay. NH4 showed a significant 42% drop in the 10 μM group when compared to the untreated group and the implied physical sensitization from the interpretive step yielded a 19% drop also. NC revealed a net effect that produced a highly significant 38% drop in the 100 nM group when compared to the untreated group and the implied physical sensitization from the secondary step yielded a significant 27% drop as well. The results from the colony assay were not perfectly aligned,

but did show NH4 as the best emerging candidate with a significant net effect decrease of 42% when compared to the untreated group and an implied physical sensitization from the secondary step of 54%. The chemical effects that were detected in this study were a main issue of concern. The CNPs toxicity has shown conflicting results in previous studies suggesting that the chemical effects come from their ability to transition between the two valence states and increase the presence of oxygen vacancies [118]. This could explain some of the inconsistencies observed.

4.3 GNP Data

Gold type nanoparticles have been shown to sensitize tumorous cells due in part to their secondary electron emission properties [50-55]. It has been shown that their main pathway into the cell is due to RME (receptor-mediated endocytosis) with dependency on conditions such as size, shape, surface charge, and added functional groups [119]. One study using protein-coated GNPs found that, more specifically, the clathrin-dependent endocytosis pathway is the main transport system into the cells [120]. GNPs were brought into this research as a hopeful benchmark study under the assumption that they could be used as a sensitization standard for comparison purposes. The percent of GNPs absorbed by the cells after initial administration was successfully determined in the 22RV1 prostate tumor cell line using a novel absorption assay. These percentages could be used as a reference to describe CNP absorption since they are comparable in size. An MTT assay with GNPs show some sensitizing properties in the non-malignant 184A1 cell line. It was expected that this sensitization characteristic of gold would show up in the malignant cell lines of MCF7 and 22RV1 as well. However, that characteristic was not discovered. Colony

data reveals tremendous toxicity and therefore no sensitizing effect was found in the irradiated groups. It is possible that their cytotoxicity is just too overwhelming to interpret anything meaningful with these cell lines. GNPs have been shown to have a significant cell-line dependent correlation between uptake and toxicity [51]. These surprising results could also be explained by the effects of GNPs with proton radiation. One study used Monte Carlo simulations to compare the effects of GNPs between photon radiation and proton radiation, and found that since most of the absorbed GNPs remained tied up in lysosomes and don't enter the nucleus, the secondary electrons generated from proton radiation may not have sufficient range to reach the nucleus and cause damage, whereas the secondary electrons generated by the photon radiation did have sufficient range [52].

The results presented here demonstrate the properties of cerium oxide nanoparticles to provide sensitization for malignant breast cells. There were some indications of protective properties in the nonmalignant breast cells as well and further investigation could confirm these effects. These properties are determined by the surface valence states of the nanoparticles, which are dependent on the microenvironment of the CNP itself. Some potential applications of CNPs include the enhancement of ion beam therapy in the treatment of some cancers and possible protection from terrestrial and space radiation.

4.4 Future Directions

The potential for cerium oxide nanoparticles to be used as a radiosensitizer has been shown previously [64, 65, 67]. All of the investigations involving these radiosensitizers and their effect on cancer cells have been examined with x-ray exposure,

so there was no experimental data showing results with regards to charged particle radiation. It was the goal of this research to start that investigation into CNPs sensitization effect of cancer cells and their protective effect on normal cells with the use of proton radiation. The fluctuating chemical toxicity in this study was a cause for concern. However, recent adaptations of CNPs involve using a polyethylene glycol cap to enhance stability, reduce cytotoxicity, and improve biological properties [121]. This variant could be investigated with future experiments. This initial investigation contained many experimental variables, including a wide range of CNP concentrations that the cells were exposed to. Additional studies could investigate promising CNPs between these established concentrations in order locate a value that would minimize the chemical effects and maximize the physical effects while improving the dose reduction factor. With the ability of ECU's Pelletron Accelerator, further investigation could implement various ion beams to study the CNPs effect against heavier charged particles. The titanium foil used at the end of the beamline was sufficient for maintaining vacuum and providing minimal loss in beam energy, but a thinner exit window could decrease the energy loss even further and is feasible with stronger metal alloys like Havar foil, which has been used in other similar experimental setups [122]. This could facilitate the use of lower energy ion beams on CNP treated cells to assess their effects at higher LET values. *In vivo* studies with mice may present a better understanding of the complete whole body effects of implementing the CNPs. There are extensive nanoparticle candidates available for optional avenues in future research. Using the current setup, it would be valuable to assess the effects of different nanoparticle types used to treat tumor cells. This could be beneficial in the upcoming area of heavy ion therapy.

References

[1] Hellweg CE, Baumstark-Khan C. Getting ready for the manned mission to Mars: the astronauts' risk from space radiation. Naturwissenschaften 2007;94(7):517-26.

[2] Hosseinimehr SJ. Trends in the development of radioprotective agents. Drug Discovery Today 2007;12(19-20):794-805.

[3] Mettler FA, Jr., Thorriadsen BR, Bhargavan M, Gilley DB, Gray JE, Lipoti JA, McCrohan J, Yoshizurrli TT, Mahesh M. Medical radiation exposure in the us in 2006: preliminary results. Health Physics 2008;95(5):502-7.

[4] Khan FM, Gibbons JP. The physics of radiation therapy. Fifth edition. ed. Philadelphia, PA: Lippincott Williams & Wilkins/Wolters Kluwer; 2014.

[5] Babaei M, Ganjalikhani M. The potential effectiveness of nanoparticles as radio sensitizers for radiotherapy. BioImpacts : BI 2014;4(1):15-20.

[6] Juzenas P, Chen W, Sun Y-P, Coelho MAN, Generalov R, Generalova N, Christensen IL. Quantum dots and nanoparticles for photodynamic and radiation therapies of cancer. Advanced Drug Delivery Reviews 2008;60(15):1600-14.

[7] Cucinotta FA. Space Radiation Cancer Risks. 2007. Available from: https://ntrs.nasa.gov/search.jsp?R=20070006479

[8] Attix FH. Introduction to radiological physics and radiation dosimetry. John Wiley & Sons; 2008.

[9] Saw CB. Foundation of radiological physics. CB Saw; 2004.

[10] Turner JE. Atoms, radiation, and radiation protection. John Wiley & Sons; 2008.

[11] Podgorsak EB. Review of radiation oncology physics: a handbook for teachers and students. Vienna, International Atomic Energy Agency Educational Reports Series 2003.

[12] Carron NJ. An introduction to the passage of energetic particles through matter. CRC Press; 2006.

[13] Sherer MAS, Visconti PJ, Ritenour ER, Haynes K. Radiation protection in medical radiography. Elsevier Health Sciences; 2014.

[14] Halperin EC, Brady LW, Wazer DE, Perez CA. Perez & Brady's principles and practice of radiation oncology. Lippincott Williams & Wilkins; 2013.

[15] Jonathan EC, Bernhard EJ, McKenna WG. How does radiation kill cells? Current Opinion in Chemical Biology 1999;3(1):77-83.

[16] Nikjoo H, Uehara S, Emfietzoglou D. Interaction of radiation with matter. CRC Press; 2012.

[17] Tarnuzzer RW, Colon J, Patil S, Seal S. Vacancy engineered ceria nanostructures for protection from radiation-induced cellular damage. Nano Letters 2005;5(12):2573-7.

[18] Colon J, Herrera L, Smith J, Patil S, Komanski C, Kupelian P, Seal S, Jenkins DW, Baker CH. Protection from radiation-induced pneumonitis using cerium oxide nanoparticles. Nanomedicine-Nanotechnology Biology and Medicine 2009;5(2):225-31.

[19] Ziegler JF, Ziegler MD, Biersack JP. SRIM–The stopping and range of ions in matter (2010). Nuclear Instruments and Methods in Physics Research Section B: Beam Interactions with Materials and Atoms 2010;268(11):1818-23.

[20] Friedland W, Jacob P, Paretzke HG, Merzagora M, Ottolenghi A. Simulation of DNA fragment distributions after irradiation with photons. Radiation and Environmental Biophysics 1999;38(1):39-47.

[21] Plante I. A Monte-Carlo step-by-step simulation code of the non-homogeneous chemistry of the radiolysis of water and aqueous solutions. Part I: theoretical framework and implementation. Radiation and Environmental Biophysics 2011;50(3):389-403.

[22] Plante I. A Monte-Carlo step-by-step simulation code of the non-homogeneous chemistry of the radiolysis of water and aqueous solutions-Part II: calculation of radiolytic yields under different conditions of LET, pH, and temperature. Radiation and Environmental Biophysics 2011;50(3):405-15.

[23] Friedland W, Dingfelder M, Kundrat P, Jacob P. Track structures, DNA targets and radiation effects in the biophysical Monte Carlo simulation code PARTRAC. Mutation Research 2011;711(1-2, Sp. Iss. SI):28-40.

[24] Hall EJ, Giaccia AJ. Radiobiology for the radiologist. 6th ed. Philadelphia: Lippincott Williams & Wilkins; 2006.

[25] Hanai R, Yazu M, Hieda K. On the experimental distinction between ssbs and dsbs in circular DNA. International Journal of Radiation Biology 1998;73(5):475-9.

[26] Raviraj J, Bokkasam VK, Kumar VS, Reddy US, Suman V. Radiosensitizers, radioprotectors, and radiation mitigators. Indian Journal of Dental Research: official publication of Indian Society for Dental Research 2014;25(1):83-90.

[27] Dziegielewski J, Baulch JE, Goetz W, Coleman MC, Spitz DR, Murley JS, Grdina DJ, Morgan WF. WR-1065, the active metabolite of amifostine, mitigates radiation-induced delayed genomic instability. Free Radical Biology & Medicine 2008;45(12):1674-81.

[28] Khodarev NN, Kataoka Y, Murley JS, Weichselbaum RR, Grdina DJ. Interaction of amifostine and ionizing radiation on transcriptional patterns of apoptotic genes expressed in human microvascular endothelial cells (HMEC). International Journal of Radiation Oncology Biology Physics 2004;60(2):553-63.

[29] Deneve WJ, Everett CK, Suminski JE, Valeriote FA. Influence of WR-2721 on DNA cross-linking by nitrogen mustard in normal mouse bone marrow and leukemia cells in-vivo. Cancer Research 1988;48(21):6002-5.

[30] Johnke RM, Sattler JA, Allison RR. Radioprotective agents for radiation therapy: future trends. Future Oncology 2014;10(15):2345-57.

[31] Brizel DM, Wasserman TH, Henke M, Strnad V, Rudat V, Monnier A, Eschwege F, Zhang J, Russell L, Oster W, Sauer R. Phase III randomized trial of amifostine as a radioprotector in head and neck cancer. Journal of Clinical Oncology 2000;18(19):3339-45.

[32] Mitchell JB, Degraff W, Kaufman D, Krishna MC, Samuni A, Finkelstein E, Ahn MS, Hahn SM, Gamson J, Russo A. Inhibition of oxygen-dependent radiation-induced damage by the nitroxide superoxide dismutase mimic tempol. Archives of Biochemistry and Biophysics 1991;289(1):62-70.

[33] Hahn SM, Tochner Z, Krishna CM, Glass J, Wilson L, Samuni A, Sprague M, Venzon D, Glatstein E, Mitchell JB, Russo A. Tempol a stable free radical is a novel murine radiation protector. Cancer Research 1992;52(7):1750-3.

[34] Martin RF, Broadhurst S, D'Abrew S, Budd R, Sephton R, Reum M, Kelly DP. Radioprotection by DNA ligands. The British Journal of Cancer Supplement 1996;27:S99-101.

[35] Tawar U, Bansal S, Shrimal S, Singh M, Tandon V. Nuclear condensation and free radical scavenging: a dual mechanism of bisbenzimidazoles to modulate radiation damage to DNA. Molecular and Cellular Biochemistry 2007;305(1-2):221-33.

[36] Singh VK, Yadav VS. Role of cytokines and growth factors in radioprotection. Experimental and Molecular Pathology 2005;78(2):156-69.

[37] Felemovicius I, Bonsack ME, Baptista ML, Delaney JP. Intestinal radioprotection by vitamin E (alpha-tocopherol). Annals of Surgery 1995;222(4):504-8; discussion 8-10.

[38] Kumar KS, Srinivasan V, Toles R, Jobe L, Seed TM. Nutritional approaches to radioprotection: vitamin E. Military Medicine 2002;167(2 Suppl):57-9.

[39] Keithahn C, Lerchl A. 5‐Hydroxytryptophan is a more potent in vitro hydroxyl radical scavenger than melatonin or vitamin C. Journal of Pineal Research 2005;38(1):62-6.

[40] Kitts DD, Wijewickreme AN, Hu C. Antioxidant properties of a North American ginseng extract. Molecular and Cellular Biochemistry 2000;203(1):1-10.

[41] Attele AS, Wu JA, Yuan C-S. Ginseng pharmacology: multiple constituents and multiple actions. Biochemical Pharmacology 1999;58(11):1685-93.

[42] Lee T-K, Johnke RM, Allison RR, O'Brien KF, Dobbs LJ, Jr. Radioprotective potential of ginseng. Mutagenesis 2005;20(4):237-43.

[43] Lee T-K, Allison RR, O'Brien KF, Khazanie PG, Johnke RM, Brown R, Bloch RM, Tate ML, Dobbs LJ, Kragel PJ. Ginseng reduces the micronuclei yield in lymphocytes after irradiation. Mutation Research 2004;557(1):75-84.

[44] Goldwyn S, Lazinsky A, Wei H. Promotion of health by soy isoflavones: efficacy, benefit and safety concerns. Drug Metabolism and Drug Interactions 2000;17(1-4):261-89.

[45] Landauer MR, Srinivasan V, Seed TM. Genistein treatment protects mice from ionizing radiation injury. Journal of Applied Toxicology 2003;23(6):379-85.

[46] Yashar CM, Spanos WJ, Taylor DD, Gercel-Taylor C. Potentiation of the radiation effect with genistein in cervical cancer cells. Gynecologic Oncology 2005;99(1):199-205.

[47] Rucinska A, Roszczyk M, Gabryelak T. Cytotoxicity of the isoflavone genistein in NIH 3T3 cells. Cell Biology International 2008;32(8):1019-23.

[48] Hsieh C-Y, Santell RC, Haslam SZ, Helferich WG. Estrogenic effects of genistein on the growth of estrogen receptor-positive human breast cancer (MCF-7) cells in vitro and in vivo. Cancer Research 1998;58(17):3833-8.

[49] Salata OV. Applications of nanoparticles in biology and medicine. Journal of Nanobiotechnology 2004;2(1):3.

[50] Chithrani DB, Jelveh S, Jalali F, van Prooijen M, Allen C, Bristow RG, Hill RP, Jaffray DA. Gold nanoparticles as radiation sensitizers in cancer therapy. Radiation Research 2010;173(6):719-28.

[51] Jain S, Coulter JA, Hounsell AR, Butterworth KT, McMahon SJ, Hyland WB, Muir MF, Dickson GR, Prise KM, Currell FJ, O'Sullivan JM, Hirst DG. Cell-specific radiosensitization by gold nanoparticles at megavoltage radiation energies. International Journal of Radiation Oncology Biology Physics 2011;79(2):531-9.

[52] Lin Y, McMahon SJ, Scarpelli M, Paganetti H, Schuemann J. Comparing gold nano-particle enhanced radiotherapy with protons, megavoltage photons and kilovoltage photons: a Monte Carlo simulation. Physics in Medicine and Biology 2014;59(24):7675-89.

[53] McMahon SJ, Prise KM, Currell FJ. Comment on 'implications on clinical scenario of gold nanoparticle radiosensitization in regard to photon energy, nanoparticle size, concentration and location'. Physics in Medicine and Biology 2012;57(1):287-90; discussion 91-5.

[54] McQuaid HN, Muir MF, Taggart LE, McMahon SJ, Coulter JA, Hyland WB, Jain S, Butterworth KT, Schettino G, Prise KM, Hirst DG, Botchway SW, Currell FJ. Imaging and radiation effects of gold nanoparticles in tumour cells. Scientific Reports 2016;6:19442-Article No.: .

[55] Zheng Y, Hunting DJ, Ayotte P, Sanche L. Radiosensitization of DNA by gold nanoparticles irradiated with high-energy electrons. Radiation Research 2008;169(1):19-27.

[56] Avalos Funez A, Isabel Haza A, Mateo D, Morales P. In vitro evaluation of silver nanoparticles on human tumoral and normal cells. Toxicology Mechanisms and Methods 2013;23(3, Sp. Iss. SI):153-60.

[57] Chandrasekharan DK, Nair CKK. Studies on silver nanoparticle-glycyrrhizic acid complex as a radioprotector and an adjuvant in radiotherapy under in vivo conditions. Cancer Biotherapy & Radiopharmaceuticals 2012;27(10):642-51.

[58] Xu R, Ma J, Sun X, Chen Z, Jiang X, Guo Z, Huang L, Li Y, Wang M, Wang C, Liu J, Fan X, Gu J, Chen X, Zhang Y, Gu N. Ag nanoparticles sensitize IR-induced killing of cancer cells. Cell Research 2009;19(8):1031-4.

[59] Ng KW, Khoo SPK, Heng BC, Setyawati MI, Tan EC, Zhao X, Xiong S, Fang W, Leong DT, Loo JSC. The role of the tumor suppressor p53 pathway in the cellular DNA damage response to zinc oxide nanoparticles. Biomaterials 2011;32(32):8218-25.

[60] Porcel E, Liehn S, Remita H, Usami N, Kobayashi K, Furusawa Y, Le Sech C, Lacombe S. Platinum nanoparticles: a promising material for future cancer therapy? Nanotechnology 2010;21(8):85103-.

[61] Maier-Hauff K, Ulrich F, Nestler D, Niehoff H, Wust P, Thiesen B, Orawa H, Budach V, Jordan A. Efficacy and safety of intratumoral thermotherapy using magnetic iron-oxide nanoparticles combined with external beam radiotherapy on patients with recurrent glioblastoma multiforme. Journal of Neuro-Oncology 2011;103(2):317-24.

[62] Le Duc G, Miladi I, Alric C, Mowat P, Brauer-Krisch E, Bouchet A, Khalil E, Billotey C, Janier M, Lux F, Epicier T, Perriat P, Roux S, Tillement O. Toward an image-guided microbeam radiation therapy using gadolinium-based nanoparticles. ACS Nano 2011;5(12):9566-74.

[63] Chattopadhyay S, Dash SK, Tripathy S, Das B, Kar Mahapatra S, Pramanik P, Roy S. Cobalt oxide nanoparticles induced oxidative stress linked to activation of TNF‐α/caspase‐8/p38‐MAPK signaling in human leukemia cells. Journal of Applied Toxicology 2015;35(6):603-13.

[64] Wason MS, Colon J, Das S, Seal S, Turkson J, Zhao J, Baker CH. Sensitization of pancreatic cancer cells to radiation by cerium oxide nanoparticle-induced ROS production. Nanomedicine-Nanotechnology Biology and Medicine 2013;9(4):558-69.

[65] Das S, Dowding JM, Klump KE, McGinnis JF, Self W, Seal S. Cerium oxide nanoparticles: applications and prospects in nanomedicine. Nanomedicine 2013;8(9):1483-508.

[66] Karakoti AS, Singh S, Kumar A, Malinska M, Kuchibhatla SVNT, Wozniak K, Self WT, Seal S. PEGylated nanoceria as radical scavenger with tunable redox chemistry. Journal of the American Chemical Society 2009;131(40):14144-5.

[67] Madero-Visbal RA, Alvarado BE, Colon JF, Baker CH, Wason MS, Isley B, Seal S, Lee CM, Das S, Manon R. Harnessing nanoparticles to improve toxicity after head and neck radiation. Nanomedicine-Nanotechnology Biology and Medicine 2012;8(7):1223-31.

[68] Karakoti AS, Monteiro-Riviere NA, Aggarwal R, Davis JP, Narayan RJ, Self WT, McGinnis J, Seal S. Nanoceria as antioxidant: synthesis and biomedical applications. JOM (Warrendale, Pa : 1989) 2008;60(3):33-7.

[69] Heckert EG, Karakoti AS, Seal S, Self WT. The role of cerium redox state in the SOD mimetic activity of nanoceria. Biomaterials 2008;29(18):2705-9.

[70] Pirmohamed T, Dowding JM, Singh S, Wasserman B, Heckert E, Karakoti AS, King JES, Seal S, Self WT. Nanoceria exhibit redox state-dependent catalase mimetic activity. Chemical Communications (Cambridge, England) 2010;46(16):2736-8.

[71] Dowding JM, Dosani T, Kumar A, Seal S, Self WT. Cerium oxide nanoparticles scavenge nitric oxide radical (˙NO). Chemical Communications (Cambridge, England) 2012;48(40):4896-8.

[72] Xue Y, Luan Q, Yang D, Yao X, Zhou K. Direct evidence for hydroxyl radical scavenging activity of cerium oxide nanoparticles. The Journal of Physical Chemistry C 2011;115(11):4433-8.

[73] Asati A, Santra S, Kaittanis C, Nath S, Perez JM. Oxidase-like activity of polymer-coated cerium oxide nanoparticles. Angewandte Chemie (International ed in English) 2009;48(13):2308-12.

[74] Colon J, Hsieh N, Ferguson A, Kupelian P, Seal S, Jenkins DW, Baker CH. Cerium oxide nanoparticles protect gastrointestinal epithelium from radiation-induced damage by reduction of reactive oxygen species and upregulation of superoxide dismutase 2. Nanomedicine-Nanotechnology Biology and Medicine 2010;6(5):698-705.

[75] Mamotyuk E, Klochkov V, Grygorova G, Yefimova S, Malyukin YV. Radioprotective effect of CeO2 and GdEuVO4 nanoparticles in “in vivo” experiments. Nanoscience Advances in CBRN Agents Detection, Information and Energy Security. Springer; 2015, p. 193-7.

[76] Lin W, Huang Y-w, Zhou X-D, Ma Y. Toxicity of cerium oxide nanoparticles in human lung cancer cells. International Journal of Toxicology 2006;25(6):451-7.

[77] Alili L, Sack M, Karakoti AS, Teuber S, Puschmann K, Hirst SM, Reilly CM, Zanger K, Stahl W, Das S, Seal S, Brenneisen P. Combined cytotoxic and anti-invasive properties of redox-active nanoparticles in tumor-stroma interactions. Biomaterials 2011;32(11):2918-29.

[78] Ibanez IL, Notcovich C, Catalano PN, Bellino MG, Duran H. The redox-active nanomaterial toolbox for cancer therapy. Cancer Letters 2015;359(1):9-19.

[79] Sayin VI, Ibrahim MX, Larsson E, Nilsson JA, Lindahl P, Bergo MO. Antioxidants accelerate lung cancer progression in mice. Science Translational Medicine 2014;6(221):221ra15-Article No.: ra15.

[80] Zhou X, Wong LL, Karakoti AS, Seal S, McGinnis JF. nanoceria inhibit the development and promote the regression of pathologic retinal neovascularization in the vldlr knockout mouse. PLoS One 2011;6(2):e16733.

[81] Kong L, Cai X, Zhou X, Wong LL, Karakoti AS, Seal S, McGinnis JF. Nanoceria extend photoreceptor cell lifespan in tubby mice by modulation of apoptosis/survival signaling pathways. Neurobiology of Disease 2011;42(3):514-23.

[82] Pourkhalili N, Hosseini A, Nili-Ahmadabadi A, Hassani S, Pakzad M, Baeeri M, Mohammadirad A, Abdollahi M. Biochemical and cellular evidence of the benefit of a combination of cerium oxide nanoparticles and selenium to diabetic rats. World Journal of Diabetes 2011;2(11):204-10.

[83] Pourkhalili N, Hosseini A, Nili-Ahmadabadi A, Rahimifard M, Navaei-Nigjeh M, Hassani S, Baeeri M, Abdollahi M. Improvement of isolated rat pancreatic islets function by combination of cerium oxide nanoparticles/sodium selenite through reduction of oxidative stress. Toxicology Mechanisms and Methods 2012;22(6):476-82.

[84] Pulido-Reyes G, Rodea-Palomares I, Das S, Sakthivel TS, Leganes F, Rosal R, Seal S, Fernandez-Pinas F. Untangling the biological effects of cerium oxide nanoparticles: the role of surface valence states. Scientific Reports 2015;5:15613.

[85] Park E-J, Choi J, Park Y-K, Park K. Oxidative stress induced by cerium oxide nanoparticles in cultured BEAS-2B cells. Toxicology 2008;245(1-2):90-100.

[86] Hirst SM, Karakoti AS, Tyler RD, Sriranganathan N, Seal S, Reilly CM. Anti-inflammatory properties of cerium oxide nanoparticles. Small (Weinheim an der Bergstrasse, Germany) 2009;5(24):2848-56.

[87] Singh S, Kumar A, Karakoti A, Seal S, Self WT. Unveiling the mechanism of uptake and sub-cellular distribution of cerium oxide nanoparticles. Molecular BioSystems 2010;6(10):1813-20.

[88] Vinardell MP, Mitjans M. Antitumor activities of metal oxide nanoparticles. Nanomaterials (Basel, Switzerland) 2015;5(2):1004-21.

[89] Simonsen LC, Wilson JW, Kim MH, Cucinotta FA. Radiation exposure for human Mars exploration. Health Physics 2000;79(5):515-25.

[90] Stampfer MR, Bartley JC. Induction of transformation and continuous cell lines from normal human mammary epithelial cells after exposure to benzo-a-pyrene. Proceedings of the National Academy of Sciences of the United States of America 1985;82(8):2394-8.

[91] Sramkoski RM, Pretlow TG, II, Giaconia JM, Pretlow TP, Schwartz S, Sy M-S, Marengo SR, Rhim JS, Zhang D, Jacobberger J. A new human prostate carcinoma cell line, 22Rv1. In Vitro Cellular and Developmental Biology Animal 1999;35(7):403-9.

[92] Levenson AS, Jordan VC. MCF-7: The first hormone-responsive breast cancer cell line. Cancer Research 1997;57(15):3071-8.

[93] Seal S. University of Central Florida, NanoScience Technology Center. Orlando, FL. [private communications]; 2017.

[94] Vujaskovic Z, Jackson IL, Seal S, Das S. Methods of using cerium oxide nanoparticles to mitigate or protect against radiation injury. US Patent 9415065 B2; 2016.

[95] Patil S, Kuiry S, Seal S, Vanfleet R. Synthesis of nanocrystalline ceria particles for high temperature oxidation resistant coating. Journal of Nanoparticle Research 2002;4(5):433-8.

[96] Tsunekawa S, Sivamohan R, Ito S, Kasuya A, Fukuda T. Structural study on monosize CeO 2-x nano-particles. Nanostructured Materials 1999;11(1):141-7.

[97] Norton G. New developments in design and applications for Pelletron accelerators. Pramana–J Phys 2002;59(5).

[98] Middleton R. A versatile high intensity negative ion source. Nuclear Instruments and Methods in Physics Research 1983;214(2):139-50.

[99] Middleton R. A versatile high intensity negative ion source. Nuclear Instruments and Methods in Physics Research 1984;220(1):105-6.

[100] Middleton R. A negative ion cookbook. University of Pennsylvania 1989.

[101] Heddle DW. Electrostatic lens systems. CRC Press; 2000.

[102] Davis T. Charging System; 2001. Available from: http://www.pelletron.com/charging.htm.

[103] Ferry JA. Recent developments in electrostatic accelerator technology at NEC. Nuclear Instruments and Methods in Physics Research Section A: Accelerators, Spectrometers, Detectors and Associated Equipment 1993;328(1-2):28-33.

[104] XCAP Software. EPIX Incorporated; 2015.

[105] Bettega D, Calzolari P, Doglia SM, Dulio B, Tallone L, Villa AM. Cell thickness measurements by confocal fluorescence microscopy on C3H10T1/2 and V79 cells. International Journal of Radiation Biology 1998;74(3):397-403.

[106] Belli M, Cera F, Cherubini R, Dalla Vecchia M, Haque AM, Ianzini F, Moschini G, Sapora O, Simone G, Tabocchini MA, Tiveron P. RBE-LET relationships for cell inactivation and mutation induced by low energy protons in V79 cells: further results at the LNL facility. International Journal of Radiation Biology 1998;74(4):501-9.

[107] Belli M, Cera F, Cherubini R, Haque AMI, Ianzini F, Moschini G, Sapora O, Simone G, Tabocchini MA, Tiveron P. Inactivation and mutation induction in V79 cells by low energy protons: Re-evaluation of the results at the LNL facility. International Journal of Radiation Biology 1993;63(3):331-7.

[108] Belli M, Cherubini R, Finotto S, Moschini G, Sapora O, Simone G, Tabocchini MA. RBE-LET relationship for the survival of V79 cells irradiated with low energy protons. International Journal of Radiation Biology 1989;55(1):93-104.

[109] Facility PS-OCNBC. Thawing, propagating and cryopreserving protocol: NCI-PBCF-CRL2505 (22Rv1) prostate carcinoma (ATCC®CRL-2505™). 2012.

[110] Folkard M, Prise KM, Vojnovic B, Newman HC, Roper MJ, Michael BD. Inactivation of V79 cells by low-energy protons, deuterons and helium-3 ions. International Journal of Radiation Biology 1996;69(6):729-38.

[111] Folkard M, Prise KM, Vojnovic B, Davies S, Roper MJ, Michael BD. The irradiation of V79 mammalian cells by protons with energies below 2 MeV Part I. Experimental arrangement and measurements of cell survival. International Journal of Radiation Biology 1989;56(3):221-38.

[112] Boyd CM. Modification of Cell Survival Rates by Cerium Oxide Nanoparticles for Exposure to Proton Radiation. Dissertation, East Carolina University. 2017.

[113] Swartz BW. Viability of Cerium Oxide Nanoparticles as a Radioprotector Against Proton Radiation for Non-malignant Cells. Dissertation, East Carolina University. 2015.

[114] Sinclair W. Cell cycle dependence on the lethal radiation response in mammalian cells. Argonne National Lab., Ill.; 1972.

[115] Schettino G, Folkard M, Prise KM, Vojnovic B, Bowey AG, Michael BD. Low-dose hypersensitivity in Chinese hamster V79 cells targeted with counted protons using a charged-particle microbeam. Radiation Research 2001;156(5 Part 1):526-34.

[116] Sutherland JC. Repair-dependent cell radiation survival and transformation: an integrated theory. Physics in Medicine and Biology 2014;59(17):5073-90.

[117] Sontag W. A discrete cell survival model including repair after high dose-rate of ionizing radiation. International Journal of Radiation Biology 1997;71(2):129-44.

[118] Dunnick KM, Pillai R, Pisane KL, Stefaniak AB, Sabolsky EM, Leonard SS. The effect of cerium oxide nanoparticle valence state on reactive oxygen species and toxicity. Biological Trace Element Research 2015;166(1):96-107.

[119] Kettler K, Veltman K, van de Meent D, van Wezel A, Hendriks AJ. Cellular uptake of nanoparticles as determined by particle properties, experimental conditions, and cell type. Environmental Toxicology and Chemistry 2014;33(3):481-92.

[120] Chithrani BD, Chan WCW. Elucidating the mechanism of cellular uptake and removal of protein-coated gold nanoparticles of different sizes and shapes. Nano Letters 2007;7(6):1542-50.

[121] Li H, Yang Z-Y, Liu C, Zeng Y-P, Hao Y-H, Gu Y, Wang W-D, Li R. PEGylated ceria nanoparticles used for radioprotection on human liver cells under gamma-ray irradiation. Free Radical Biology & Medicine 2015;87:26-35.

[122] Thieberger P, Abendroth H, Alessi J, Cannizzo L, Carlson C, Gustavsson A, Minty M, Snydstrup L. A very thin havar film vacuum window for heavy ions to perform radiobiology studies at the BNL tandem. *Proceedings of 2011 Particle Accelerator Conference, New York, NY.* 2011.